PRINCETON UNIVERSITY

DEPARTMENT OF AERONAUTICAL ENGINEERING

NONLINEAR ASPECTS OF

COMBUSTION INSTABILITY IN LIQUID

PROPELLANT ROCKET MOTORS

Second Yearly Progress Report
For the Period 1 June 1961 to 31 May 1962

Aeronautical Engineering Report No. 553b

Prepared by: *David T. Harrje*
D. T. Harrje, Senior Research Associate

W. C. Strahle
W. C. Strahle, Asst-in-Research

W. A. Sirignano
W. A. Sirignano, Asst-in-Research

Approved by: *L. Crocco*
L. Crocco, Robert H. Goddard Prof.
of Jet Propulsion

1 June 1962

TABLE OF CONTENTS

I. INTRODUCTION

This report covers the continuing progress in the investigation of the "general problem of combustion instability in liquid propellant rocket motors," together with further studies, both experimental and theoretical, of the nonlinear effects in rocket motors. Attention is given to the magnitudes and effects of nonlinear perturbations. Previously these interrelated subjects of "linear" and "nonlinear" combustion instability were covered by separate reports (Ref. I and 2). Sponsorship of this theoretical-experimental research is under NASA Grant NsG 99-60.

To cover one specific area of this research in more detail, a separate technical report is being written for release at this time. The title is, Experimental Studies of Transverse Waves in a Cylindrical Chamber (Ref. 9).

A summary of the more general information covered by the technical report and how it relates to the combustion instability research as a whole will be found in Appendix C. A number of the other related studies are also covered in some detail in Appendices A, B, D, E and F.

The history of the research on the general problem of combustion instability in liquid propellant rocket motors is covered in Ref. I. Aspects of the research on the transverse modes of combustion instability and the use of the variable-angle sector motor were covered in an ARS Journal article (Ref. 3), which is included in reprint form with this report. Reference 2 furnishes the background material and history for the nonlinear studies.

II. SUMMARY

Orientation tests of the injection elements were used in an attempt to cancel the velocity effects present in spinning tangential mode oscillations.

Using tangentially oriented spuds in various combinations, 1 x 12, 6 x 2, 2 x 6 and 4 x 3, the incidence of the spinning tangential mode was altered considerably from one combination to another. Also affected was stability behavior with the baffle in place (prior to burnout), where first and second standing tangential mode oscillations were observed. However, the direction of spin of the tangential wave failed to remain constant with mixture ratio thereby casting doubt on the consistency of the relative mixture ratio distribution across each spray fan. Similar evidence was provided in the pulse limits testing, where the fuel-on-oxidizer doublet was finally abandoned for the like-on-like injection type.

Variable-angle sector motor tests using injection systems similar to those tested on longitudinal hardware have resulted in values of the sensitive time lag and interaction indices for alcohol-oxygen close to those determined longitudinally. This was the expected result, since both methods measure pressure sensitivity alone with differences due to nozzle effects. Working with 30° sector increments on the transverse tests, naturally the same precision as attained in the longitudinal testing was not possible.

Specific tests were designed to compare longitudinally and transversely obtained combustion parameters using the same distributed injector arrangement (i.e., 36 impinging radially oriented pairs on the 360° motor

with each pair covering an equal area of injector face). Only the lower

angle limit could be determined on the transverse tests because of

uncertainties in the gas dynamic behavior at the chamber center at angles

above $180°$. Using suitable axial velocity distributions in the longi-

tudinal case (the variable-length sector motor with the multi-orifice

nozzle was used), good agreement was found to exist between combustion

parameter values determined by the two experimental methods, thus

confirming the applicability of the pressure sensitive theory to both

longitudinal and transverse modes of oscillation.

Additional testing using the variable-length sector motor with

the multi-orifice nozzle involved the short hole (L/D $\approx$ 5) and long

hole (L/D $\approx$ 20) tangentially oriented distributed injectors. Although

some difficulties were found in determining certain stability limits,

agreement between the instability regimes of all three injector

configurations was good. Performance versus length measurements provided

data for velocity distributions in the alcohol-oxygen rocket motor. Nozzle

heat transfer calculations were made to determine true performance of the

injection system.

A reproducible shift in the upper mixture ratio limit was

found for the fuel-on-oxidizer doublet injector (1 x 12), when it was

subjected to pulsed limits testing (fuel-to-oxidizer pulse orientation).

The shift increased with pulse strength. However, when the pulse orien-

tation was reversed the limit shift data became erratic.

Concurrent with the pulsed limits testing was a study of the

pulse itself. These studies, conducted in an optical rocket motor,

supplied data on: the initial shock wave path across the chamber, the

nature of the spinning wave produced, initial amplitude and decay rates for various combinations of powder charges and burst diaphragms, effect of chamber pressure on initial amplitude and decay rate, ability of nitrogen to supply pulses to the system and ability to produce radial and standing modes in addition to the spinning tangential mode.

Pulsed limits testing was continued on like-on-like injector spuds which were shown to be highly sensitive to the presence of pulse disturbances. Normal motor operation showed only a narrow range for the spinning tangential mode and even this was not always reproduced. For these tests no baffle was normally used and when a baffle was employed even the narrow region of instability associated with the 0.1" fan spacing could be eliminated. However, using the 0.1" and 0.2" spaced spray fans, pulsed limits were shown to extend the spinning mode regime over the entire range of operating mixture ratio in a number of instances. Data tended to indicate that some of the lower strength pulses were very effective in inducing the spinning tangential mode with certain orientations. As the pulse limits tests progressed, it was found to be increasingly important to evaluate the initial pulse amplitude in the chamber. These data were provided from the tape records, and the amplitude scatter indicated effects of combustion were present.

The oxidizer-to-fuel pulse orientation was shown to be the most effective in these pulse limits tests. When the opposite orientation was used in the 0.1" spacing tests, the final wave orientation was the reverse of the initial pulse direction indicating the directional preference 0 to F . However, with the 0.2" spacing at higher mixture ratio and high pulse levels (initial peak-to-peak pressure amplitude above 75 psi),

high amplitude waves were produced in the fuel-to-oxidizer direction. Much of the pulsed limits data can only be considered preliminary at this time with many aspects still to be investigated.

Basic studies on the spacial distribution of vaporization and the effect of spinning tangential waves on the droplet fan are being carried out theoretically and experimentally. Another basic study concentrates on the influence of the instantaneous droplet size on combustion instability. Theoretical and experimental work is also under-way in this area. Other areas being treated theoretically involve a rigorous approach to some of the underlying principles in the instability theory as conceived to date and an extension of these concepts to the nonlinear case.

III. DISCUSSION

A. Injection Orientation

In covering the progress of the research, first the general problem of combustion instability in liquid rocket motors will be discussed.

In the previous reports on "linear" combustion instability (i.e., instability which spontaneously builds up from a small disturbance Ref. 1, 4,5), the question of velocity sensitivity was shown to be of considerable importance. This subject was covered in detail in a technical report (Ref. 4). Although longitudinal modes of instability can be explained in terms of the pressure sensitive theory alone, the transverse modes present a more complex situation. Pressure sensitivity is still important, but now velocity effects must also be considered. Shifts in the stability regimes

were caused by the velocity effects present (Ref. 4). Baffles placed in
the motor (extending diametrically across the injector)suppressed these
effects. With the baffle in place, either instability disappeared or
the spinning mode was changed to the far less dangerous (from a heat
transfer standpoint) standing mode. Often such baffles were only
necessary for stabilization of the spinning mode during the starting
transients and seconds later, when the baffle burned away, the motor
remained stable.

Looking at the velocity effect from a linear standpoint (Ref. 4),
one can surmise that arrangements of the injection elements also should
offer a means to attain stable operation. Using the 12-spud injector
(9-inch chamber, 7-inch injection diameter and spuds designed for 1.4
mixture ratio for ethyl alcohol, liquid oxygen) with fuel-on-oxidizer
impingements, Figure I illustrates some of the orientation arrangements
possible. The linear theory assumes an enhancement of the combustion
process with velocity in one direction and a reduction in combustion
rates with the velocities in the opposite direction (Ref. 4). Among the
spud orientations in Figure I, some are so arranged as to cancel the
spinning mode; e.g., the 6 x 2, 2 x 6 arrangements (the first number
refers to the number of individual groups, while the second refers to
the number of spuds per group). When all the spuds are oriented in the
same direction (I x 12), the spinning mode is naturally favored. Other
arrangements include the 4 x 3 and 12 x 1 orientations, which encourage
the standing mode and one odd combination which favors the spinning
mode to a lesser degree (2 x 5 + 2 x 1).

In all of these orientation tests, we are discussing tangentially
oriented spuds, where the injector holes are tangent to the injection circle

and the spray fans therefore fall on injector radii.

First discussing the test results of the 1 x 12 injector, it is seen in Figure 2 that a number of operating conditions are compared. First the rocket chamber was operated in the conventional fashion, denoted as whole chamber tests. Tests were between two and three seconds duration. Ignition was accomplished using three solid propellant ignitors, igniting a mixture of hydrogen gas and full-flow oxygen. This method insured reproducible transient behavior - free of the ignition variations that had proved to be a problem in Ref. 1.

Two series of tests were run on the whole chamber. The earliest series used only a single pressure transducer and hence the direction of the spinning waves could not be detected. A later series using two transducers at a 90° interval on the chamber perimeter, indicated that contrary to expectations the direction of the spin was not constant. The direction was expected to be from the oxidizer rich side of the injection spray fan toward the full rich side. Such a mixture ratio distribution across the spray fan of a doublet was found by Somogyi and Feiler, Ref. 6. The reason for the combustion enhancement direction being from oxidizer to fuel in this case, is that a cryogenic such as liquid oxygen vaporizes more rapidly than the ethyl alcohol and hence is more readily displaced by the resulting velocity disturbances. This movement improves the mixture ratio distribution and enhances the combustion. How well this model works out will be shown later from like-on-like injector testing.

When a diametral baffle was placed in the 1 x 12 injector-chamber combination the spinning mode was eliminated. The stability limit

was shifted from 1.6 for the spinning mode (whole chamber case) to 1.2 - 1.3 for the standing mode baffle case (shown as "with baffle" t < 1 sec in Figure 2). The placement of the baffle, typical of all the orientation tests, is shown in Figure 3. An electrical contact on one end of the aluminum baffle provided a clear indication of when the baffle had burned away. This was recorded along with transducer data on the FM tape.

Using the two transducer position indicated in Figure 3, both spinning and standing modes could be readily identified. Figure 4a illustrates typical standing mode data taken in this manner. Higher standing modes (second tangential) were present in some cases. The direction of spin is determined by the same two pressure transducers and the characteristic wave shape is illustrated. The buildup to the spinning wave after baffle burnout is shown in Figure 4b. The characteristic narrow, peaked waves associated with the transverse spinning modes point clearly to the absence of shocks and represent a proof against the often advanced suggestion that transverse modes can be related to transverse detonation waves (see Appendix D).

After the baffle burns away, Figure 2 indicates that the spinning tangential oscillations are present to a mixture ratio higher than the whole chamber case. In discussing the other cases tested (6 x 2, 2 x 6 and 4 X 3), we will find that this was the only instance in which such higher limits occurred. Additional tests were made, which determined that the region between the limit found with the whole chamber and the highest limit found after baffle burnout was mixed with stable runs. Also to be noted is that the direction of spin changed more than once as mixture ratio was increased. This offered further

proof that these spuds were not behaving as the doublet tested in Ref. 6.

In testing the 6 x 2 and 2 x 6 orientations, no preferential spin direction was expected. Tests were performed in the same manner as in the 1 x 12 case with the results shown in Figures 5 and 6. In both cases no substantial changes were detected in the whole chamber operation as compared to the 1 x 12 case; i.e., stability limits were close to the 1.6 mixture ratio point. With the baffle in place, the 6 x 2 and 2 x 6 showed a band of second tangential standing mode oscillations, which extended from the 1.2 $\bar{r}$ region to the 1.5 $\bar{r}$ region. This was not present in the 1 x 12 case. Below 1.2 $\bar{r}$ all three cases exhibited first tangential standing mode instability. The greatest variation between the 6 x 2 and 2 x 6 cases and the results from the 1 x 12 was the difference in behavior after baffle burnout. Both showed a small but noticeable decrease in the instability limit based on mixture ratio (from 1.6+ for the whole chamber to 1.5 for the "without baffle" conditions), while the 1 x 12 showed an increase.

The most surprising of the orientation tests involved the 4 x 3 injector (see Figure 7), which conceptually should have shown a greater tendency toward standing mode instability. Even the whole motor data with this arrangment showed deviations from the previous tests. The maximum mixture ratio for the occurrence of spinning wave combustion instability was again in the 1.6+ range. However, stable and intermittent oscillations were found at mixture ratios as low as 1.3. With the baffle in place the first tangential standing mode was only found during the lowest mixture ratio run (0.8 F) with a region of intermittent oscillations present near 1.0 $\bar{r}$. After baffle burnout, this intermittent region moved

up only slightly (1.1 F) and the spinning mode was extended to a mixture ratio of 1.0. This is a considerable drop from the 1.5 range of even the 6 x 2 and 2 x 6 types.

These tests illustrated that considerable alterations in the unstable regions of rocket motor operation can be accomplished by orientation of the injection patterns. However, as the 1 x 12 tests indicated, the doublet fuel-on-oxidizer spud does not possess the same spatial distribution of fuel and oxidizer rich zones within the spray fans for operation at different mixture ratios which is a requirement for evaluation of velocity effects. Hence, the data from these tests could not be expected to conform to the predictions originally advanced. Like-on-like injection, with controlled placement of the droplet spray fans of each propellant, is being used in current, "pulsed limits," testing and will be described later in this report.

B. Sector Motor (Variable-Angle)

One method of separating the effects of velocity from those of pressure has involved the use of the sector motor concept. This experimental approach is covered in detail in the ARS Reprint (Ref. 3) included with this report. In order to better compare pressure sensitive effect associated with longitudinal and transverse mode hardware, the sector concept is used in two ways. First as in Ref. 3, the variable-angle sector motor is utilized (with a suitable injector) to determine transverse stability limits with a precision of 30° (the sector angle variation is limited to 30° variations for the injectors in question so as to maintain identical combustion characteristics). If on the other hand, the sector angle is limited to the minimum value (30°) such

that no transverse oscillations are present (angular variation would not prevent radial oscillation, but these do not appear to be a problem for the injectors in question), the length may be varied in the search for longitudinal stability limits. A comparison of the combustion parameters (the pressure-sensitive time lag τ and the p-sensitive interaction index n, Ref. 9) for the transverse and the longitudinal cases is then possible.

The variable-angle sector motor for transverse testing is shown in Figure 8. Although angular variation between $30°$ and $360°$ can be accomplished recent tests have been limited to $180°$ or less because of the uncertain gas dynamics boundary conditions at the center of the motor for angles greater than $180°$ (Ref. 3 and 4). One kind of injector used is the distributed type (each spud occupies the same injector area) with capabilities of $90°$ spud orientation (i.e., tangential or radial arrangements) and propellant flow control to each group of three spuds (per $30°$ sector), see Figure 9.

Problems of operation have plagued this particular injector design, which requires sealing between the fuel and oxidizer manifolds. This has been accomplished with varying degrees of success by teflon "O" rings, metallic "O" rings, teflon coated metallic "O" rings, and finally, all metal seals. No method resulting in a truly satisfactory solution.

Using a radial spud orientation, tests were made at sector angles of 90, 120, 150 and 180 degrees covering the operational mixture ratio range. As seen in Figure 10 only the $180°$ tests indicated first tangential standing mode instability with the lower limit falling between

150° and 180°. Since we are limited to a maximum of 180° and because the next limit based on other transverse testing would occur above 240°, only a limited amount of data on the combustion parameters is forthcoming from these tests. We can calculate the sensitive time lag τ (based on limit of 165°, independent of mixture ratio using $n = 0.9$ from the theoretical curves of Ref. 4 as 0.2 millisec, and also conclude that τ fails to show strong mixture ratio sensitivity. Obviously such data are quite limited for comparison.

More typical of the sector tests with injection concentrated at one injection circle are the tangential orientation tests for the 9" chamber, 7" injection diameter case, using 12 spuds operating at 150 psia and 1000 lb nominal thrust. As is shown in Figure 11, the limit between stable operation and first tangential mode instability occurs between 90° and 120° at low mixture ratios and moves above 120° for high $\bar{r}$. The same trend is found for the upper limit, where 180° sector tests exhibit second tangential mode oscillations below $1.7 \bar{r}$ and first tangential above this mixture ratio. From these data both τ and n can be calculated and typical values would be: for $\bar{r} = 1.0$; $\tau^* = 0.135$ milli-secs, $n = .6$; $\bar{r} = 1.65$; $\tau^* = 0.140$ millisecs, $n = .65$ and for $\bar{r} = 2.4$ $\tau^* = 0.161$ millisecs, $n = .65$. The region covered in these tests in the n, τ^* C_0^*/r_c^* plane is indicated in Figure 12. We could apply two restrictions: (1) that except at the design mixture ratio (1.4), the angular deviation of the resultant spray causes the nearby walls of the sector to alter the results(although the spray fan would not impinge on the wall, the recirculation pattern on the wall side still could be modified) and (2) that if 180° tests indicate the existence of second tangential mode instability; then the first mode should have been

The tests performed on the variable-length sector hardware used three variations of the distributed injector. The standard injector hole arrangment (L/D of the holes $\approx$ 5, 1.4 $\overline{r}$ design, included angle 55$\frac{1}{2}°$) was used for two series of tests, one with the radial orientation the other with the tangential. The other injector type was based on the work of Rupe (Ref. 8) and utilized injection holes of 20 to 1 L/D , preceded by a turbulence induction length (threaded passage).

The first tests using the multi-orifice nozzle were made with the tangentially-oriented, short-hole injector. The results of the testing plotted on a mixture ratio, chamber length basis are shown in Figure 14. Short length limits of stability, and the stability boundary at higher mixture ratios were well defined. Some problems in differentiating between stable and unstable operation were present at the lower mixture ratios and to a lesser degree at the long length limits of the first tangential mode. When questions of exact limits arose, the wave shape, frequency and steadiness of the oscillation were taken into account in deciding which points were unstable and which were marginal or basically stable. The existence of definite regions of unstable operation was far different than the tests using the same injector and conventional nozzle arrangement (Ref. 1), where the motor was completely stable from the 6" to 24" lengths. The data from the short-hole, radially oriented tests are presented in Figure 15. If one compares these results and those obtained with the tangential orientation, it is seen that in both cases the lower limits are close to 6 inches, the upper limits are close to 12 inches and that instability occurs over a range of mixture ratios from 1.0 to 1.8. Similar behavior would be expected with velocity and sensitivity absent. The influence of the walls in this 30° sector motor

could easily explain the variations in the exact instability regime boundaries. Changes in the spray fan interaction between the radial and tangentially oriented arrangements may also explain these variations.

The long-hole injector also yielded a similar range of stability limits with a slight shift to higher mixture ratios and longer lengths (see Figure 16). Another difference between the long-hole and short-hole tests was that the early tests on this injector clearly determined the stability limits, which were relatively free from the intermittent b behavior characteristics of the short-hole testing. However, later confirming tests, although indicating the same lower mixture ratio limit, shed doubt on the exact upper mixture ratio limit. Flow checks of the injector provided no clue as to the reason for the shift. Performance of the long-hole and the short-hole is compared in Figure 17 for both stable and unstable operation at the 10 and 12 inch lengths. The c^* versus mixture ratio curves are similar for both injectors with the performance of the short-hole reaching slightly higher levels.

With the initiation of the long-hole tests, the cavity-type strain gage pressure transducers were incorporated in the system for steady-state pressure measurement. It was, therefore, possible to make an accurate survey of c^* versus mixture ratio for chamber lengths from 2 to 15 inches. These data, as shown in Figure 18, are necessary for the determination of the combustion distribution, which is a prerequisite for finding accurate values of τ and n . It can be seen from Figure 18 that at design mixture ratio (1.4) the performance with the 2 inch length is the same as that for 3, 4 and 6 inches. Thus, as in the previous tests with fuel-on-oxidizer doublet injection, the combustion zone is primarily located in the first 2 inches. At high mixture ratio, a

spread in performance is evident with the combustion zone apparently

extending close to 3 inches. Only a few percentage points increase

in performance was gained by going to the 15 inch length.

The combustion parameter data from tests with the radial hole

orientation can supply comparative values of the sensitive time lag and

interaction index, since it is the same injector arrangment used in the

transverse tests. In determining the combustion parameters for the

longitudinal case, it has been previously mentioned that the axial

combustion distribution is of prime importance. The truth of this state-

ment can be seen in the following illustration. From the c^* versus

chamber length data in Figure 18 and previous information on axial

combustion distributions with impinging injection (Ref. 10), we can

determine the axial velocity distribution in the chamber. These distri-

butions are shown in Figures 19a and 19b together with the associated

plots of τ and n for the multi-orifice nozzle. Actually, the

critical aspect of the combustion distributions is not the "tail" at

longer lengths, but rather the exact location of the region of maximum

slope (i.e., region of maximum burning rate). Figure 19a places this

region at approximately $1\frac{1}{2}$ inches from the injector face, while Figure 19b

places it at approximately 1.1 inches. Thus, the present distributions

bracket previous data (Ref. 10 placed this region at 1.3 ÷ inches

from the face for a similar fuel-on-oxidizer doublet injector).

Using these two combustion distributions, the following values

of τ and n are determined at a mixture ratio of 1.4: from Figure 19a,

τ = 0.17 millisecs and n = 1.19; from Figure 19b, τ = 0.165 millisecs

and n = .9 . Since the values from the transverse motor were τ = 0.2 .

millisecs an n = .9 , we can see that values determined from the two

methods are in good agreement. These data, together with longitudinal,

transverse combustion parameter comparisons in Ref. 3, confirm the

applicability of the pressure sensitive time lag and interaction index

to both longitudinal and transverse mode calculations. Of course, in

the transverse spinning case, v-sensitivity effects also must be taken

into account.

In determining the combustion parameters from the stability

diagrams in Figures 14, 15 and 16, some interesting problems develop.

To theoretically analyze the data, the input information which should be

known includes the geometry of the nozzle, the velocity distribution as

a function of mixture ratio and the mean chamber gas temperature (also a

function of mixture ratio). In addition, if a verification of the theory

is to be carried out (i.e., comparisons of experimental and theoretical

limits as in Ref. 11), the oscillation frequency at either a lower or

upper stability limit must be known. Besides the problems which enter into

the normal determination of the above information, some new problems

are associated with these specific tests. These problems can be traced

to the cooling of the multi-orifice nozzle. Because of the uncertainty

in the distribution of the heat transfer in the subsonic portion of the

nozzle, the Mach number at the nozzle entrance is no longer known.

Furthermore, the application of the isentropic nozzle admittance theory

is no longer valid. This problem is not as severe as it might seem,

however, since the subsonic portion of the multi-orifice nozzle is very

short. Thus, the nozzle acts in an almost quasi-steady fashion and only

slightly affects the stability calculations. A serious effect of this

heat transfer is to essentially invalidate the method most commonly

employed to determine the chamber temperature and velocity distribution –

that of the characteristic velocity measurement for various chamber lengths. Further information on this subject may be found in Appendix A. Unless the nozzle heat transfer distribution is known, c^* cannot be converted to chamber sound speed. A method to correct for such heat transfer effects is found in Appendix B.

Even though a rough idea of the velocity distribution may be gained by the c^* measurement (see Figure 18) and assumption of chamber exit Mach number, highly accurate sound speed measurements are required for these tests. This is because the short nozzle and rather narrow instability regions crowd the non-dimensional frequency range, $\omega^* L^*/c_o^*$, into a very limited range of values. When this occurs, computation of τ and n from length limits and frequency measurements is very sensitive to the non-dimensional frequency, which contains the sound speed. Furthermore, the frequency which is measured is usually a frequency associated with fully developed, high amplitude oscillation, which will certainly differ slightly from the acoustic frequency. Finally, the rather narrow instability regions in Figure 14, 15 and 16 indicate that the interaction index is very close to its minimum permissible value to cause instability in these tests. This requires still greater accuracy in the non-dimensional dimensional frequency measurement.

Because of these difficulties, it was decided to abandon the previous approach of comparing experimental and theoretically calculated limits, but rather both limits were used to determine the combustion parameters. Then τ and n may be directly computed from Figure 19 and the experimental limit curves without a frequency and sound speed measurement (except as required to convert $\tau^* c_o^*$ to τ^*). It should also be

recognized that only one velocity distribution was used in the $\tau - n$ determination, whereas some changes will take place in off-design operation.

From these measurements a novel method of determining the nozzle heat transfer is possible. The c^* data in Figure 18 allow an estimate of $\bar{c}_o^*/c_o^*$ reference versus chamber length, where $\bar{c}_o^*$ reference is the sound speed at $L = 15$ inches. Also with a knowledge of τ^*, the nondimensional frequency at a stability limit may be calculated. Then measurements of the physical frequency can be converted to $\bar{c}_o^*$, which, in turn, may be used to find $\bar{c}_o^*$ reference . If the sound speed at $L = 15$ inches versus mixture ratio is converted to c^* through an isentropic nozzle relation, the resulting c^* curve is shown in Figure 20a. Then the difference in c^* at 15 inches, which was actually measured, and this fictitious c^* should represent the effect of heat transfer in the nozzle and indicate an appropriate value of (see Appendix B). The large amount of data scatter is due to the roughness of the method and the difficulties inherent in stability limit determination. These results should be viewed from the standpoint of checking the magnitude of the heat transfer corrections as shown in Figure 20b rather than for their quantitative value.

Figure 20a represents the heat transfer loss to the nozzle as the difference between the performance evaluated at 15 inches and that calculated from the frequency data. Figure 20b is based on the direct heat transfer calculations covered in Appendix B. In Figure 20b, rather than adding the heat transfer performance loss to the measured performance, the curves represent "revised" theoretical performance on which one can base percentage theoretical calculations. Depending on the assumptions involved, the heat transfer corrections vary considerably;

e.g., f = 0.342 represents fully turbulent flow in the constant area

section "A" of the multi-orifice nozzle (i.e., 34.2% of the heat transfer

occurs in the subsonic portion of the nozzle), while f = 0.5 represents

50% heat transfer in the subsonic portion. It can be seen that the heat

transfer predictions from Figures 20a and 20b are of the same order of

magnitude and hence the performance of the variable-length sector motor

is of the order of 95% of theoretical. Typical of the range of $\mathcal{T}$ and $\mathcal{N}$

values associated with the variable-length sector motor tests of the

distributed injectors are those shown in Figure 21. The long-hole

tangentially oriented injector limits were used for this plot.

Before leaving the discussion of the longitudinal mode, the

testing on the square motor is again in progress. As mentioned in

Ref. I, the square motor hardware has shown its major attribute to date

in supplying heat transfer rates at or beyond the limits of today's

water-cooled transducers (15 Btu/in^2 sec or greater). This particular

activity has been taken over by the variable-length sector motor,

operating with a special chamber section that allows for evaluation

of three transducers at once from a heat transfer standpoint (heat

transfers up to 6 Btu/in^2 sec are capable with that hardware).

Consequently, the testing on the square motor is with a 4 x 4 (16 pairs)

like-on-like injection system and only preliminary data are available at

this time.

D. Pulsed Limits Tests

So far we have been discussing spontaneous stability limits

testing; however, rocket systems are not limited to this "linear" type.

Perturbations during normal operation from a number of possible causes

(probably most important of all, the starting transients) can readily initiate nonlinear combustion instability. To investigate nonlinear instability regimes a series of "pulsed instability limits" tests were made.

The same experimental hardware was used as in the spud orientation tests (see page 8), with the addition of the pulsing device. The pulses were produced firing a charge of smokeless pistol powder behind a calibrated burst diaphragm. The resultant shock wave entered the chamber through a tangentially oriented port (see Figure 22). The pulse gun was covered in detail in Ref. 2. The pulses that were chosen as references were the 45-20 (where the first number indicates the powder charge in grains and the second number indicates the burst diaphragm rating divided by 1000 psi), 30-10 and 15-7.5, with the later addition of 15-2 and 15-1 combinations. Evaluation of the effect of various parameters on the pulses produced was carried out as a separate study in the "optical rocket motor" and is described in detail in Appendix C.

Initial pulse limits testing involved the 1 x 12, fuel-on-oxidizer doublet injector in the 500 lb thrust level alcohol-oxygen motor. A baffle was utilized in order to eliminate nonlinear starting transient effects with the shock pulse following one second after baffle burnout, shutdown was 1/2 to 1 second later (see bottom of Figure 22). The initial direction of pulsing was from the oxidizer rich side of the spray fan toward the fuel rich side (Ref. 6). As pointed out in the orientation tests, the fuel-on-oxidizer doublet failed to show a consistent direction of spin for the tangential wave contrary to initial expectations. The same problems that plagued the orientation testing complicated the situation in the pulse limits testing. When pulsed

from oxidizer-to-fuel the shift in stability limits were erratic. However when the pulse was oriented from fuel to oxidizer the upper mixture ratio limit shifted in a reproducible manner. This shift is illustrated in Figure 23, where the upper limit moves to higher mixture ratios as the pulse strength is increased. The effect of pulsing from fuel to oxidizer at high mixture ratio will be discussed more fully for the case of the like-on-like injector.

The fact that the oxidizer-to-fuel pulse produced erratic limit shift behavior and the inconsistency in the direction of spin resulting from the orientation tests, made it imperative in the pulse limit tests to utilize an injection system that had a known spacial distribution of fuel and oxidizer droplets. The type injection element used next was the like-on- like type, in which fuel impinged on fuel at 90° included angle a known distance away from an oxidizer impinging on oxidizer. The spacing between spray fans was chosen as 0.1 inch initially, and due to the design of the passages in each agreed, there was also a spacing in the perpendicular direction; i.e., the spud placed in the tangential orientation produces sprays spaced initially 0.1 inch apart (parallel to a radius), however, one spray center is 0.15 inches further from the center of the chamber than the other. This arrangement has many similarities to the ring-type injection used in high thrust rocket motors, since in that case fuel and oxidizer doublets are at varying distances from the center of the chamber (alternate rings of fuel and oxidizer).

Using the 0.1" spacing spuds in the tangentially oriented arrangement, initial tests were made with the pulse (from oxidizer to fuel). Since at this point in the testing only one pulse gun position

was available oxidizer had to be on the outside for these tests (i.e. the oxidizer spray fan was closer to the chamber wall).

This point can perhaps be visualized best by referring to Figure 24 where the shock pulse gun on the left was used (actually this diagram is of a later experimental configuration). No matter which way the spud is rotated in this figure the fan closer to the pulse gun also is closer to the outer wall. Since this aspect of the fan orientations is significant, the necessity for the two pulse gun system of Figure 24 is clear.

Returning to the $0.1''$ spacing tests, the results are shown in Figure 25. The chamber under normal operating conditions is shown to be very stable. Only one test was unstable and that was not able to be reproduced in several attempts. However, for the two pulses levels used (45-20 and 30-10) it was possible to initiate sustained spinning tangential mode oscillations up to mixture ratios of 1.5 . The spin direction was the same as the pulse direction (oxidizer to fuel). Testing was limited on this configuration because of hardware erosion at the pulse entrance port due to excess oxygen near the wall surface.

To improve the conditions at the port after several repairs with copper welding, the spray fans were reversed. Thus, the pulse was from fuel to oxidizer with the fuel on the outside. Rather than an immediate transition to unstable operation following the pulse, as was the case previously, the amplitude first decayed. Figure 26 shows the history of events that followed: after decay, the standing mode was set up within the chamber, this in turn made the transition into a spinning wave travelling from oxygen to fuel (opposite to the initial pulse direction).

The pulsed limits determined with this experimental configuration are shown in Figure 27. Here the non-pulsed motor showed a narrow region

of spinning mode instability which could be eliminated using baffles during
the start. In this region (1.3 mixture ratio and below), low amplitude
sinusoidal oscillations were present. This closely resembled the pressure
records obtained at the stability limits of the longitudinal mode. This
zone did not seem to be effected by pulsing the chamber and it may tentatively
be looked upon as perhaps a purely pressure sensitive region (v - effects are
absent).

As the strength of the pulse charges was increased the regime
covered by the spinning tangential mode rose from the 1.3 F range (no pulse)
to above 2.6 F for the 45-20 combination. Records in the stable range of
operation just beyond spinning wave instability limits allowed an evaluation
of the pulses fired into an operating rocket motor. The data from these
tests are shown in Figures 28 and 29. It is evident that both the initial
amplitude and the decay rate are higher for the low mixture ratio pulses.
Thus, it would appear necessary to examine more closely the spinning wave
which each pulse produces in the operating chamber, in order to fairly
evaluate limits. At this point in the testing, the 0.1" spacing injector
spuds had eroded to the point where testing had to be discontinued.

A redesigned spud, which provided improved cooling to the lip
of the injection orifices, was used as the pulsed limits tests were continued.
The spacing for these tests were 0.2 inch and together with the two pulse gun
chamber section (see Figure 24) all four configurations could be investigated.
The four arrangements are: pulse from oxidizer to fuel; oxidizer on the
outside (Ō→F), and fuel on the outside (0→F̄), and the pulse from
fuel to oxidizer; oxidizer on the outside (F→Ō), and fuel on the outside
(F̄→0). The barred notation indicated the outside spray fan. See Figure 30
for a diagram of the four arrangements.

Data from these tests will be compared with the initial peak-to-peak pressure of the spinning wave produced by the pulse. This is important when one considers the apparent influence of combustion on the pulse strength illustrated by the initial amplitude versus mixture ratio for the 45-20 combination shown in Figure 31. Here it is seen that higher amplitudes are associated with the low mixture ratio firings. This was also shown in Figure 28 versus Figure 29 for the 30-10. Data on initial amplitudes are taken from Visicorder records after slow speed playback (20 to 1 reduction) from the FM tape recorder.

Typical of this type of record are the pulsed limits data from the $0 \rightarrow \bar{F}$ (oxidizer to fuel direction, fuel on the outside) tests as shown in Figure 32. If we separate the stability regions with a dotted line, we can see that the region of instability broadens as the pulse strength is increased. This might be termed the "expected" results.

Tests with the fuel on the outside and pulses from the other direction, $\bar{F} \rightarrow 0$, provided only one instance of instability in eight tests across the mixture ratio spectrum. These tests at the 45-20 level, failed to repeat the unstable point, which was spinning in the $0 \rightarrow F$ direction.

When the oxidizer was placed on the outside, the stability regions changed considerably. Figure 33 shows the $\bar{0} \rightarrow F$ data. Here we find that stability limits are well defined at the high initial pulse levels (above 140 psi peak-to-peak) but are stability regions mixed at the low pulse levels. It is also noted that, although stable operation was present for mixture ratios above 2.2 in the high pulse cases (45-20 and 30-10), the low pulse tests (15-20 charges rather than 15-10) were able to produce either unstable or marginally stable operation as high as 2.6 mixture ratio. Until more tests are made in the region between the high and low pulse levels, these data must be considered preliminary; however, the possibility of critical

pulse values (that is, values which are more effective than magnitudes above as well as below) does present itself.

In each of these instability regions the direction of the spin was from the oxidizer to the fuel (O→F). With this in mind, the last group of rocket motor pulsed limits tests are presented in Figure 34. These data are for the F→$\overline{O}$ case and it is seen that at high mixture ratios there exists an instability region where the wave is in the F→O direction. Amplitudes of the resultant spinning waves were quite high when compared with previous data. A possible explanation of this behavior is being sought via a model which considers the spacial vaporization history of different propellants based on injection velocity.

No study of the nonlinear effects of combustion instability would be complete with rocket motor tests alone. From a theoretical standpoint, a model has been investigated which assumes a rotating detonation wave in an annular chamber. In the final analysis, this model was not applicable to cases of interest in liquid propellant rocket motors without major revision. This analysis is presented in detail in Appendix D.

A new mathematical technique has come to our attention which should prove extremely useful in the analysis of non-linear combustion instability. The technique is known as the characteristic coordinate perturbation method. Much of the development of this method was accomplished by M. J. Lighthill and C. C. Lin.

The method involves a recasting of the variables with the characteristic coordinates as the new independent variables and the space and time variables are now dependent variables. This is necessary for mathematical rigor but will not be explained here. All dependent variables are written as a Taylor series in an amplitude factor and a standard perturbation analysis is made.

Crocco's time lag theory is employed and the parameters $\mathcal{T}$ and

n are introduced when a solution of the combustion instability problem is attempted.

At the start, a study of the longitudinal mode only has been attempted but a study of the transverse mode as well is intended. A non-linear analysis of oscillating flow in nozzles will be associated with this study.

So far, only the first order solution has been obtained for the longitudinal case, but the second order solution should be obtained in the very near future. As would be expected, the first order solution agrees with that obtained by Crocco by a separation of variables technique. That is, certain relationships between the time lag, interaction index, and frequency are found which serve as a criterion for linear instability. It is expected that the non-linear solution will give certain relations between these same parameters which will serve as a criterion for non-linear instability. Also, information about the existence of shock waves in the chamber should be obtained.

Several basic experimental approaches to individual aspects of this complex nonlinear problem are also being investigated. One study deals with the determination of the instantaneous droplet diameter for injection into a oscillating pressure chamber. This study was initiated on a theoretical basis, which indicated a relationship between the instantaneous droplet diameter and the burning rate see(Appendix E).

This first study uses the resonating chamber apparatus originally used for another purpose by the Jet Propulsion Laboratory, (see fig. 35). In principle, the apparatus consists of a variable-length chamber and a controlled frequency gas flow. An internal siren, within the inlet gas line, modulates the flow in a nearly sinusoidal manner (although within the chamber the pulses

steepen into characteristic longitudinal shocks). With the proper frequency and chamber length relationships oscillating pressure amplitudes of 25 psi peak-to-peak can be produced with this apparatus in the modified condition. Fig. 36 shows some typical resonance curves of variable length operation.

Some of the modifications are as follows: Initially, because the gas inlet line and exhaust lines also had associated resonanse frequencies, in addition to the chamber itself, the exhaust line was eliminated and the exhaust was located near the perimeter of the chamber and holding the spray part. This was a temporary arrangement while tests involving the influence of chamber pressure fluctuations on the instantaneous liquid mass flow were being made. It was expected that the gas flow could then be reversed so that it would flow in the same direction as the liquid spray and hence provide a minimum of disturbance. However, the amplitude of the pressure oscillations was reduced considerably when this modification was made (order of 1/2 of former amplitudes) and therefore more extensive modifications were in order. Further redesign is being undertaken at this time in order to reorient the the gas direction to that of droplet direction. This is an important consideration in the droplet observations.

Currently droplet size observations are being carried out under steady-state conditions. Using a spray tank, capable of attaining rocket chamber pressures, the same injector spuds as used in the pulsed limits testing are being evaluated. This apparatus was previously used to evaluate conical spray jets (ref. 12). The parameters varied are injector pressure drop, distance downstream from the point of injection, tank pressure, and the ability to change the fluid properties. Observations are made through quartz windows, which have caused several months delay in the obtaining of the required data.

The reason is that the window material and homogeneity are very critical in maintaining the integrity of the narrow beam of light. (The light scattering technique, ref. 13, is used to determine the D_{32} or Sauter Mean diameter) Imperfections in the original quartz windows (even thought optical grade #1 in quality) caused the circular beam of light to be increased in size and altered in shape. After a number of tests, it was found that homosote quartz (unrolled in manufacture as was the case for optical grade #1) solved the problem. These steady-state tests are nearing completion and will be reported in the next report.

The other basic studies mentioned include the determination of the degree of vaporization of an impinging jet spray under steady and unsteady conditions. The unsteady condition tests would also be concerned with the displacement of vaporized propellant as compared to the liquid droplets. Fig. 37 shows a schematic of this experimental apparatus. An inert gas with controlled turbulence is seen to surround the incoming impinging liquid spray. The liquid is temperature and pressure controlled so that varying degrees of vaporization may be obtained. Measurements will use schlieren techniques by means of windows in the pressurized test chamber to determine the presence of vaporization. This experiment is currently in progress with unsteady aspects of the apparatus in the design phase. The pulsed stability limits tests have already indicated the importance of obtaining these data.

APPENDIX A: Effect of the Approximation to the Velocity Distribution in
Instability Calculations

In order to theoretically analyse stability limit data, it is necessary
that the velocity distribution in the chamber be known. The theoretical treat-
ment of the longitudinal stability limits in Reference II contains the velocity
distribution in the integral forms

$$A(L,\omega) = \int_0^L \bar{u}(x) \cos\left[\frac{\omega(L-2x)}{\bar{c}_0}\right] dx \qquad (1)$$

$$B(L,\omega) = \int_0^L \bar{u}(x) \sin\left[\frac{\omega(L-2x)}{\bar{c}_0}\right] dx \qquad (2)$$

$$C(L) = \int_0^L \bar{u}(x) dx \qquad (3)$$

where L is chamber length, x the axial distance, $\bar{c}_0$ the average
chamber speed of sound of the chamber gases, and ω the frequency of oscillation
at the stability limits. These integrals appear in equations of the form

$$n = f_1\left(L, \frac{\omega L}{\bar{c}_0}\right) \; ; \; \frac{\bar{c}_0 \bar{\tau}}{L} = f_2\left(L, \frac{\omega L}{\bar{c}_0}\right) \qquad (4)$$

where n is the interaction index and $\bar{\tau}$ the sensitive time lag. It
has been convenient to replace an observed velocity distribution by a step
function at the point of maximum velocity gradient, with the view in mind
to simplify the theoretical treatment. However, the validity of the assumption
breaks down at short chamber lengths. Since a reasonable representation of the
actual velocity distribution is available in many cases, it is desirable to
investigate the errors introduced by several approximations.

Two velocity distributions were chosen and are presented in Figure 38.
If this is represented "exactly" by an m+I straight line approximation,
equations (I), (2) and (3) may be computed from the following formulas:

$$A(L,\omega) = UR - TS \qquad (5)$$

$$B(L,\omega) = TR - US \qquad (6)$$

$$T = \sin\frac{\omega L}{\bar{c}_0} \; , \quad U = \cos\frac{\omega L}{\bar{c}_0} \qquad (7)$$

$$R = \frac{\bar{c}_0}{2\omega}\left[\bar{u}_e \sin \frac{2\omega L}{\bar{c}_0} + \frac{\bar{c}_0}{2\omega}\sum_{i=1}^{m-1} D_i \left(\cos \frac{2\omega x_{i+1}}{\bar{c}_0} - \cos \frac{2\omega x_i}{\bar{c}_0}\right) + \right.$$

$$\left. + \frac{\bar{c}_0}{2\omega} D_m \left(\cos \frac{2\omega L}{\bar{c}_0} - \cos \frac{2\omega x_m}{\bar{c}_0}\right)\right] \tag{8}$$

$$S = \frac{\bar{c}_0}{2\omega}\left\{\frac{\bar{c}_0}{2\omega}\left[\sum_{i=1}^{m-1} D_i \left(\sin \frac{2\omega x_{i+1}}{\bar{c}_0} - \sin \frac{2\omega x_i}{\bar{c}_0}\right) + \right.\right.$$

$$\left.\left. + D_m\left(\sin \frac{2\omega L}{\bar{c}_0} - \sin \frac{2\omega x_m}{\bar{c}_0}\right)\right] - \bar{u}_e \cos \frac{2\omega L}{\bar{c}_0}\right\} \tag{9}$$

$$C = \frac{1}{2}\left[\sum_{i=1}^{m-1} D_i \left(x_{i+1}^2 - x_i^2\right) + D_m\left(L^2 - x_m^2\right)\right] + $$

$$+ \sum_{i=1}^{m-1} E_i \left(x_{i+1} - x_i\right) + E_m\left(L - x_m\right) \tag{10}$$

$$D_i = \left(\bar{u}_{i+1} - \bar{u}_i\right)/\left(x_{i+1} - x_i\right) \tag{11}$$

$$E_i = \left(\bar{u}_i x_{i+1} - \bar{u}_{i+1} x_i\right)/\left(x_{i+1} - x_i\right) \tag{12}$$

where $\bar{u}_i$ and $\bar{x}_i$ are the coordinates of the endpoints and L is assumed to lie between X_m and X_{m+1} . A four straight line approximation was assumed to be "exact" for this analysis. In addition three approximate distributions were studied.

1. A step function located at the point of maximum velocity gradient.

2. A straight line from $X = 0$, $\bar{u} = 0$ to $X = X_1$, $\bar{u} = \bar{u}_e$ which is adjusted so that the integral of the velocity distribution is exact at the maximum length considered.

3. A step function located so as to fulfill the same condition as in 2.

The computations were carried out on an IBM 1620 computing machine and the results are presented Figure 39. Only the percent error in the minimum interaction index is shown, since the sensitive time lag and frequency

at the minimum point are primarily determined by length. Errors In the latter two quantities are rarely over 1% .

It is rather surprising to see such strong errors appearing in the minimum Interaction index. These are introduced by the fact that equations (I) and (2) have oscillating integrands. It could have been reasoned beforehand that approximations I or 2 would have been best for B (L,ω), 2 or 3 should be best for C . No single approximation is best over the entire range for A (L,ω). Even so, there appears to be no consistent method for predicting the effect on the interaction index. It appears that the step function at the maximum velocity gradient gives the best overall behavior but still causes errors of nearly 20% at short lengths. As expected, all the approximations improve as the length becomes large.

It is apparent that if accurate data analysis is to be carried out, the velocity distribution should be represented as accurately as possible. This has important consequences since it has been found experimentally that interaction indices lie in a very narrow range (0.7 < n < 1.5), at least for the cases tested. Thus, if it is eve desirable to attempt a correlation of n and τ with propellant type, mixture ratio and injector type, it is imperative that the velocity distribution be known quite accurately.

APPENDIX B: Determination of Characteristic Velocity With Cooled Exhaust Nozzle

The characteristic velocity, c^*, in the rocket chamber can usually be determined by measurement of the chamber pressure p_c, and the propellant mass flow, m. The simple relationship

$$c^* = \frac{p_c A_t g}{\dot{m}}$$

is used. This is derived by an analysis of the nozzle flow which assumes steady, one-dimensional, isentropic flow of a perfect gas with constant specific heats and molecular weight throughout the converging portion of the nozzle. Also, negligible Mach number at the nozzle entrance and Mach number one at the throat are assumed.

However, with highly-cooled exhaust nozzles, this relationship has not given realistic values for c^*. Therefore, an attempt has been made to establish a relationship which satisfactorily determines the characteristic velocity for the special case of considerable deviation from isentropic nozzle flow. While removing the isentropic assumption, we should logically keep all assumptions which do not contradict the postulate that heat transfer exists. Namely, a steady, one-dimensional flow of a perfect gas with constant specific heats and molecular weight and negligible Mach number at the nozzle entrance are assumed. Note that with cooling, the sonic point will be slightly upstream of the throat.

In the case of the cooled nozzle, in addition to measurements of the chamber pressure and the propellant flow rate, coolant flow rate and the

temperature difference between the incoming coolant and the outgoing coolant are determined. This allows us to calculate the amount of heat transferred to the nozzle walls in steady-state operation. However, we are interested only in the heat transferred upstream of the throat, since disturbances in the diverging portion do not affect chamber conditions and hence will not enter the relationship for c^*. Although $\dot{Q}$ (the total heat transferred to the nozzle walls per unit time) will be measured, a theoretical prediction of f (the percentage of heat transferred upstream of the throat) will be necessary.

The analysis proceeds as follows:

For steady state operation,

$$\dot{m} = \rho u A. \tag{1}$$

For a perfect gas with constant specific heat,

$$P = \rho RT \tag{2}$$

and

$$\frac{\Delta S}{R} = \frac{1}{\gamma - 1} \ln \frac{T}{T_{ref.}} = \ln \frac{\rho}{\rho_{ref.}} \tag{3}$$

The following relations define Mach number, stagnation temperature, and characteristic velocity.

$$M = \frac{u}{a} \tag{4}$$

$$T_o = T + \frac{u^2}{2c_p} \tag{5}$$

$$c^* = \sqrt{\frac{R T_c}{\gamma}} \left(\frac{2}{1 + \gamma} \right)^{\frac{1 + \gamma}{2(1 - \gamma)}} \tag{6}$$

We will consider the chamber pressure, p_c, and the chamber temperature, T_c, as the stagnation conditions at the nozzle entrance. This

is in accordance with the assumption of negligible Mach number at this point.

Combining relations (I) through (6), we may obtain

$$\dot{m} = \frac{P_c A g}{c^*} M \left(\frac{1 + \frac{\gamma-1}{2} M^2}{\frac{1+\gamma}{2}} \right)^{\frac{1+\gamma}{2(1-\gamma)}} e^{-\frac{\Delta S}{R}} \left(\frac{T_0}{T_c} \right)^{\frac{3-\gamma}{2(1-\gamma)}}$$

where the entropy is referenced to chamber conditions.

Evaluating the variables at the throat, we obtain

$$\dot{m} = \frac{P_c A_t g}{c^*} \left\{ M_t \left(\frac{1 + \frac{\gamma-1}{2} M_t^2}{\frac{1+\gamma}{2}} \right)^{\frac{1+\gamma}{2(1-\gamma)}} e^{-\frac{\Delta S_t}{R}} \left(\frac{T_{0_t}}{T_c} \right)^{\frac{3-\gamma}{2(1-\gamma)}} \right\} \qquad (7)$$

Note that in the isentropic case

$$M_t = 1 \qquad\qquad \Delta S_t = 0 \qquad\qquad T_{0_t} = T_c$$

and relation (7) reduces to the well known

$$\dot{m} = \frac{P_c A_t g}{c^*}$$

By defining

$$c^*_{effective} = \frac{c^*}{\left\{ M_t \left(\frac{1 + \frac{\gamma-1}{2} M_t^2}{\frac{\gamma+1}{2}} \right)^{\frac{\gamma+1}{2(1-\gamma)}} e^{-\frac{\Delta S_t}{R}} \left(\frac{T_{0_t}}{T_c} \right)^{\frac{3-\gamma}{2(1-\gamma)}} \right\}}$$

$$(8)$$

we may write (7) as

$$\dot{m} = \frac{P_c A_t g}{c^*_{effective}}$$

For small deviations of the throat Mach number from unity, the deviation of the function

$$F(M_t) = M_t \left(\frac{1 + \frac{\gamma-1}{2} M_t^2}{\frac{\gamma+1}{2}} \right)^{\frac{\gamma+1}{2(1-\gamma)}}$$

from unity is extremely small (See Ref. 14). So we shall assume $F(M_t) = 1$.

Considering conservation of energy, we have $\dot{m}\, c_p (T_c - T_{o_t}) = f\, \mathcal{R}$

This gives us the relation

$$\left(\frac{T_{o_t}}{T_c} \right)^{\frac{3-\gamma}{2(1-\gamma)}} = \left(1 - \frac{f\, \mathcal{R}}{\dot{m}\, c_p\, T_c} \right)^{\frac{3-\gamma}{2(1-\gamma)}}$$

Under our one-dimensional assumption, the following relationship may be used

$$-\frac{\Delta S_t}{R} = \int_{ENTRANCE}^{THROAT} \frac{1}{RT} \frac{\delta Q}{\delta x} dx$$

where $\dfrac{\delta Q}{\delta x}$ is the amount of heat transferred to the wall per pound mass of fluid per unit length of nozzle.

Since most of the heat is transferred near the throat, a reasonable approximation is

$$-\frac{\Delta S_t}{R} \approx \frac{1}{RT_t} \int_{ENTRANCE}^{THROAT} \frac{\delta Q}{\delta x} dx = \frac{f\, \mathcal{R}}{\dot{m}\, R\, T_t}$$

Now

$$T_t = \frac{T_{o_t}}{1 + \frac{\gamma-1}{2} M_t^2}$$

Based on experiment we find that $\left| \dfrac{T_c - T_{o_t}}{T_c} \right|$ is of the order of $\dfrac{1}{100}$. Also $M_t \approx 1$, so that we may approximate

$$T_t \approx \frac{2}{\gamma+1} T_c$$

and

$$-\frac{\Delta S_t}{R} \approx \frac{\gamma+1}{2} \frac{f\, \mathcal{R}}{\dot{m}\, R\, T_c}$$

Within our approximation we can write (8) as

$$\frac{c^*_{effective}}{c^*} = \left(1 - \frac{f\mathcal{R}}{\dot{m}\,c_p T_c}\right)^{\frac{3-\gamma}{2(\gamma-1)}} e^{-\frac{\gamma+1}{2}\frac{f\mathcal{R}}{\dot{m}RT_c}} \quad (9)$$

$\mathcal{R}$ and $\dot{m}$ are measured experimentally while c^*, T_c, c_p, γ, and R may be calculated theoretically for any fuel-oxidizer combination and any chamber pressure. Only f remains undetermined.

The relationship for heat transfer per unit time for the case of an axisymmetric nozzle followed by an axisymmetric constant-area section is

$$\mathcal{R} = \int_{NOZZLE} h_N (T_0 - T_w)\,\pi D\,dx + \int_{\substack{CONSTANT \\ AREA\ SECTION}} h_p (T_0 - T_w)\,\pi D\,dx$$

where h is the convective heat transfer coefficient and D is the diameter of the local section.

By definition

$$f = \frac{\int_{\substack{CONVERGING \\ PORTION}} h_N (T_0 - T_w)\,\pi D\,dx}{\mathcal{R}}$$

In the special case of interest, the diverging portion of the nozzle is much shorter than either the converging portion or the constant area section (See Fig. 20). Therefore, the heat transferred while the gas is in this portion will be neglected, thus

$$f = \frac{\int_{\substack{CONVERGING \\ PORTION}} h_N (T_0 - T_w)\,\pi D\,dx}{\int_{\substack{CONVERGING \\ PORTION}} h_N (T_0 - T_w)\,\pi D\,dx + \int_{\substack{CONSTANT \\ AREA \\ SECTION}} h_p (T_0 - T_w)\,\pi D\,dx} \quad (10)$$

The variation of $(T_0 - T_w)$ is not easily determined. However, the flow is nearly isoenergetic and assuming the variation in wall temperature is

small, we can write

$$(T_0 - T_w) = \text{constant throughout}$$

Thus equation (10) may be written as

$$f = \frac{\displaystyle\int_{\substack{\text{CONVERGING} \\ \text{PORTION}}} h_N \, \pi D \, dx}{\displaystyle\int_{\substack{\text{CONVERGING} \\ \text{PORTION}}} h_N \, \pi D \, dx + \int_{\substack{\text{CONSTANT} \\ \text{AREA SECTION}}} h_p \, \pi D \, dx} \tag{11}$$

The variation of D with X is known for any particular geometry. All that remains to be determined is h_N and h_p.

Fully-developed turbulent pipe flow was assumed in the constant area section so that the convective heat transfer coefficient was determined in the standard manner. A useful form for the relation[*] is

$$h_p = \left[0.023 \left(\frac{\mu^{0.2} c_p}{P_\lambda^{0.6}} \right)_0 \left(\frac{P_c \, g}{c^*} \right)^{0.8} \frac{D_t^{1.6}}{D^{1.8}} \sigma \right]$$

where h_p is in $Btu/in^2 \, sec \, {}^oF$ and the other units are chosen accordingly. σ is a factor which accounts for variation of the properties through the boundary layer. Since the diameter in this portion is constant, h_p is constant with χ and one of our integrals is readily evaluated.

$$\int_{\substack{\text{CONSTANT} \\ \text{AREA SECTION}}} h_p \, \pi D \, dx = h_p \, \pi D \, L_p$$

In order to evaluate h_N, a relationship derived by D. R. Bartz (see Ref. 15 and 16) for determining heat transfer coefficients in rocket

nozzles was used. According to Bartz

$$h_N = \left[\frac{0.026}{D_t^{0.2}} \left(\frac{\mu^{0.2} c_p}{P_r^{0.6}} \right)_0 \left(\frac{P_c \, g}{c^*} \right)^{0.8} \left(\frac{D_t}{r_c} \right)^{0.1} \right] \left(\frac{A_t}{A} \right)^{0.9} \sigma$$

where r_c is the radius of curvature at the throat.

Here D is a function of X and $D^{-0.8}$ will appear in our integrand. For simplicity in the calculation, the nearly conical nozzle in the case of interest was assumed to be exactly conical so that we could say

$$D = a + bx$$

where a and b are constants related to the geometry. Now we have sufficient information to evaluate the second integral and f is determined from (11).

Now, it is possible to determine $c^*_{effective}$ from (9).

List of Symbols

c^*	characteristic velocity
p	pressure
$\dot{m}$	mass flow
A	area
g	conversion factor 32 ft/sec^2
$\dot{Q}$	heat transferred to nozzle per unit time
f	percentage of heat transferred upstream of sonic point
ρ	density
u	velocity
T	temperature
R	gas constant
a	speed of sound

M	Mach number
c_p	specific heat at constant pressure
c_v	specific heat at constant volume
γ	ratio of specific heats
s	entropy
h	heat transfer coefficient
D	diameter of nozzle (local)
μ	coefficient of viscosity
P_r	Prandtl number
k	coefficient of thermal conductivity
x	axial distance
L	length of section
r_c	throat radius of curvature

Subscripts:

c	chamber conditions
o	stagnation conditions
t	evaluated at throat
N	nozzle
P	constant area pipe section
w	condition at wall of nozzle

APPENDIX C: Basic Pulse Studies

To study the effects of non-linear combustion instability,
it is necessary to disturb the conditions within the combustion chamber
with a controlled perturbation. Methods to produce such disturbances
have been used in the rocket industry (Ref. 23 and 33) to rate the tendency
of a rocket motor to go unstable. In order to look more deeply into
the problem of non-linear combustion instability, it is first essential
to evaluate the pulse technique itself. The choice in this study was
to use the powder charge-burst disc system to produce the pulse, rather
than a jet of inert gases.(which was felt would actually alter the
combustion conditions). The experimental approach to evaluating the
effects within a rocket chamber, when that chamber is pulsed, is based
on simulating the conditions and geometry of the operational hardware.

The apparatus used was completely described in Reference 2
and consisted of the cylindrical portion of the operational rocket
motor with the nozzle replaced by a glass window to provide for
schlieren photographs of the gas dynamic effects associated with the
pulse (see schematic, Figure 40). In place of the injector plate a
polished optical face (necessary for the schlieren photographs) was
substituted. This had a limited number of openings for pressure and
velocity measurements. A schlieren photograph of the initial shock
wave as it traveled across the chamber from the tangentially oriented
entrance port was shown in Ref. 2. Using a number of such tests, it
was possible to show the travel history of shock waves generated under
a variety of initial chamber pressure conditions.   These data are
shown in Figure 41 and illustrate that even with variations in the

initial chamber pressure from 1 to 20 atmospheres, the wave still travels almost directly across the chamber. Actually at one atmosphere the point of impact on the opposite side of the chamber is more than 180° from the entrance port, while as the initial chamber pressure increases this impact point moves to values below 180°.

One hope of the schlieren approach was to observe the spinning first tangential mode oscillations that were set up in the cylindrical chamber following the initial strong shock. However, the grain charge used in producing the shock (although composed of smokeless pistol powder) prevented any schlieren records after the initial shock because of the associated smoke and turbulence.

In order to determine the nature of the spinning first tangential mode, the optical injector face was replaced with an injector plate designed designed for as many as eight crystal pressure transducers. This injector plate is shown in Figure 42, where transducers can be located at one inch intervals extending from the center of the injector.

In order to record the information resulting from these tests, the FM tape recorder system was used. Since it was of interest to record both the steady-state pressure and the unsteady component of pressure at each station, the number of stations was limited to three by the 7 channels available on the tape. Thus, the signal from each of the crystal gages (output nominally 10 millivolts/psi) was split, one half routed through a low-pass filter (cutoff above 500 cps) and the other half limited by a Kronite bandpass filter. The bandpass filter allowed for independent study of the fundamental mode of the oscillation and the harmonics produced. The time histories of the steady-state pressures and the

frequencies of which the wave was composed were studied for comparison with the theoretical work of Moore and Maslen (see Ref. 10), and such comparisons are covered in Ref. 9. What is important from the point of view of evaluating the effects of the spinning tangential wave, when it is introduced into the combustion chamber of a rocket motor, is that only the fundamental frequency recorded in these tests is of major significance.[*]

In the following discussions we will only consider the pulse entering the chamber tangentially oriented; i.e., oriented in such a fashion as to be tangent to the injection diameter of the operational rocket injector. The radial pulse orientation was also tested and the results were as follows: the frequencies produced corresponded to the radial mode with considerable traces of other frequencies present (standing or spinning tangential mode) and the amplitude was relatively small compared to the amplitudes reached using similar pulses to produce the spinning tangential mode ($<20\%$ at 5 millisec). One other arrangement is also used in order to produce the standing tangential wave. This uses the tangential orientation, but a diametral baffle is placed in the four inch long cylindrical chamber section extending to within 1/8" of the window end. This method produces a strong standing wave pattern that decays more slowly than in the spinning case. These tests are covered in detail in Ref. 9. It should be noted from the two experimental arrangements just mentioned, that if it is desirable to provide either radial or standing tangential mode oscillations in a rocket motor in order to test susceptibility to either of these modes, the pulse technique

---

[*]Although the variation of steady-state pressure and the higher harmonics with time could be observed, they constituted less than 10% of the total pressure effects. This, of course, does not account for the effects on combustion within a pulsed rocket chamber.

appears adequate for the task.

So far in this discussion, it has been implied that the pulse technique provides a reasonable method for producing spinning tangential oscillations. Let us look at the records from the tests in the nitrogen filled cylindrical chamber to see what the waves produced are like. Figure 43 illustrates a typical test using a 30 grain charge and a 10,000 psi burst diaphragm to produce the pulse. The variation of the amplitude of the unsteady component of pressure at stations 5, 3, and 1 is readily apparent. Actually one would expect the amplitude to be negligible at station 1 (injector center) based on acoustic theory (or Ref. 10). However, any eccentricity of the wave would produce unsteady pressures amplitudes at this station. Figure 44 compares acoustic theory to the experimental values obtained with the 30-10 charge-diaphragm combination. In this comparison station 3 is used as the reference station.

In all the records, the first few cycles of the rotating wave tended to vary erratically in amplitude or alternated between reaching a higher positive pressure on one cycle and then dropping to a lower negative pressure on the next. These effects are believed due to the decay of the initial shock wave. Exponential decay is present for all of the spinning waves produced by the charge-diaphragm system. Nitrogen pulsing with large volume tended to produce constant amplitudes for a period prior to the exponential decay. The standing wave produced, tended to exponentially decay at first and then proceeded to decay at a low linear rate.

For the grain charge-burst diaphragm system the spinning

tangential mode frequency, especially for low initial chamber pressure conditions, can be predicted with only limited accuracy (since the speed of sound depends on the gas mixture for determining the final temperature, molecular weight and γ thus requiring an accurate knowledge of how much powder has burned). At higher chamber pressure, however, where the mass of powder burned is small compared to the mass of inert gas present in the chamber, the experimental frequency compares well with that predicted. Another experimental arrangement where frequencies were accurately predicted utilized nitrogen pressure up to 2000 psi to burst the precision diaphragms. Of course, no problems concerning temperature, molecular weight or γ were present with the all nitrogen system.

In varying the grain charge-diaphragm combinations, it was noted that in addition to the change in the initial value of the peak-to-peak pressure, the rate of exponential decay also varied. Figure 45a illustrates the pressure amplitude time histories for the three charge-diaphragm combination chosen for the early pulse limits testing (see page 23). Here it can be seen that the initial amplitudes of the peak-to-peak pressure vary in the same order as the grain charges, while the decay rates vary in a far less obvious fashion. Also evident is a certain amount of scatter about the mean slope shown. When fired into the nitrogen filled chamber the scatter with the charge-diaphragm system normally fell within ± 10% of the mean. Using the nitrogen shock tube to rupture the diaphragm, scatter was reduced to a few percent.

Using the 30-10 pulse in the chamber under conditions of varying initial chamber pressure, major changes in both the initial peak-to-peak amplitude and the decay rate are indicated. These data are presented in Fig. 45b.

Both the data on variations in chamber pressure (Fig. 45b) and the grain charge-diaphragm combinations (Fig. 45a) illustrate the necessity for obtaining complete information on the pulse entering the chamber of an operating rocket motor if pulsed limits testing is to have any meaning. Should the chamber pressure be altered between two sets of tests, it is shown that the pulse produced can exhibit far different initial amplitudes and decay rates. Thus, any stability limits determined could shift drastically.

APPENDIX D: Non-linear Transverse Combustion Instability

This aspect of the work has been concerned with an analysis of the regime conditions once the transverse instability is fully established in the rocket motor. No attempt is being made here to predict the onset of instability.

Once the instability is fully established, high-amplitude waves are present and non-linear effects are important and can't be neglected. Therefore, the problem cannot yet be solved by rigorous mathematical means, so that some simplifying assumptions are necessary.

Transverse instability is generally a three-dimensional phenomena. However, for the first analysis, one would like to simplify the problem and investigate a two-dimensional case. This can be done by looking at a rocket chamber in the form of a thin cylindrical annulus. In this case, we have an axial direction and a tangential direction. Radial effects may be neglected.

Of course, this is inherently different from a full chamber where radial effects are important. However, a good qualitative under-standing of the problem may be obtained. Also, annular chambers may some day be constructed, so that the problem has practical value in that sense.

In an actual liquid propellant rocket motor, atomization, evaporation, mixing and burning are occurring with some spatial distri-bution. We will simplify the situation by assuming that a premixed gas is being uniformly injected. This has already been accomplished in the laboratory at Princeton in another project involving liquid propellant

rocket combustion processes. Premixing chambers and porous plug injectors were employed. This gives hope that any theory developed may be checked in the laboratory using well-established techniques.

We will concern ourselves only with waves spinning in the transverse direction. The circumference to wavelength ratio is always an integer. The waveform will be assumed to be a shock followed by an expansion. It is further assumed that all combustion occurs immediately after the shock wave. So essentially we have a detonation wave. Even though it is felt that (according to the strictest definition) detonation waves will not occur in the rocket chamber, this assumption is made in this first analysis for the sake of simplification. This detonation will be assumed to be of infinitesimal thickness. It can be characterized by an energy release which will be assumed to be a function of the fuel-oxidizer combination only and independent of thermodynamic functions in the chamber.

Under these assumptions, one need not concern himself with chemical kinetics but only with the mechanics of the flow field.

The perfect gas and constant specific heat assumptions, will be made. Besides the obvious simplifications introduced by these assumptions, an important one is that molecular weights will not appear in our equations, Thus the gases involved need not be specified except for stating the energy release in combustion and the ratio of specific heats.

Since fully developed combustion waves are observed to have constant frequency and exhibit the same waveform with time, we may expect to find steady-state conditions by moving at our wave velocity. So we can fix our frame of reference to the detonation front. In order to draw a schematic of our flow, we may cut our annulus and roll it unto a plane surface. It is necessary to look at only one wavelength of the flow field since the flow

is periodic.

Following a theoretical model proposed by Sommers (Ref.18) for a similar problem, a model was constructed which approximated the wave front by straight line portions, as shown in Fig. 46.

Since the gas is being injected at low subsonic velocities in an axial direction and the wave front moves at supersonic speeds in a tangential direction, any given particle will be swept by the wave more than once, as shown here by the contact surfaces in Fig.46. Assuming, the gas is completely burned the first time it is swept by the shock, one portion of the wave front will be a detonation and the other portion will be a pure shock. The presence of the shock wave may be attributed to the action of the expanding gases behind the detonation.

There is a discontinuity in entropy between the burned gas region and the unburned gas region. In general, a reflected wave is obtained when a pressure wave crosses an entropy discontinuity. In our case, one expects the reflected wave to be an expansion wave since the pressure amplitude should be greater across the detonation portion of the wave front than across the shock portion of the wave front. All expansions will be assumed isentropic. Therefore, these reflected waves are Prandtl-Meyer expansion fans.

A resemblance can be seen between the flow field immediately behind the shock portion of the wave front and the flow over a body of the same shape as our contact surface. This leads one to wonder what happens when the combustion is so energetic, and the burned gas expands to such an extent, that the boundary conditions at the contact surface cannot be satisfied with the weak shock solution. One would then look for the strong shock

solution. However, since the wave front must be continuous, we would not expect a detached shock as would occur in front of a blunt body. We will return to this problem since it arises in cases of interest.

An important consideration concerns the type of detonation wave which is present in the chamber. Experimentally, it is found that if a combustible mixture is ignited at the closed end of a tube, a combustion wave will propagate along the tube and will reach a steady condition which corresponds to the Chapman-Jouget state. It has been argued that if a strong detonation were obtained, it would be unstable. That is, expansion waves would overtake the wave from behind and weaken it to the Chapman-Jouget state where it would be stable with respect to expansion waves from behind. However, if a moving piston followed the detonation wave at a sufficient velocity, a stable strong detonation would be obtained. Thus, the downstream boundary condition may be such as to produce a stable detonation which is not a Chapman-Jouget detonation. In our situation, there is no well-defined downstream boundary condition since the flow is cyclic. Another important point is that the Chapman-Jouget postulate was made on the basis of observation of one-dimensional flows. Here, the flow field is two-dimensional. Therefore, since our field is two-dimensional and our downstream boundary condition is not well defined, we cannot immediately say that the Chapman-Jouget state exists. However, on the basis of two independent experiments, Chapman-Jouget detonations may be expected.

The first of these experiments was performed by Voitsekhovskii (Ref. 17) who examined the problem of maintaining detonations in annular channels. The maximum wave velocity measured corresponded to the Chapman-

Jouget condition which theory points out to be the case of minimum adiabatic velocity. In other cases where the quenching effects should be more pronounced, a velocity closer to the acoustic velocity was measured.

The other set of experiments was conducted by Sommers (Ref. 18) who was interested in the interaction of a detonation wave with a bounding inert gas. This is similar to our problem since the burned gas is essentially an inert gas which bounds the unburned gas.

Sommers allowed two jets, one a explosive mixture, the other an inert gas to flow side-by-side. A detonation wave moved through the explosive gas causing a shock wave to move alongside in the inert gas. The detonation wave moved at Chapman-Jouget velocity.

Usually, weak oblique shocks were obtained in the inert gas. However, in the special case of lean mixtures (hydrogen-oxygen) with a heluim boundary, a strong shock was obtained which moved ahead of the detonation wave.

On the basis of these two experiments, both of which involved two dimensional flow fields and one of which involved waves which were cyclic in nature, we shall proceed by assuming the detonation in our case is the Chapman-Jouget type.

The flow field will be described by average conditions in the following regions (1), (1u), (1b), (2), (2b), (3) as shown in Fig. 46.

The unburned gas **undergoes** an expansion from the injector surface to the detonation front. In order to relate average conditions at the injector surface to the average conditions in front of the detonation, the wave profile must be known. If we wish to stay within the realm of integral relations, this information will never come from our solution. It must be supplied in some manner. The pressure profile will be expressed

as follows:

$$P_i = P_1 + \frac{P_2 - P_1}{n}$$

where n is a parameter of the problem.

If n = 2, the positive amplitude equals the negative amplitude. However, since experiment shows positive amplitudes are greater than negative amplitudes, n > 2 is more realistic. The introduction of this profile parameter n is definitely a weak point of the analysis. Note that this relationship reflects the cyclic nature of the flow.

The axial pressure gradient in the unburned gas is assumed negligible which means the axial component of velocity remains constant in the unburned gas. This is conveniently expressed as:

$$\mathcal{V}_{1u} = \mathcal{V}_i$$

The isentropic relation relates conditions at the injector surface to conditions at the detonation front as follows:

$$\frac{P_1}{P_i} = \left(\frac{\rho_1}{\rho_i}\right)^{\gamma}$$

The conservation equations may be written for the detonation.

Continuity:

$$\rho_{1u} u_{1u} = \rho_2 u_2$$

Axial Momentum:

$$\mathcal{V}_{1u} = \mathcal{V}_2$$

Transverse Momentum:

$$P_{1u} + \rho_{1u} u_{1u}^2 = P_2 + \rho_2 u_2^2$$

Energy:

$$\frac{\gamma}{\gamma-1} \frac{P_{1u}}{\rho_{1u}} + \frac{u_{1u}^2}{2} + q = \frac{\gamma}{\gamma-1} \frac{P_2}{\rho_2} + \frac{u_2^2}{2}$$

Where q is the energy released per unit mass in combustion, u is the transverse component of velocity and v is the axial component.

The Chapman-Jouget condition is conveniently expressed as:

$$u_2^2 = \gamma P_2 / \rho_2$$

which tells us the velocity behind the detonation is sonic.

The equations are non-dimensionalized by the parameters P_i, ρ_i and $a_i \left(= \sqrt{\gamma P_i / \rho_i} \right)$ where the last term is really dependent on the other two terms. This gives eight unknowns in eight equations with the four parameters γ/a_i^2, v_i/a_i, γ and n. Then the following eight quantities may be solved for:

P_{1u}/P_i, ρ_{1u}/ρ_i, u_{1u}/a_i, v_{1u}/a_i, P_2/P_i, ρ_2/ρ_i, u_2/a_i, and v_2/a_i.

Also, using the isoenergetic relation applied across the region between the injector surface and the detonation front, we may determine the wave velocity, V_s.

$$\frac{\gamma}{\gamma-1} P_i / \rho_i + V_s^2/2 = \frac{\gamma}{\gamma-1} P_{1u}/\rho_{1u} + u_{1u}^2/2$$

The wave velocity V_s appears in this relation because of the change of the frame of reference.

There are two interesting points so far. First, conditions in the region of the detonation front have been determined without considering the other regions. This is so, because axial pressure gradients were neglected. If the axial pressure gradient was not zero, conditions at the detonation would be affected even in the Chapman-Jouget state which means sonic flow behind the detonation. Conditions in front of the wave would be affected through these axial pressure gradients.

The second interesting point is that the solution is independent of the wavelength which agrees with the experimental findings of B. V. Voitsekhovskii, who measured the same velocity for different modes. This is one of the inherent differences between the annular chamber and the full chamber. Of course, the difference is attributed to the radial effects.

Therefore, one must be careful in drawing analogies between the annular chamber and the full chamber.

The shock angle, θ, can be determined once conditions in region (1b) are known. The standard matching conditions across the contact surface relate conditions at (1b) to conditions at (1u) while the isentropic and isoenergetic relations relate conditions at (1b) to conditions at (2).

Matching Conditions:

$$P_{1u} = P_{1b} \equiv P_1$$

$$v_{1u}/u_{1u} = v_{1b}/u_{1b}$$

Isentropic Relation:

$$P_2/P_1 = \left(\rho_2/\rho_{1b} \right)^{\gamma}$$

Isoenergetic Relation:

$$\frac{\gamma}{\gamma-1} P_2/\rho_2 + \frac{u_2^2 + v_2^2}{2} = \frac{\gamma}{\gamma-1} P_1/\rho_{1b} + \frac{u_{1b}^2 + v_{1b}^2}{2}$$

Conditions at (1u) and (2) have already been determined, so that, by using the same non-dimensionalization technique as before, four relations in four unknowns are established. Therefore conditions in region (1b) are easily determined.

The solution of the rest of the problem requires an iteration technique. For convenience, the shock angle was chosen as the iteration parameter. If the shock angle is specified, the following conservation equations applied across the shock may be used to solve for conditions in region (2b).

Continuity:

$$\rho_{1b}\left(u_{1b} \sin\theta - v_{1b} \cos\theta \right) = \rho_{2b}\left(u_{2b} \sin\theta - v_{2b} \cos\theta \right)$$

Axial Momentum:

$$u_{1b} \cos\theta + v_{1b} \sin\theta = u_{2b} \cos\theta + v_{2b} \sin\theta$$

Transverse Momentum:

$$P_1 + P_{1b}\left(u_{1b}\sin\theta - v_{1b}\cos\theta\right)^2 = P_{2b} + P_{2b}\left(u_{2b}\sin\theta - v_{2b}\cos\theta\right)^2$$

Energy:

$$\frac{\gamma}{\gamma-1}\frac{P_1}{\rho_{1b}} + \frac{u_{1b}^2 + v_{1b}^2}{2} = \frac{\gamma}{\gamma-1}\frac{P_{2b}}{\rho_{2b}} + \frac{u_{2b}^2 + v_{2b}^2}{2}$$

The following matching conditions may be applied across the contact surface between regions (2b) and (3).

$$P_3 = P_{2b}$$

$$v_3/u_3 = v_{2b}/u_{2b}$$

The isoenergetic and isentropic relations may be applied to relate conditions at (3) to conditions at (2).

$$\frac{\gamma}{\gamma-1}\frac{P_3}{\rho_3} + \frac{u_3^2 + v_3^2}{2} = \frac{\gamma}{\gamma-1}\frac{P_2}{\rho_2} + \frac{u_2^2 + v_2^2}{2}$$

$$P_3/P_2 = \left(\rho_3/\rho_2\right)^\gamma$$

These last four relations are sufficient to determine conditions in region (3).

Since the shock angle, θ, was specified, two independent methods of computing the contact surface angle, δ, are possible. The two values of δ will, in general, be different and the difference will be used to determine the next choice of the value of θ in the iteration procedure.

The first relation for δ is

$$\tan\delta_A = v_{2b}/u_{2b}$$

The second equation is obtained by relating the angle turned by the flow through the Prandtl - Meyer fan to the contact surface angle

$$\delta_B = \nu_3 - \nu_2 + \arctan v_2/u_2$$

where ν is the Prandtl - Meyer function.

The difference $\delta_A - \delta_B$ indicates the next value of θ. This process is repeated until $\delta_A = \delta_B$.

The complete calculations, including the iteration procedure, was accomplished with the aid of an IBM 1620 computer.

Figure 47 is a graphical illustration of the solution. One curve represents the solution for conditions behind the shock while the other family of curves represent characteristics through the Prandtl - Meyer expansion. The solution to the problem is given by the intersection of these two curves.

However, for larger values of q/a_i^2, the heat release parameters, no intersection and therefore, no solution are obtained. The maximum value of q/a_i^2 which allows a solution is 10. The value of q/a_i^2 which corresponds to a stoichimetric mixture of methane and oxygen is 50. This means all cases of interest give no point of intersection.

Therefore weak oblique shock solutions will not be obtained. Strong solution similar to those obtained by Sommers with his helium gas boundary should be expected. There is a definite similarity between Sommers case and this one. Upon examination of the equations, it is seen that an important similarity parameter is the ratio of the Mach numbers

$$M_{1b}/M_{1u} = \left(u_{1b}/u_{1u}\right)\left(T_{1u}/T_{1b}\right)^{1/2}\left(m_{b1b}/m_{b1u}\right)^{1/2}$$

When this term is below some critical value, the strong solution is obtained. There is no strict critical value since other similarity parameters appear, although they are not as important.

In his experiments, Sommers went below this value by decreasing the molecular weight of the boundary gas and increasing the molecular weight of the hydrogen-oxygen mixture. In the present analysis, a high

temperature boundary gas was considered. Apparently, this problem occurs whenever the boundary gas has a large speed of sound.

It is felt that a series of experiments similar to those of Sommers but concentrating on boundary gases with high speeds of sound would be very helpful. An understanding of the interaction process of the detonation wave and the strong shock is necessary at this stage of the investigation.

The theoretical model, which was originally used and was reported in Ref. 2, produced results applicable only for small amplitude shock waves.

In that case, the shock front was approximated by one straight line, one portion of which was a detonation wave. Average conditions were used and the energy conservation equation across the shock front was written for a volume including the complete shock front. The isentropic relation was used for the expansion region. These assumptions implied the entropy increase across the wave front was small and only low amplitude solutions were allowed.

However, from this it is seen that perhaps this restriction may be avoided by representing the fluid mechanical and thermodynamic properties by some simple function of the spatial variables rather than using average conditions. This is a possible direction to be chosen for future analysis.

List of Symbols

P	pressure
ρ	density
u	transverse velocity
v	axial velocity
q	energy released per pound mass in combustion
a	speed of sound
γ	ratio of specific heats
T	temperature
m_b	molecular weight
n	pressure profile parameter
V_s	shock velocity
θ	shock angle with transverse direction
δ	contact surface angle with transverse direction
ν	Prandtl - Meyer function
M	Mach number

Subscripts:

i	conditions at injector surface
$1u$	conditions in unburned gas before detonation
$1b$	conditions in burned gas before shock
2	conditions behind detonation
$2b$	conditions behind shock
3	conditions after Prandtl - Meyer expansion

APPENDIX E: Some Effects of Injection Droplet Diameter Variation and
Vaporization Rate Perturbations on Combustion Instability

Possibly the most useful results of the Crocco time lag

theory (7) and its subsequent experimental verification are the speci-

fication of the order of magnitude required in the burning rate pertur-

bation and the requirement of the existence of some characteristic time

delay in the combustion process. Indeed, through the experimental verifi-

cation the absolute magnitude of the burning rate perturbation which

actually exists has been pinpointed quite precisely and has been found

to vary only slightly with the type of injection system, at least with

the propellants tested. Such a result is invaluable when it is desired

to investigate actual causes of instability, although it appears to have

been basically ignored in some previous assertions as to the possible

"causes" of instability.

It is well known that rocket combustion is never entirely smooth

but is rendered rough by certain random processes in the chamber such

as turbulence. Processes which are randomly distributed throughout the

chamber (such as the periodic breakup of impinging liquid jets in quiescent

surroundings, the oscillation of a flame front between two unlike burning

droplets, and turbulent mixing) have a frequency spectrum in no way

related to the acoustical properties of the chamber. Although it is

possible to have an unstable system on account of random fluctuations

if the damping functions are also random, such is not the case in rocket

instability theory. It is not unreasonable to suspect then that such

processes can only contribute to combustion noise from which the select

frequency for amplification by some other process originates. Further-

more, there is concern over the possiblity of chemical kinetics playing

a role in unstable operation. Culick (19) has developed a theory based
on the premise that the presence of liquid droplets does not alter the
character of instability in the rocket engine and that the sole supporting
mechanism is chemical kinetics. Such a premise is contrary to the
findings at Princeton (20). Furthermore, the characteristic time that
e ters such a theory is not sufficient to produce the observed character-
istics of liquid rocket instability, even though the order of magnitude
of the perturbation may be sufficient.

Just knowing the approximate form of the burning rate pertur-
bation does not, however, make the task of finding supporting mechanisms
much simpler. In view of the complicated processes taking place within
a rocket chamber, the task of analytically describing all these phenomena
would be a very difficult one, especially since the basic knowledge
concerning these phenomena is very slight. What is more, virtually all
of the knowledge of the detailed processes taking place within a chamber
is based on steady-state operation. In reality there may be significantly
different behavior of these processes in the unsteady state. Still, it
is believed that some insight into the instability problem may be gained
from highly simplified analyses.

An interesting but somewhat disappointing result is obtained
if we attempt an extension of some steady-state concepts into the unsteady
state. For some propellants vaporization appears to be the rate control-
ling step in the conversion from liquid to chamber gases (21). Also,
it is known that the median (some appropriate median) drop size of the
injected spray significantly affects the position of maximum energy release
in the chamber (21,22). It may seem reasonable, therefore, to attempt

the construction of an instability theory around the unsteady operation
of these processes.

Considering only longitudinal modes for simplicity, we may
tacitly accept all of the original theory except the concept of the inter-
action index, the time lag and the droplet drag law. In addition, further
assumptions will be introduced as the development proceeds.

The droplet vaporization law which will be accepted is the D^2
law where the naive assumption is made that the form of the equation is
valid even in the unsteady state. Furthermore, the evaporation constant
will be considered as constant even under fluctuating conditions. Then
we have:

$$\frac{D r_L^*}{D t^*} = -\frac{\bar{\lambda}^*}{\bar{c}_p^* \bar{\rho}_L^*}\left[\frac{\ln(1+\bar{B})}{C}\right]\frac{1}{r_L^*} \tag{1}$$

where the bar superscript denotes an average or steady-state value,
the star denotes a dimensional quantity and the subscript L refers to
the liquid. ρ is density, r is radius, t is time, λ is thermal
conductivity in the film surrounding a droplet, and c_p is the corre-
sponding specific heat at constant pressure. The Spalding transfer
number is $B = \frac{\bar{c}_p^*(T_0^* - T_L^*)}{\Delta l^*}$ where T_0 is the ambient adiabatic combustion
gas temperature and Δl is the latent heat of vaporization of the liquid.
$C = 1 - \frac{r_L^*}{r_c^*}$ where r_c is an outer radius from the droplet which specifies
the position where the outward diffusing vapor reaches T_0. This is
usually specified by a heat transfer correlation, but C will here be
assumed to have an appropriate constant value. It is considered that the
rocket propellants can be lumped mathematically into a single equivalent
monopropellant and that the spray droplet distribution curve approaches

a delta function so that Equation (1) describes all droplets in the spray. Furthermore, the droplets are considered to be injected at their wet bulb temperature which remains constant in time (following the droplet).

If C is sufficiently close to one, the only consistent drag law is Stokes flow which is here uncorrected for outward mass transfer.

$$\frac{Dv^*}{Dt^*} = \frac{9}{2} \frac{\bar{\mu}^*}{\mathcal{S}_L^*} \frac{(u^* - v^*)}{r_L^*}$$ (2)

μ is the viscosity of surrounding gas (some appropriate average), u is the chamber gas velocity, and v is the droplet velocity. Equations (1) and (2) are then basically the equations used by Spalding (23). Writing the continuity equation as in Ref. (7),

$$\frac{\partial \mathcal{S}^*}{\partial t^*} + \frac{\partial (\mathcal{S}^* u^*)}{\partial x^*} = -\frac{\partial \mathcal{S}_L^*}{\partial t^*} - \frac{\partial (\mathcal{S}_L^* v^*)}{\partial x^*} = \frac{\partial w^*}{\partial x^*}$$ (3)

$\mathcal{S}$ refers to the density of the chamber gases of complete combustion (all intermediate gases and liquids are assumed to occupy a negligible portion of the chamber). x is the axial distance from the injector end, $\mathcal{S}_L$ is the mass of liquid per unit chamber volume, and w is the amount of chamber gas liberated per unit time in the region 0 to x .

We also have the relation

$$\mathcal{S}_L^* v^* = \dot{n}^* \mathcal{S}_L^* \frac{4}{3} \pi r_L^{*^3} = G^*$$ (4)

where $\dot{n}$ is the droplet number flow rate, G is the droplet mass flow rate and

$$\dot{n}^* = n^* v^*$$ (5)

where n is the droplet number density. Finally, the droplet continuity equation is:

$$\frac{\partial n^*}{\partial t^*} + \frac{\partial \dot{n}^*}{\partial x^*} = 0$$ (6)

It is convenient to introduce the following nondimensional variables:

$$x = \frac{x^*}{L^*} \qquad t = \frac{t^* c_0^*}{L^*} \qquad u = \frac{u^*}{c_0^*} \qquad v = \frac{v^*}{c_0^*}$$

$$w = \frac{w^*}{\rho_0^* c_0^*} \qquad r = \frac{r^*}{r_{L_0}^*} \qquad \rho_L = \frac{\rho_L^*}{\rho_0^*} \qquad \omega = \frac{\omega^* L^*}{c_0^*}$$

$$\dot{n} = \frac{\dot{n}^*}{\dot{n}_0^*} \qquad \rho = \frac{\rho^*}{\rho_0^*} \qquad G = \frac{G^*}{\rho_0^* c_0^*}$$

$$\tag{7}$$

L is the chamber length from 0 to the entrance of the converging portion of the nozzle, c_0 is the stagnation speed of sound of the chamber gases at the injector end and ρ_0 is the stagnation density. r_{L_0} is the initial injected droplet radius and $\dot{n}_0$ is the injected droplet flow rate. ω is the oscillation frequency.

In terms of the non-dimensional variables we may write equations (1-4, 6) in a more compact form as:

$$\frac{D r_L}{Dt} = -\frac{k_1}{r_L} \tag{8}$$

$$\frac{D v}{Dt} = \frac{k_2 (u-v)}{r_L^2} \tag{9}$$

$$\frac{\partial \rho}{\partial t} + \frac{\partial (\rho u)}{\partial x} = -\frac{\partial \rho_L}{\partial t} - \frac{\partial (\rho_L v)}{\partial x} = \frac{\partial w}{\partial x} \tag{10}$$

$$\rho_L v = \bar{u}_e \dot{n} r_L^3 = G \tag{11}$$

$$\frac{\partial (\dot{n}/v)}{\partial t} + \frac{\partial \dot{n}}{\partial x} = 0 \tag{12}$$

where $\quad k_1 = \frac{\bar{\lambda}^* L^* \ln(1+\bar{B})}{c_p^* \rho_L^* c_0^* r_{L_0}^{*2} C} \quad$ and $\quad k_2 = \frac{9}{2} \frac{\bar{\mu}^* L^*}{\rho_L^* c_0^* r_{L_0}^{*2}}$

$\bar{u}_e$ is the chamber gas Mach number at the entrance to the deLaval nozzle. It is well to note that from here on k_1 and k_2 may be considered empirical constants so as to best fit experimental steady-state data. For many propellants k_1 and k_2 are $O[10^{-1}]$ which will be considered as $O[\bar{u}_e]$. Strictly this is not a correct mathematical statement since neglecting terms of $O[\bar{u}_e^2]$ compared to terms of $O[1]$ is more general than saying that terms of $O[10^{-2}]$ may be neglected. However, from here on k_1 and k_2 will be considered $O[\bar{u}_e]$. We further note that according to Equations (1) and (2) $\dfrac{k_2}{k_1} = \dfrac{q}{2} \dfrac{Pr \ C}{\ln(1+B)} \approx 0.5$ for many propellants where Pr is the Prandtl number.

We now investigate linear neutral stability by introducing small perturbations:

$$r_L(x,t) = \bar{r}_L(x) + r_L'(x,t) = \bar{r}_L(x) + R(x) e^{i\omega t}$$
$$V(x,t) = \bar{V}(x) + v'(x,t) = \bar{V}(x) + \mathcal{Y}(x) e^{i\omega t}$$
$$u(x,t) = \bar{u}(x) + u'(x,t) = \bar{u}(x) + \mathcal{U}(x) e^{i\omega t}$$
$$w(x,t) = \bar{w}(x) + w'(x,t) = \bar{w}(x) + \mathcal{G}(x) e^{i\omega t}$$
$$\dot{n}(x,t) = \bar{n}_o(x) + \dot{n}'(x,t) = 1 + N(x) e^{i\omega t}$$
$$G(x,t) = \bar{G}(x) + G'(x,t) = \bar{G}(x) + \mathcal{H}(x) e^{i\omega t}$$

(13)

First, combining Equations (10) - (12)

$$\frac{1}{\bar{u}_e} \frac{\partial w}{\partial x} = -\left[\frac{\dot{n}}{V} \frac{\partial(r_L^3)}{\partial t} + \dot{n} \frac{\partial(r_L^3)}{\partial x}\right] = -\dot{n} \frac{D(r_L^3)}{Dt}$$

(14)

Then introducing Equation (13) in Equations (8-12 and 14), we obtain the steady-state relations.

$$\bar{V} \frac{d\bar{r}_L}{dx} = -\frac{k_1}{\bar{r}_L}$$

(15)

$$\bar{V} \frac{d\bar{V}}{dx} = \frac{k_2(\bar{u}-\bar{V})}{\bar{r}_L^2}$$

(16)

$$-\frac{d(\bar{\rho}\bar{u})}{dx} = \frac{d}{dx}(\bar{\rho}_L\bar{V}) = -\frac{d\bar{w}}{dx} = \bar{u}_e \frac{d(\bar{r}_L^3)}{dx}$$

(17)

and the perturbation equations after division by the common factor become:

$$\frac{dR}{dx} + \left(\frac{i\omega}{\bar{V}} - \frac{k_1}{\bar{V}\bar{r}_L^2} \right) R = - \frac{\eta}{\bar{V}} \frac{d\bar{r}_L}{dx} \tag{18}$$

$$\frac{d\eta}{dx} + \left(\frac{i\omega}{\bar{V}} + \frac{1}{\bar{V}}\frac{d\bar{V}}{dx} + \frac{k_2}{\bar{V}\bar{r}_L^2} \right)\eta = \frac{k_2 \nu}{\bar{V}\bar{r}_L^2} - \frac{2k_2(\bar{u}-\bar{V})}{\bar{V}\bar{r}_L^3} R \tag{19}$$

$$N + 3R = \mathcal{H} \tag{20}$$

$$\frac{dN}{dx} + \frac{i\omega}{\bar{V}} N = \frac{i\omega \eta}{\bar{V}^2} \tag{21}$$

$$\frac{dg}{dx} = -3\bar{u}_e \left[\frac{d}{dx}(\bar{r}_L^2 R) + \bar{r}_L^2 \frac{d\bar{r}_L}{dx} N + \frac{i\omega}{\bar{V}} \bar{r}_L^2 R \right] \tag{22}$$

The boundary conditions to be attached to Equations (15-22) are:

$$\bar{r}_L(0) = 1 \quad, \quad \bar{V}(0) = \bar{V}_0 \quad, \quad \bar{u}(0) = 0 \tag{23}$$

and

$$R(0) = R_0 \quad, \quad \eta(0) = \eta_0 \quad, \quad N(0) = N_0 \quad, \quad \mathcal{H}(0) = \mathcal{H}_0 \quad, \quad g(0) = 0 \tag{24}$$

The last of the relations of (24) is obvious since $w(x,t) = 0$ at $x = 0$. It must be noted that to strictly adhere to the original time lag theory G_0 should be zero or of higher order since the mass injection rate was considered constant in that theory. However, we shall return to this point later. From Spalding (23) we have the steady state solution to Equations (15) – (17).

$$\bar{V} = \left[\bar{V}_0 + \frac{3\bar{u}_e}{\left(\frac{k_2}{k_1} - 3\right)} \right] \bar{r}_L^{k_2/k_1} - \frac{\bar{r}_L^3 \frac{k_2}{k_1} \bar{u}_e}{k_2/k_1 - 3} + \bar{u}_e \tag{25}$$

$$\bar{u} = \bar{w} = \bar{u}_e(1 - \bar{r}_L^3) \tag{26}$$

where $\bar{\rho} = 1$ has been assumed and is correct to terms of $O[\bar{u}_e^2]$ compared to $O[1]$ in the Crocco theory. The theoretical procedure would be to

assume $\bar{u}(x)$ known and fit a reasonable curve from Equation (26) to it. Then the constants k_1 and k_2 may be reasonably estimated. This is probably a more rational procedure than to theoretically predict k_1 and k_2 since precise values of the input parameters are not known.

The first observation in relations (18) and (19) is that a strong singularity appears in the neighborhood of the point of disappearance of the droplets $\left(\bar{r}_L = o\right)$. Such a singularity did not appear in the Crocco theory because the droplet evaporation process was not considered and the drag law chosen was

$$\frac{Dv}{Dt} = k\,(u-v)$$

where k was considered constant. This troublesome point makes no difference, however, in the final results because of the eventual quantities of interest and because of the many integrations to follow. Staying away from the singular point, an order-of-magnitude investigation seems desirable. The primary reference perturbation is that of the pressure where

$$p(x,t) = 1 + \varphi(x)\,e^{i\omega t}$$

and the reference quantity is $\varphi(o) = \varphi_o$. It is seen from Equation (25) that for reasonable injection velocities v is $O[\bar{u}_e]$. At least for the fundamental mode ω is $O[1]$, being very near π. Then from Equations (15) and (16) $d\bar{r}_L/d_M$ and $d\bar{v}/d_M$ are $O[1]$ and $O[\bar{u}_e]$, respectively. From the acoustic solution p is $O[\varphi_o]$ Assuming R as large as $O[\varphi_o]$, it is seen from Equation (19) that γ is $O[\bar{u}_e\varphi_o]$ in accordance with Crocco's theory. Then from Equation (18) R is $O[\bar{u}_e\varphi_o]$ and from Equation (21) N is $O[\varphi_o]$. Consequently q is $O[\bar{u}_e\varphi_o]$ from Equation (22). But this

is precisely what is desired since this is the order of magnitude expected for the burning rate perturbation from Crocco's theory. Only the handling of the singular point or the magnitude of the boundary conditions can alter this order-of-magnitude argument. It is also important to note that the last two terms of Equation (22) are the primary terms and the first could be dropped now as being of higher order, if it weren't for the presence of the singularity which may alter the order of magnitude of the results.

Since the solution of Equations (21) and (22) depends upon the solution of Equation (19), it is unfortunate that Equation (19) is coupled with R. However, it is a weak coupling as will be seen. Because of the linearity of the equations, the solutions to Equations (18), (19) and (21) may be written:

$$R = R^{(o)} + R^{(1)}$$
$$\eta = \eta^{(o)} + \eta^{(1)} + \eta^{(2)}$$
$$N = N^{(o)} + N^{(1)} \tag{25}$$

where

$$R^{(o)} = \frac{R_o}{\bar{r}_L} e^{-i\omega_o \int_o^x \frac{dx'}{\bar{V}(x')}} \tag{26}$$

and use has been made of Eq. (15). Clearly the term $\int_o^x \frac{dx'}{\bar{V}(x')}$ is something like a total time lag for the propellant burning at station x and for convenience we may define:

$$\tau_t = \int_o^x dx'/\bar{V}(x')$$

Then:

$$R^{(1)} = -\frac{e^{-i\omega \tau_t(x)}}{\bar{r}_L} \int_o^x \frac{\eta(x')}{\bar{V}(x')} \frac{d\bar{r}_L}{dx'} \bar{r}_L e^{i\omega \tau_t(x')} dx' \tag{27}$$

This says that the droplet radius perturbation is made up of two parts:
(1) a term expressing the initial perturbation, which is carried along
at the droplet speed and modified by the size of the droplet, and (2)
a term due to the integrated effects of droplet velocity fluctuation
inasmuch as they effect the position where the perturbation occurs.
Similarly for N,

$$N^{(0)} = N_0 \, e^{-i\omega \tau_t(x)}$$

(28)

and:

$$N^{(1)} = i\omega \, e^{-i\omega \tau_t(x)} \int_0^x \frac{\gamma(x')}{\nabla(x')^2} e^{i\omega \tau_t(x')} dx'$$

(29)

It is clear, however, that:

$$N^{(1)} \frac{d\bar{r_L}}{dx} \gtrsim \frac{i\omega}{\nabla} R^{(1)}$$

so that Equation (22) may be written as:

$$\frac{dq}{dx} = -3\bar{u}_e \left[\frac{d}{dx}(\bar{r_L}^2 R) + \bar{r_L}^2 \frac{d\bar{r_L}}{dx} N^{(0)} + \frac{i\omega}{\nabla} \bar{r_L}^2 R^{(0)} \right]$$

(30)

This is solely a consequence of the vaporization law chosen. For instance,
if a convective heat transfer correlation had been included explicitly,
such a result would not be true. This will have strong effects in the
results since it appears that the leading terms in order of magnitude
in Equation (30) now depend only on what happens at the injector face.
Unless the presence of the singularity alters this reasoning, droplet
vaporization perturbations would have only a secondary effect in the
burning rate perturbation.

Still, the solution for R is required by Equation (30) and R requires a solution for η . We find from Equations (19), (24), and (25):

$$\eta^{(o)} = \eta_0 \frac{\bar{v}_o}{\bar{v}} \bar{r}_L^{k_2/k_1} e^{-i\omega \tau_t(x)} \tag{31}$$

$$\eta^{(1)} = \frac{k_2 \bar{r}_L^{-k_2/k_1} e^{-i\omega \tau_t(x)}}{\bar{v}} \int_0^x \frac{\nu(x') e^{i\omega \tau_t(x')}}{\bar{r}_L^{(2+k_2/k_1)}} dx' \tag{32}$$

$$\eta^{(2)} = -\frac{2 \bar{r}_L^{k_2/k_1} e^{-i\omega \tau_t(x)}}{\bar{v}} k_2 \int_0^x \frac{(\bar{u}-\bar{v}) R(x') e^{i\omega \tau_t(x')}}{\bar{r}_L^{(3+k_2/k_1)}} dx' \tag{33}$$

This states that the droplet velocity perturbation is dependent upon (1) the initial perturbation carried along at the speed of the droplets and modified by the actual speed and droplet size, (2) the variation due to changes in drag through changes in chamber gas speed, and (3) the variation due to changes in droplet size as they affect the drag. The troublesome singularity is now apparent. The strongest place where it appears is in Equation (33) where we first notice from Equation (25) that (u - v) disappears as $\bar{r}_L^{k_2/k_1}$ for usual values of k_2/k_1. Then even if R is regular at $\bar{r}_L = 0$ (which it isn't) $\eta^{(2)}$ has a singularity of $\bar{r}_L^{-k_2/k_1 - 1}$. Such behavior is impossible because a perturbation quantity must remain regular. The behavior is due to the assumed form of the vaporization law which should, in reality, be modified for vanishingly small droplets and due to the vanishing of the volume-to-surface ratio of a droplet as $\bar{r}_L \rightarrow 0$. In fact, it would be impossible for the droplets to have a velocity perturbation larger than that of the gas. However, we may proceed assuming the relation correct, and the singularity will disappear because

of the many integrations to follow. The actual quantity of interest is

$\bar{r}_L^2 R$ as may be seen from Equation (30); this will remain regular

as a consequence of the well-known fact that the volume-to-radius ratio

of a sphere goes to zero as $\bar{r}_L \rightarrow 0$. Consider that the contribution

to $R^{(1)}$ from $\gamma^{(0)}$ is $R\{^1_0\}$, the contribution to $R^{(1)}$ from

$\gamma^{(1)}$ is $R^{(1)}_{(1)}$, etc. Then from Equations (27) and (33):

$$\bar{r}_L^2 R^{(1)}_{(2)} = 2\bar{r}_L \, k_2 \, e^{-i\omega \tau_t (x)} \int_0^x \frac{dr_L}{dx'} \frac{dx'}{\bar{v}^2 \bar{r}_L^{(1-k_2/k_1)}} \int_0^{x'} \frac{(\bar{u}-\bar{v}) R(x'') e^{i\omega \tau_t (x'')}}{\bar{r}_L^{(3+k_2/k_1)}} dx'' \quad (34)$$

which in view of the above remarks and upon inspection is regular if

R has a singularity no worse than $\bar{r}_L^{-(1+k_2/k_1)}$. Further noting

that since τ_t is $O\left[\frac{1}{\bar{u}_e}\right]$ the exponential is a rapidly oscillating

function, the integration reduces the apparent order of magnitude of

Equation (34) by $\bar{u}_e$. Upon inspection $\bar{r}_L^2 R^{(1)}_{(2)}$ is $O[\bar{u}_e^2 \, \psi_0]$ if

$\bar{r}_L^2 R$ is $O[\bar{u}_e \, \psi_0]$ as previously mentioned. This is the reason

for a previous statement of a weak coupling between the R and γ

equations, and assuming regularity as mentioned above we may neglect

$\bar{r}_L^2 R^{(1)}_{(2)}$ as of higher order.

Noting from Equations (27) and (32):

$$R^{(1)}_{(1)} = - \frac{k_2 \, e^{-i\omega \tau_t (x)}}{\bar{r}_L} \int_0^x \frac{\bar{r}_L^{-(k_2/k_1+1)}}{\bar{v}^2} \frac{dr_L}{dx'} dx' \int_0^{x'} \frac{\psi(x'') e^{i\omega \tau_t (x'')}}{\bar{r}_L^{(2+k_2/k_1)}} dx'' \quad (35)$$

the singularity in R is seen to be no worse than $1/\bar{r}_L$ which is not

as severe as $1/r_L^{(1+k_2/k_1)}$. Thus, since this is the worst singular

behavior in R the regularity of $\bar{r}_L^2 R$ is shown. It is now wise

to manipulate Equation (35) in order to obtain a more convenient form.

Using Equation (15) and switching the order of integration,

$$
\bar{r}_L^2 R_{(1)}^{(1)} = k_1 k_2 \bar{r}_L e^{-i\omega \tau_e} \int_0^x \frac{\nu(x'')\, e^{i\omega \tau_e(x'')}}{\bar{r}_L^{(2+k_2/k_1)}}\, dx'' \int_{x''}^x \frac{\bar{r}_L^{\,k_2/k_1}}{\bar{v}^3}\, dx'
$$

or

$$
\bar{r}_L^2 R_{(1)}^{(1)} = \frac{k_2}{k_1}\, \bar{r}_L e^{-i\omega \tau_e} \int_1^{\bar{r}_L} \frac{\nu e^{i\omega \tau_e(\bar{r}_L'')}}{\bar{r}_L''^{(1+k_2/k_1)}}\, \bar{v}\, d\bar{r}_L'' \int_{\bar{r}_L''}^{\bar{r}_L} \frac{\bar{r}_L'^{(1+k_2/k_1)}}{\bar{v}(\bar{r}_L')^2}\, d\bar{r}_L'
$$

Integrating the first integral by parts once we obtain:

$$
\bar{r}_L^2 R_{(1)}^{(1)} = -\frac{k_1 k_2 \bar{r}_L e^{-i\omega \tau_e}}{i\omega} \int_0^x \bar{v}(x'')\, e^{i\omega \tau_e(x'')} \frac{d}{dx''} \left\{ \frac{\nu(x'')}{\bar{r}_L^{(2+k_2/k_1)}} \int_{x''}^x \frac{\bar{r}_L^{\,k_2/k_1}}{\bar{v}^3}\, dx' \right\} dx''
$$

$$(36)$$

where the first term has vanished at both end points by virtue of the form of the second integral and the fact that ν (0) = 0. This will provide a great simplification and a surprising result. First, note that when account is taken of the rapidly oscillating exponential in Eq (35) the expression is apparently of $O[\nu_0]$ where ν is assumed of $O[\nu_0]$. This is contrary to a previously mentioned expectation that R would be $O[\bar{u}_e \nu_0]$. Such behavior is due to the cancelling of the rapidly oscillating exponential in the first integral of Eq (35) when the expression for ν is inserted into the expression for R. However, inspection of Eq (36) shows that $\bar{r}_L^2 R_{(1)}^{(1)}$ is indeed $O[\bar{u}_e \nu_0]$, which is a consequence of the fact that ν is very small near the injector face, and $\bar{r}_L$ is small near the disappearance point of the droplets.

Integrating Eq. (30) and using (24):

$$q^{(x)} = -3\bar{u}_e \left[\bar{r}_L^2 R - R_0 + \int_0^{x} \left(\bar{r}_L^2 \frac{d\bar{r}_L}{dx'} N^{(0)} + \frac{i\omega}{\bar{v}} \bar{r}_L^2 R^{(0)} \right) dx' \right] \quad (37)$$

Then it is clear that the contribution of $\bar{r}_L^2 R_{\omega}^{(1)}$ to the first term

in Eq (37) is $O[\bar{u}_e^2 \psi_0]$ which is insufficient to drive instability as

has been previously discussed. This conclusion is surprising because it

states that perturbations in the vaporization rate due to fluctuating

chamber gas conditions are not strong enough to contribute to instability,

at least from a small perturbation point of view. It can now be seen from

Eq. (37) that only interaction at the injector face remains in the burning

rate expression.

Scala [24] considered the fluid dynamic problem of the injec-

tion system in connection with entropy wave instability. From this work the

following relations are   extracted:

$$\varkappa/_0 = H(\omega) \psi_0 \qquad (38)$$

$$\eta_0 = J(\omega) \bar{v}_0 \psi_0 \qquad (39)$$

Further, from Eqs (20) and (38)

$$N_0 + 3 R_0 = H(\omega) \psi_0 \qquad (40)$$

Where $H(\omega)$ and $J(\omega)$ are functions of frequency and the injection system.

For compatibility with Crocco's theory it is required that $H(\omega)$ be

$O[\bar{u}_e \psi_0]$ or higher in order that to a sufficient degree of approximation

the mass injection rate is constant. For usual injection systems under

high frequency oscillations this is the case and under such conditions $J(\omega)$

is usually $O[\bar{u}_e]$. A further relation connecting the drop size

to chamber gas conditions is required. However, as is well-known, such re-

lations are very rare for the steady-state, and almost nonexistent for un-

steady conditions. Nevertheless, a physically plausible assumption, which

has some experimental justification and was used by Penner [25] , is that

the median drop size (in this work there is no ambiguity concerning the work _median_ since all droplets have the same size) is proportional to the Weber number (based on gas density) to some power, The physical reasoning is that the Weber number is a ratio of gas dynamic forces to surface tension forces, and one expects that the greater such a ratio, the greater will be the spray breakup into smaller droplets. Then we may assume:

$$\frac{r^{*}_{Lo}(t)}{\bar{r}^{*}_{Lo}} = \left[\frac{\rho^{*}_o(t^* - \phi^*)\, V^{*^2}_o(t^* - \phi^*)}{\bar{\rho}_o + \overline{V}^{*^4}_o\, \mathbf{a}} \right]^{-g}$$

where constant surface tension is assumed and a steady-state relation is assumed valid for the unsteady state if a phase lag, ϕ , is included. The amplitude exponent, g , may be, and almost surely would be, a function of frequency but for steady-state is assumed of $O[1]$. The same is true of

ϕ^{*} which is zero in the steady-state by assumption. Then if this relation is accepted, perturbations are introduced, use is made of Eq (39), and the assumption (which is a consequence of Crocco's theory) made that isentropic gas oscillations take place at the injector end, we obtain:

$$R_o = -g\, \varphi_o \left[J(\omega) + \frac{1}{g} \right] e^{-i\omega\phi} \tag{41}$$

If $J(\omega)$ is $O[\bar{u}_e]$, we may neglect it since we only want q to $O[\bar{u}_e\, \varphi_o]$. Then using Eq's (26), (28), (37) and (40) we obtain for a general assumption concerning R_o

$$q = -3\bar{u}_e\, R_o \left[\bar{r}_L\, e^{-i\omega\tau_t(x)} - 1 + \int_o^x \left(\frac{i\omega\bar{r}_L}{V} - 3\bar{r}_L^2\, \frac{d\bar{r}_L}{dx'} \right) e^{-i\omega\tau_t(x')}\, dx' \right.$$

If the first term in the integral is integrated by parts once, a cancellation with the leading two terms in the entire expression is found yielding:

$$q = -3\bar{u}_e\, R_o \left[\int_o^x \frac{d\bar{r}_L}{dx'} (1 - 3\bar{r}_L^2)\, e^{-i\omega\tau_t(x')}\, dx' \right]$$

Integrating the second term by parts,

$$q = \frac{9\bar{u}_e\, k_1\, R_o}{i\omega} \left[\bar{r}_L\, e^{-i\omega\tau_t(x)} - 1 \right] - 3\bar{u}_e\, R_o \left(1 + \frac{3k_1}{i\omega} \right) \int_o^x \frac{d\bar{r}_L}{dx'}\, e^{-i\omega\tau_t(x')}\, dx'$$

where Eq (15) has been used. The integral appearing in the second term may
be put in the form of a Fresnel integral if Eq (15) is used; this integral is

$O[\bar{u}_e]$. Now, however, $9k_1$ can become $O[1]$ if k_1 is approxi-

mately 0.1. Then, since the second term appearing in the equation above is

$O[\bar{u}_e^2]$, it may be dropped and we have the burning rate expression

good to $O[\bar{u}_e]$ as:

$$q = \frac{9 \bar{u}_e k_1 R_o}{i \omega} \left[\bar{r}_L e^{-i\omega \tau_f(x)} - 1 \right] \tag{42}$$

or using Eq (41)

$$q = \frac{9 \bar{u}_e k_1 g}{i \omega \gamma} \left[1 - \bar{r}_L e^{-i\omega \tau_f(x)} \right] \psi_o e^{-i\omega \phi} \tag{43}$$

This may be compared to Crocco's form:

$$q = n \left(1 - e^{-i\omega \tau} \right) \int_o^X \varphi(x') \frac{d\bar{u}}{dx'} dx' \tag{44}$$

where n is the interaction index and τ is the sensitive time lag (which

is $O[1]$). Probably the most striking difference between Eqs (43) and (44) is

the appearance of a total time lag of $O[\frac{1}{\bar{u}_e}]$ in Eq. (43) versus a time delay

of $O[1]$ in Eq. (44). Another important difference is the appearance of two

frequency dependent parameters g and ϕ in Eq. (43) as opposed to n and

τ in Eq. (44) which must be frequency independent parameters since they are

steady-state quantities. However, since a further integration is to follow,

the total time lag in Eq (43) will disappear as of higher order which is con-

sistent with the formulation of Crocco and Cheng.

In order to see what Eq. (42) predicts we use it in the well

developed theory of Ref. (7). The solution appears there in the following form:

$$\frac{\gamma \mu_e}{\varphi_0} = -i \sin \omega - \gamma \bar{u}_e \cos \omega + (\gamma - 2) \omega B + \omega C \sin \omega + \frac{\gamma q^{(1)}}{\varphi_0} + E \tag{45}$$

$$\frac{\varphi_e}{\varphi_0} = \cos \omega + i \left[2 \bar{u}_e \sin \omega + A(\gamma - 2) \omega + C \omega \cos \omega - D \right] \tag{46}$$

where the subscript e denotes the entrance to the nozzle (x=1).

$$A = \int_0^1 \bar{u}(x') \cos \omega (1 - 2x') \, dx' \tag{47}$$

$$B = \int_0^1 \bar{u}(x') \sin \omega (1 - 2x') \, dx' \tag{48}$$

$$C = \int_0^1 \bar{u}(x') \, dx' \tag{49}$$

$$D = \frac{\gamma \omega}{\varphi_0} \int_0^1 q(x') \cos \omega (x' - 1) \, dx' \tag{50}$$

$$E = \frac{\gamma \omega}{\varphi_0} \int_0^1 q(x') \sin \omega (x' - 1) \, dx' \tag{51}$$

At the entrance to the nozzle we have an admittance relation of the form:

$$\frac{\gamma \mu_e}{\varphi_0} = -A = -(A_r + i A_i) \tag{52}$$

for isentropic oscillations. For simplicity we assume a very short nozzle so that the quasi-steady condition

$$A_i = 0 \quad , \quad A_r = \bar{u}_e \left(\frac{\gamma - 1}{2} \right) \tag{53}$$

is valid. Since combustion is assumed complete at x = 1,

$$q(1) = \frac{9 \bar{u}_e k_1 q \varphi_0}{i \omega \gamma} e^{-i \omega \phi} \tag{54}$$

If we make the approximation that combustion is concentrated at the injector end, this leads to difficulties in the choice of k_1 and the use of Eq (26).

However, if first a reasonable velocity distribution is chosen to yield a value of k_1, the integrals (50) and (51) are converted to velocity integrals through Eqs. (26) and (43), the velocity is replaced by a step function at, say, station ψ , and ψ is passed to zero, no difficulty arises. So, adopting this procedure and combining Eqs (43) and (45) - (54), we obtain as a solution for the characteristic values g and ϕ :

and

$$\phi = \frac{1}{\omega} \arctan\left\{\bar{u}_e\left[\left(\frac{\gamma+1}{2}\right)\cot\omega - \omega - \left(\frac{\gamma-1}{2}\right)\tan\omega\right]\right\} \tag{55}$$

$$g = \frac{\omega \sin\omega}{g\bar{u}_e k_1 \cos\omega\phi\left[\bar{u}_e\left(\frac{\gamma-1}{2}\right)\tan\omega\phi \sin\omega - \cos\omega\right]} \tag{56}$$

in which terms of $O[\bar{u}_e^2]$ have been neglected compared to terms of $O[1]$. Taking $\bar{u}_e = 0.05$ and a value of $k_1 = 0.2$ ft.$^{-1}$ x [*. Computations have been carried out and are presented in Figs (48) and (49). These are conditions that must hold at a stability limit. Assuming that a typical length between the point of injection and drop formation in an impinging jet injector is 1/2" and that a typical injection velocity is 100 ft/sec, a typical time that a fluid element could be sensitive to chamber conditions during injection is about 0.5 msecs. Therefore, since this is comparable to a high frequency oscillation period, only solutions for ϕ of $O[1]$ are considered.

Examination of these figures shows negative results. Three instability regions exist: 1) $g < 0$, $\phi > 0$ 2) $g > 0$, $\phi < 0$ and 3) $g > 0$, $\phi > 0$. By assumption and physical intuition we expect that only region (3) is of interest since positive g was expected and a positive phase lag was expected. However, region (3) has a lag greater than one-half cycle, which was not expected; this is also a lead of less than one-half cycle as in region (2). Fig. (49) shows ϕ decreasing with nondimensional

frequency. From experiments we know that higher ω is associated with the upper stability limit (in length) which is a lower physical frequency, ω^* . Physically, one would expect that ϕ^* would increase with ω^* and this is borne out in regions (1) and (3). It is also to be expected that g will decrease with increasing ω^* , or from Fig. (44), with increasing ϕ^* . Taking typical test results of:

$$L^*_{lower} = 0.08 \text{ ft.} \qquad \omega = 0.95$$

$$L^*_{upper} = 1.6 \text{ ft.} \qquad \omega = 1.05$$

we see that in region (3) $\phi^* \approx constant$ and g would be higher by a factor of two at the lower limit than at the upper limit, contrary to expectation. Poor behavior is also present in regions (1) and (2). Even in view of the above remarks the worst behavior has not been mentioned. That is, the values of g are $O[2-6]$ which is certainly a high number to be used in Eq (41) compared to a steady-state value less than one assumed by Penner (25). Furthermore, from Eq (56) $g \propto \frac{1}{k_1}$, where the value of $k_{1av.}$ chosen here is 0.2. But typical numbers from observed velocity distributions should be more in the neighborhood of 0.05 to 0.1 which would raise the required value of g to unreasonable figures.

The failure of this model should not, however, be regarded as a complete failure of the approach. For instance, it is noticed that the particular form of the vaporization law chosen allows a cancellation of two leading order terms in Eq. (22). This would not occur if, say, convective effects on droplet vaporization were taken into account explicitly in the perturbation procedure. Coupled with this observation is the fact that the model should probably be attempted with, say, three distinct size groups of droplets. Then the injector response characteristics may be modified to

include a shift in the distribution shape under oscillating conditions. This would not only prevent the term cancellation previously mentioned but would prevent a cancellation of leading order terms in the manipulation of Eq. (37). It is also probable that a better model should take into account the effects of two different propellants. However, with impinging jets of either the fuel-on-oxidizer doublet or the closely spaced like-on-like types there is obviously liquid phase mixing, and it is no longer a clear cut case of two distinct propellant types moving down the chamber. Furthermore, relation (41) is basically a conjecture since even steady-state behavior of injectors is not known with precision. It is possible that a different choice of the injector response function would have produced better results.

There are more fundamental objections to this model, however. First, the vaporization law used, while almost reasonable for steady-state description, is not correct when perturbed. Furthermore, it is not correct to perturb steady-state heat transfer correlations if convective effects on droplet vaporization are introduced. One must remember that even if a droplet is at a wet bulb temperature which is constant in time, one is perturbing conditions that exist _outside_ of a region of heat and mass diffusion surrounding a droplet. The correct, or more correct, form that vaporization perturbations should take can only be obtained if one considers the full system of equations describing the diffusion field. Secondly, the heating-up portion of a droplet lifetime can be significant compared to its total lifetime in the chamber. During such a period the D^2 law of vaporization is certainly not valid. Also, chemical kinetics may be important in this region since we expect a lower gas temperature near the injector face. Third, even after the heating-up period is over, the steady-state solution may not be expected to follow Eq. (15) since it is still a quasi-steady state solu-

tion of the diffusion field. This problem is discussed elsewhere in this report in Appendix F. Finally, one of the most serious objections, which has apparently not been recognized by other workers in the field, is that the required time delay from Crocco's work will never be introduced by pure perturbations on existing equations for a two-component chamber model unless it is independently introduced (as in the work of Crocco and Cheng). The reason for this is that the conception of a system of equations describing only liquid motion and the motion of chamber gases of complete combustion leaves something out. That is, it does not account for that portion of time during which an element of propellant is in the transition stage from liquid to chamber gas through the diffusion, mixing, and reaction processes.

In summary, it may be said that there is still a great lack of information concerning the basic processes taking place within the rocket combustor to the extent that a reasonable description of the unsteady chamber is still forthcoming. While it appears that injector interaction concerning drop size behavior is not strong enough to contribute to the instability problem, this conclusion is not absolutely certain. The conclusion that vaporization rate perturbations cannot contribute is erroneous because the equations used to describe the problem are incomplete. However, work on the above problems is now in progress at Princeton and will be reported in a future publication.

APPENDIX F

The Significance of the Quasi-Steady-State
Assumption in Droplet Vaporization Theory

There are many problems which arise in engineering that require

the solution of what is basically the diffusion equation with boundary

conditions to be applied at positions which are nonstationary. Such

problems include the freezing or melting of water on a lake, the solidi-

fication or melting of metals, and the vaporization or condensation of

a liquid surface. Very often in theoretical consideration of such

problems the assumption is made that at any instant of time the process

takes place according to the steady-state process. That is, the boundary

is assumed stationary in time and the time derivative(s) in the diffusion

equation(s) describing the system are set to zero. The reasons for doing

so are two-fold. First, the results of such an idealization yield results

not far from physical reality in many cases, and secondly, the mathe-

matical difficulties introduced by consideration of the full problem

preclude an exact solution for a great number of problems.

The primary case of interest here is the evaporation of a

droplet in a high temperature environment such as may be found in a rocket

engine. There is, as yet, no exact solution of the system of equations

describing the process and the common approach is to use the quasi-

steady-state assumption. The usual justification is that one considers

the ratio of a typical time of physical interest, say the droplet life-

time, to a typical diffusion time of the problem, say the square of a

characteristic length in the problem divided by the thermal diffusivity.

If this ratio is large, one assumes the validity of the quasi-steady

assumption. The question arises, however, as to the meaning of "large."

In the absence of an exact solution to the problem there is as yet no

method to estimate the error made in assuming a quasi-steady-state
solution valid.

The conservation equations for this problem will be written
under the following initial assumptions:

1. The diffusion field may be characterized by a droplet vapor
and a single, fictitious inert gas as the only constituents.

2. There are no mass sources.

3. Changes in kinetic energy and potential energy are
negligible compared to thermal energy changes.

4. The gas mixture is inviscid.

5. There is mass diffusion by a concentration gradient only.

6. There is heat transfer by conduction only.

Following Penner (26) the overall continuity, species continuity and energy
equations for a continuum are:

$$\frac{\partial \rho^*}{\partial t^*} + \nabla \cdot (\rho^* \vec{V}^*) = \frac{D\rho^*}{Dt^*} + \rho^* \nabla \cdot \vec{V}^* = 0 \tag{1}$$

$$\frac{D(\ln Y_K)}{Dt^*} + \frac{1}{\rho^* Y_K} \nabla \cdot (\rho^* Y_K \vec{V}_K^*) = 0 \tag{2}$$

$$\frac{D(\rho^* e^*)}{Dt^*} + \rho^* e^* \nabla \cdot \vec{v}^* = \nabla \cdot \vec{Q}^* - \nabla \cdot (p^* \vec{v}^*) \tag{3}$$

where use has been made of assumptions (1-4). A star superscript denotes
a dimensional quantity and an arrow superscript indicates a vector
quantity. Density is ρ, t is time, v is mass weighted average
velocity, e is internal energy per unit mass, and p is pressure.
Y_k is the mass fraction of species K and V_k is the diffusion
velocity of species K given by

$$\vec{V}_K^* = - D_{12}^* \nabla (\ln Y_K) \tag{4}$$

where D_{12} is the binary diffusion coefficient and use has been made

of assumption (5).   Q is the heat flux given by:

$$\vec{Q}^* = \lambda^* \nabla T^* - \varsigma^* \sum_{K=1}^{2} Y_K h_K^* \vec{V}_K^* \tag{5}$$

where λ is the thermal conductivity, T the temperature, h the

enthalpy per unit mass and use has been made of assumption (6). The

actual velocity of species K is given by:

$$\vec{V}_K^* = \vec{\upsilon}^* + \vec{V}_K^* \tag{6}$$

Using Equation (I) and the definition of enthalpy the energy equation

may be rewritten as:

$$\frac{Dh^*}{Dt^*} = \frac{1}{\varsigma^*} \nabla \cdot \vec{Q}^* + \frac{1}{\varsigma^*} \frac{\partial p^*}{\partial t^*} \tag{7}$$

It is now convenient to specialize to a spherically symmetric system

although this introduces an approximation which is difficult to achieve

in practice. We have from Equations (I), (2), (4), (5) and (7):

$$\frac{\partial \varsigma^*}{\partial t^*} + \frac{1}{r^{*2}} \frac{\partial}{\partial r^*}\left(\varsigma^* r^{*2} \upsilon^*\right) = \frac{D\varsigma^*}{Dt^*} + \frac{\varsigma^*}{r^{*2}} \frac{\partial (r^{*2}\upsilon^*)}{\partial r^*} = 0 \tag{8}$$

$$\frac{\partial Y_K}{\partial t^*} + \upsilon^* \frac{\partial Y_K}{\partial r^*} - \frac{1}{\varsigma^* r^{*2}} \frac{\partial}{\partial r^*}\left(\varsigma^* r^{*2} D_{12} \frac{\partial Y_K}{\partial r^*}\right) =$$

$$\frac{\partial Y_K}{\partial t^*} + \upsilon^* \frac{\partial Y_K}{\partial r^*} + \frac{1}{\varsigma^* r^{*2}} \frac{\partial}{\partial r^*}\left(\varsigma^* r^{*2} Y_K V_K^*\right) = 0 \tag{9}$$

$$\frac{\partial h^*}{\partial t^*} + \upsilon^* \frac{\partial h^*}{\partial r^*} = \frac{1}{\varsigma^* r^{*2}} \frac{\partial}{\partial r^*}\left[r^{*2}\lambda^* \frac{\partial T^*}{\partial r^*} - \varsigma^* r^{*2} \sum_{K=1}^{2} Y_K h_K^* V_K^*\right]$$

$$+ \frac{1}{\varsigma^*} \frac{\partial p^*}{\partial t^*} \tag{10}$$

Since $h^* = \sum_{K=1}^{2} Y_K h_K^*$ we may multiply Equation (9) by h_K, sum over

K and subtract from Equation (10) to obtain:

$$\sum_{K=1}^{2} Y_K \frac{\partial h_K^*}{\partial t^*} + \sum_{K=1}^{2} Y_K (v^* + V_K^*) \frac{\partial h_K^*}{\partial r^*} = \frac{1}{\rho^* r^{*2}} \frac{\partial}{\partial r^*} \left(r^{*2} \lambda^* \frac{\partial T^*}{\partial r^*} \right) + \frac{1}{\rho^*} \frac{\partial p^*}{\partial t^*} \quad (11)$$

It is in this form that one sees the utility of the quasi-steady-state assumption. For then $\frac{\partial}{\partial t} = 0$ and the overall velocity of the inert gas, say, v_2^* is zero. By Equation (6), Equation (11) becomes:

$$\rho^* r^{*2} Y_1 v_1^* \frac{\partial h_1^*}{\partial r^*} = \frac{\partial}{\partial r^*} \left(r^{*2} \lambda^* \frac{\partial T^*}{\partial r^*} \right) \quad (12)$$

But $\rho^* r^{*2} Y_1 v_1^*$ is the droplet vapor mass transfer which by equation (8) is constant, and the character of the simplification is evident.

To make equations (8), (9) and (11) amenable to analytical treatment it is necessary to introduce some further simplifying assumptions. We accept the perfect gas equation of state and assume constant specific heats. Further, the specific heats for both species are considered the same which requires equal molecular weights. The thermal conductivity will be assumed to be constant at an average value through the diffusion film. From elementary kinetic theory a consistent assumption is that $\rho^* D_{12}^*$ is also constant at some average film value. Then the system of equations becomes:

$$\frac{\partial \rho^*}{\partial t^*} + \frac{1}{r^{*2}} \frac{\partial}{\partial r^*} \left(r^{*2} \rho^* v^* \right) = 0 \quad (13)$$

$$\frac{\partial Y_K}{\partial t^*} + v^* \frac{\partial Y_K}{\partial r^*} = \frac{\overline{\rho^* D_{12}^*}}{\rho^* r^{*2}} \frac{\partial}{\partial r^*} \left(r^{*2} \cdot \frac{\partial Y_K}{\partial r^*} \right) \quad (14)$$

$$\frac{\partial T^*}{\partial t^*} + v^* \frac{\partial T^*}{\partial r^*} + \frac{\partial T^*}{\partial r^*} \sum_{K=1}^{2} Y_K V_K^* = \frac{\overline{\lambda^*}}{\overline{c_p^*} \rho^* r^{*2}} \frac{\partial}{\partial r^*} \left(r^{*2} \frac{\partial T^*}{\partial r^*} \right) + \frac{1}{\rho^*} \frac{\partial p^*}{\partial t^*} \quad (15)$$

But $\sum_{K=1}^{2} Y_K V_K^* = 0$ from equation (6) and the definition of v^*.

Therefore, equation (15) becomes:

$$\frac{\partial T^*}{\partial t^*} + v^* \frac{\partial T^*}{\partial r^*} = \frac{\lambda^*}{c_p^* \varsigma^* r^{*2}} \frac{\partial}{\partial r^*}\left(r^{*2} \frac{\partial T^*}{\partial r^*}\right) + \frac{1}{\varsigma^*} \frac{\partial p^*}{\partial t^*} \qquad (16)$$

From the momentum equation, assumption (3) and consideration of a steady-state pressure field, we may replace the meomentum equation by:

$$p^* = \text{constant} \neq p(r,t) \qquad (17)$$

Finally, the state equation is:

$$p^* = R^* \varsigma^* T^* \qquad (18)$$

where R^* is the universal gas constant divided by the molecular weight.

It is convenient to define non-dimensional variables as follows:

$$\varsigma = \frac{\varsigma^*}{\varsigma_c^*} \qquad t = \frac{t^*}{t_f^*} \qquad r = \frac{r^*}{r_{L_o}^*}$$

$$m = \frac{\varsigma^* v^* r^{*2} \bar{c}_p^*}{\bar{\lambda}^* r_{L_o}^*} \qquad X = \frac{v^* r_{L_o}^* \varsigma_c^* \bar{c}_p^*}{\bar{\lambda}^*} \qquad Le = \frac{\bar{\lambda}^*}{\bar{c}_p^* \varsigma^* D_{12}^*} \qquad (19)$$

$$K = \frac{\bar{\lambda}^* t_f^*}{\varsigma_c^* \bar{c}_p^* r_{L_o}^{*2}} \qquad T = \frac{T^*}{T_c^*} \qquad P = \frac{p^*}{p_c^*} = 1$$

The reference fluid properties ς_c, T_c and P_c are conditions existing at some radius r_c which is defined as the outside boundary of the diffusion film. The reference time t_f is still to be defined. r_{L_o} is the initial droplet radius, m is a non-dimensional mass flow rate (m = $\varsigma r^2 X$) and L_e is the Lewis number. Equations (13), (14), (16), (17) and (18) may be written:

$$\frac{1}{K} \frac{\partial \varsigma}{\partial t} + \frac{1}{r^2} \frac{\partial m}{\partial r} = 0 \qquad (20)$$

$$\frac{1}{K} \frac{\partial Y_n}{\partial t} + X \frac{\partial Y_n}{\partial r} = \frac{1}{Le \, \varsigma r^2} \frac{\partial}{\partial r}\left(r^2 \frac{\partial Y_n}{\partial r}\right) \qquad (21)$$

$$\frac{1}{\kappa} \frac{\partial T}{\partial t} + x \frac{\partial T}{\partial r} = \frac{1}{\rho r^2} \frac{\partial}{\partial r} \left(r^2 \frac{\partial T}{\partial r} \right) \tag{22}$$

$$P = 1 \tag{23}$$

$$\rho T = 1 \tag{24}$$

This is a non-linear set of equations of the parabolic type to which must be attached an appropriate set of initial and boundary conditions. One condition that should be imposed is a relation between the mass fraction of droplet vapor and temperature at the droplet surface. An equilibrium condition of the form

$$T[r_L(t), t] = T[Y_R] \tag{25}$$

is chosen where r_L is the interface position which may be a function of time. There is confusion in the literature concerning this boundary condition so some time will be spent on it. It is required that equation (25) represent a saturation state. Therefore, on a temperature entropy diagram of the droplet substance, for example, the state of the droplet vapor must lie on the saturation line if the constant
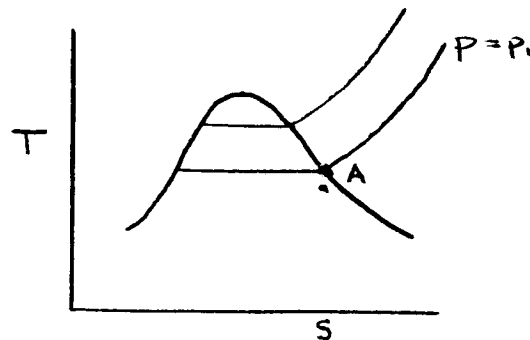
pressure lines are interpreted as partial pressures of the droplet vapor. For instance, point A in the diagram above is a permissible state if p_1

is the partial pressure of the droplet vapor at the droplet surface.
This will neglect effects of surface tension which becomes important
only when the droplet radius becomes comparable with the gaseous mean
free path. It will be further assumed here that the droplet is at a
"wet bulb" temperature where the term is used in the same sense as in
psychrometric work. That is, there will be assumed to exist a temperature
where the heat transfer to the droplet goes completely toward vaporization.
Such a condition is not a true equilibrium state since heat and mass
transfer are taking place, but in the case of high temperature vapori-
zation one cannot speak of the equivalence of the wet bulb and the
adiabatic saturation temperature so often used in psychrometric work.
In fact, such an equivalence is merely a coincidence for water-air mixtures
at ordinary temperatures and pressures. An adiabatic saturation state
would require that the liquid and surroundings be at the same temperature
and that no heat or mass transfer take place. Such a condition is
impossible because attempts to raise the droplet temperature to the
ambient temperature causes mass transfer which tends to cool the droplet.
We, of course, assume that the surroundings may be maintained at any
desired temperature.

In the time dependent problem a wet bulb temperature
which is constant in time can only be realized if the Lewis number is
equal to one; for if Le $\neq$ 1 the often quoted similarity between
heat and mass transfer does not exist. However, for high temperature
surroundings the droplet remains at a much lower temperature than the
surroundings (at least for volatile liquids such as hydrocarbons) and
variations in time around a mean wet bulb temperature may be considered

slight. Under this assumption equation (25) becomes:

$$T[r_L(t), t] = \tau \tag{26}$$

where τ is a constant which may be precalculated. This introduces the further simplification that, as far as the problem of the vaporization rate is concerned, consideration of the mass transfer equation (21), may be dropped. Its sole usefulness is in pointing out that the Lewis number must be considered in the calculation of τ . These remarks have eliminated one type of unsteady behavior which may enter the problem; i.e., the heating up period of the droplet to wet bulb.

A second boundary condition to be applied is:

$$T[r_c(t), t] \tag{27}$$

where r_c is the position, which may be a function of time, where the reference quantities are chosen. In quasi-steady theory this position is specified by a convective heat transfer relation or in the case of a burning droplet by a burning relation. For pure quiescent evaporation r_c is cast to infinity. An initial condition should also be imposed so that:

$$T[r, 0] = T_0(r) \tag{28}$$

Finally, a condition to find the interface position must be introduced in the form of a heat transfer condition:

$$\left.\frac{\partial T}{\partial r}\right)_{r_L(t)} = \frac{m_{r_L(t)}}{r_L^2 B_s} = -\frac{1}{\kappa_1 B_s} \frac{dr_L}{dt} \tag{29}$$

where it has been assumed $\rho_L^* / \rho_G^* \gg 1$

Also:

$$B_s = \frac{\overline{C_p}^* T_e^*}{\Delta l^*} \qquad K_l = \frac{\overline{\lambda}^* t_f^*}{\rho_L^* \overline{C_p}^* r_{L_0}^{*2}} \qquad (30)$$

and Δl and ρ_L are the liquid latent heat of vaporization and density,
respectively. Since a total derivative at a constant temperature surface
appears in equation (29), this is a non-linear condition. It is assumed
that equations (20), (22)-(24) and (26)-(29) constitute a well-posed
problem.

What is in essence usually done to this set of equations is
to consider all derivatives of order unity and consider K large. This
assumes the ratio of a typical time in the problem, say, the droplet
lifetime, to a typical diffusion time is very large. Then one drops
all the terms containing time derivatives. Thus, from equation (20)
m is constant in r and equation (22) becomes an ordinary differential
equation for T which may be integrated subject to equations (26) and
(27). Equation (29) may be used to find the interface position as a
function of time. Another approach is to consider slow evaporation
so that the convective term in equation (22) disappears. Then we have
essentially the heat equation, but with a variable density which cannot
be assumed constant unless equation (24) is abandoned. If the time
derivative is also dropped here, essentially Laplace's equation remains
and may be immediately integrated as before.

As pointed out by several investigators (27,28) there are
several things wrong with this approach. First, the problem is solved
without reference to initial conditions and the solution is able to
satisfy only the steady state conditions. Also, the mathematical
procedure of introducing the time dependence as only a parameter in the
solution is open to question. Secondly, if the heat equation without

the convective term is adopted, account is not given to important density

variation and convective effects that occur in high temperature work.

Finally, if Laplace's equation is adopted for the problem description and

r_c cast to infinity, the droplet vapor content of the surroundings

decreases from an infinite to a smaller infinite value as the droplet

vaporizes.

Concerning the work which has been done on this and other related

problems, Fuchs (27) obtained typical correction factors to describe the

relaxation of the initial condition to the quasi-steady condition and the

error made in the droplet lifetime due to the time dependence introduced by

the contracting radius. This was, however, carried out for the heat

equation and by approximate methods. Also, only one type of initial

condition was considered, $T_o = 1$.

An exact solution for the heat equation under very general

conditions of moving boundaries has been obtained by Kolodner (29). The

solution is in the form of a non-linear integro-differential equation for

the interface position, if this is any simplification. The solution is

based on the existence of the fundamental solution to the heat equation

and uniqueness of the solution has been shown. In certain cases this

work lends uniqueness to a great many other solutions as appear, for

example, in Carslaw and Jaeger's work (30). For instance, in Neumann's

problem of linear flow we have for $x > 0$ a liquid initially at

temperature T_1 and a solid initially at $x \leq 0$ which freezes into the

liquid, the interface position given by X . Stating a condition that

$T^*(0) = 0$ for all time, a solution may be found where the interface

position is given as $X/t^{\frac{1}{2}}$ = constant. Uniqueness for the problem is

shown by Kolodoner's work. This is a similar type solution and may be

applied to many other problems with and without the convective term. Kirkaldy (28) has obtained an exact solution to the spherical problem with the convective term included but under the assumption that ρ is constant. It is found that if $r_L/t^{\frac{1}{2}}$ is constant the equation will reduce to an ordinary differential equation in the independent variable $\eta = r/t^{\frac{1}{2}}$. The objection here is that this procedure will not work for evaporation, but only condensation, because of the finiteness of r_L at $t = 0$. Also, density being constant is an intolerable assumption in the present work; furthermore, these similar type solutions are only able to satisfy very specialized initial conditions.

There is one other interesting result obtained from these exact solutions. In a great many cases an expansion of the solution in a series will yield the quasi-steady solution as a leading term with the remaining terms important only near $t = 0$. Also, the interface motion is many times well approximated (sometimes exactly) by the quasi-steady solution. However, in the absence of an exact solution to the problem of interest, it still remains to investigate the error introduced by the quasi-steady theory.

An exact solution of the system of equations in series form is first attempted. First, from equation (22), using equations (20) and (24):

$$\frac{\partial}{\partial r}\left[r^2 \frac{\partial T}{\partial r} - mT\right] = 0 \tag{31}$$

This is immediately integrable over r ; applying equation (29):

$$r^2 \frac{\partial T}{\partial r} - mT = m_L(t)\left(\frac{1}{B_s} - \tau\right) \tag{32}$$

where m_L (t) is the mass flow rate at the liquid surface which is, of

course, a function of time. Dividing equation (32) through by t, differentiating with respect to r and using equation (20) there follows:

$$\left(T_{rr} + \frac{2 T_r}{r}\right) T - (T_r)^2 - \frac{T_t}{K} + \frac{2 m_L \epsilon}{r^2} T_r = 0 \qquad (33)$$

where ϵ is defined as $\frac{1}{2}(1/B_s - \tau)$. Equation (33) is a non-linear parabolic equation in temperature alone and is to be solved under conditions (26)-(29). In these relations we note the appearance of four fundamental parameters K, ϵ, τ, and K_1, where B_s may be derived from ϵ and τ. Another useful parameter which may be derived from these four is the Spalding transfer number:

$$B = \frac{\bar{c}_p^+ (T_c^* - T_L^*)}{\Delta \ell^*} = B_s(1 - \tau) = \frac{1 - \tau}{\tau + 2\epsilon}$$

In a great many problems of interest $1/K \ll 1$ and $\epsilon \ll 1$. Therefore a Taylor series expansion of the solution in these two parameters is assumed valid.

$$T(r, t) = T_{(0,0)} + \epsilon T_{(0,1)} + \cdots + \frac{1}{K}\left[T_{(1,0)} + \epsilon T_{(1,1)} + \cdots\right] + \cdots$$

or

$$T(r, t) = \sum_{i=0}^{\infty} \sum_{j=0}^{\infty} \left(\frac{1}{K}\right)^i \epsilon^j T_{(i,j)} \qquad (34)$$

Similarly:

$$r_L(t) = \sum_{i=0}^{\infty} \sum_{j=0}^{\infty} \left(\frac{1}{K}\right)^i \epsilon^j r_{L(i,j)} \qquad (35)$$

It will also be convenient to write equation (34) as:

$$T(r, t) = \sum_{i=0}^{\infty} \left(\frac{1}{K}\right)^i T^{(i)} \qquad (36)$$

where

$$T^{(i)} = \sum_{j=0}^{\infty} \epsilon^j \, T_{(i,j)} \tag{37}$$

Similar manipulations hold for the other quantities of interest, m and r .

Equation (36) is most conveniently substituted first in equation (33). Collecting terms in like powers of 1/K there is obtained for the first two orders in 1/K .

$$\left(\frac{1}{K}\right)^0 \quad T^{(0)} T_{rr}^{(0)} + \frac{2 T^{(0)} T_r^{(0)}}{r} - \left(T_r^{(0)}\right)^2 + 2 \epsilon \, m_L^{(0)} \, T_r^{(0)} = 0 \tag{38}$$

$$\left(\frac{1}{K}\right)^1 \quad T_{rr}^{(1)} + 2 T_r^{(1)} \left[\frac{1}{r} - \frac{T_r^{(0)}}{T^{(0)}} + \frac{\epsilon \, m_L^{(0)}}{r^2 T^{(0)}}\right] + T^{(1)} \left[\frac{T_{rr}^{(0)}}{T^{(0)}} + \frac{2}{r} \frac{T_r^{(0)}}{T^{(0)}}\right] = \tag{39}$$

$$= \frac{T_t^{(0)}}{T^{(0)}} - \frac{2 \epsilon \, m_L^{(1)} \, T_r^{(0)}}{r^2 T^{(0)}}$$

where m_L has been expanded as in equation (36). Expanding the boundary conditions, equations (26)-(29): .

$$\left(\frac{1}{K}\right)^0 \quad T^{(0)}\left[r_L^{(0)}(t), t\right] = 2 \tag{40}$$

$$T^{(0)}\left[r_c^{(0)}(t), t\right] = 1 \tag{41}$$

$$T^{(0)}(r, 0) = T_0(r) \tag{42}$$

$$T_r^{(0)}\left[r_L^{(0)}(t), t\right] = \frac{m_L^{(0)}}{B_s \, r_L^{(0)^2}} = -\frac{1}{K_1 B_s} \frac{d r_L^{(0)}}{dt} \tag{43}$$

$$\left(\frac{1}{K}\right)^1 \quad T^{(1)}\left[r_L^{(0)}(t), t\right] + T_r^{(0)}\left[r_L^{(0)}(t), t\right] r_L^{(1)} = 0 \tag{44}$$

$$T^{(1)}\left[r_c^{(0)}(t), t\right] + T_r^{(0)}\left[r_c^{(0)}(t), t\right] r_c^{(1)} = 0 \tag{45}$$

$$T^{(1)}(r, 0) = 0 \tag{46}$$

$$T_r^{(1)}\left[r_L^{(0)}(t), t\right] + T_{rr}^{(0)}\left[r_L^{(0)}(t), t\right] r_L^{(1)} = \tag{47}$$

$$-\frac{1}{B_3 \, r_L^{(0)2}}\left[\frac{2 \, m_L^{(0)} \, r_L^{(1)}}{r_L^{(0)}} - m_L^{(1)}\right] = -\frac{1}{K_1 B_3}\frac{d \, r_L^{(1)}}{d t}$$

Immediately there are two important observations. First, the reason for not going to the double expansion immediately is that equation (38) is solvable as it stands. Since equation (39) is not, the double expansion will be employed for it. While it would be more rigorous to carry out the complete expansion and to arrive at the result that the solution to the zeroth order in 1/K may be expressed as a summed series in ϵ, it will be stated without proof that a terminating polynomial in ϵ results for the solution of $T^{(0)}$. In fact, the solution is linear in ϵ. The second and most important observation is that the initial conditions, equations (28), (42) or (46), can never be satisfied with this scheme since, as in the quasi-steady solution, the time derivative of the order of the solution being considered never appears in the equation. This could have been seen at the outset and is analogous to problems that arise in, say, ordinary differential equations when a regular expansion in terms of a small parameter appearing in front of the highest derivative is attempted. The usual procedure in such a case is to find a transformation of variable to place this aparameter in front of a term that can afford to be lost while still satisfying the boundary conditions in each order equation. While this procedure could have been adopted here, no transformation yielding equations amenable to exact analysis has been found. Now, although the idea of an exact solution

has been abandoned, this solution should yield information concerning one of the remaining two types of unsteadiness which enters the problem. Assuming that the initial conditions which will be demanded by this solution can be provided, information should be gained concerning the unsteady effects introduced by the contracting droplet radius. In particular, under the imposed conditions a correction to the quasi-steady vaporization rate should be obtained.

Proceeding on this basis equation (38) is merely the quasi-steady equation in a different form than usually stated, it may be integrated using equations (40) and (43) to yield:

$$T^{(o)} = T_{(o,o)} + \epsilon T_{(o,1)} = \frac{1}{B_s} e^{m_L^{(o)}\left(\frac{1}{r_L^{(o)}} - \frac{1}{r}\right)} - 2\epsilon \qquad (48)$$

Also, using equations (41) and (43) the familiar D^2 law may be obtained:

$$r_L^{(o)2} = 1 - \frac{2 K_1 \ln(1+B)}{C} t \qquad (49)$$

where

$$C = 1 - \frac{r_L^{(o)}}{r_c^{(o)}}$$

It is now convenient to define the reference time, t_f^* in equation (19) to be the quasi-steady droplet lifetime. Then $t = 1$ when $r_L(0) = 0$ which, for a given set of numbers B, ρ_L^*/ρ_c^*, and C defines K for the problem because

$$\frac{2 K \ln(1+B)}{\rho_L^*/\rho_c^* \ C} = 1$$

Three convenient quantities are computed from equation (48).

$$T_r^{(o)} = \frac{m_L^{(o)} T_{(o,o)}}{r^2} \qquad (50)$$

$$T_{rr}^{(0)} = \frac{m_L^{(0)} T_{(0,0)} (m_L^{(0)} - 2r)}{r^4} \tag{51}$$

$$T_t^{(0)} = \frac{m_L^{(0)} T_{(0,0)}}{2r \, r_L^{(0)2}} \tag{52}$$

Expanding equation (39) by equation (37) and using equations (50)-(52),

$$\epsilon^0 \quad T_{(1,0)\,rr} + T_{(1,0)\,r}\left[\frac{2}{r} - \frac{2m_L^{(0)}}{r^2}\right] + T_{(1,0)} \frac{m_L^{(0)2}}{r^4} = \frac{m_L^{(0)}}{2r \, r_L^{(0)2}} \tag{53}$$

$$\epsilon^1 \quad T_{(1,1)\,rr} + T_{(1,1)\,r}\left[\frac{2}{r} - \frac{2m_L^{(0)}}{r^2}\right] + T_{(1,1)} \frac{m_L^{(0)2}}{r^4} = \tag{54}$$

$$= 2\frac{T_{(1,0)}}{T_{(0,0)}}rr - \frac{T_{(1,0)}}{T_{(0,0)}}r\left[\frac{2m_L^{(0)}}{r^2} - \frac{4}{r}\right] - \frac{2m_{L(1,0)}m_L^{(0)}}{r^4}$$

Because of the linearity of equation (39) the left hand side of succeeding

order equationswill always be as in equations (53) and (54), but the

inhomogeneous terms will be different. Only the solution for equation (53)

will be carried out. It is to be solved under the following boundary

conditions:

$$T_{(1,0)}\left[r_L^{(0)}(t), t\right] + T_{(0,0)\,r}\left[r_L^{(0)}(t), t\right] r_{L(1,0)} = 0 \tag{55}$$

$$T_{(1,0)}\left[r_L^{(0)}(t), t\right] + T_{(0,0)\,r}\left[r_L^{(0)}(t), t\right] r_{L(1,0)} = 0 \tag{56}$$

Also,

$$\frac{dr_{L(1,0)}}{dt} = -K_1 B_s\left[T_{(1,0)\,r}(r_L^{(0)}, t) + T_{(0,0)\,rr}(r_L^{(0)}, t) \, r_{L(1,0)}\right] \tag{57}$$

Equation (54) is linear, but with non-constant coefficients and an

irregular singular point at $r = 0$. This point is excluded during all

except the final instant of the vaporization period. The transformation

to normal form by letting

$$T_{(1,0)} = g\sigma \quad , \quad g'/g = \frac{m_L^{(0)}}{r^2} - \frac{1}{r}$$

yields:

$$T_{(1,0)} = \frac{e^{-m_L^{(0)}/r}}{r}\left[\frac{m_L^{(0)}}{2\,r_L^{(0)2}}\int^r dr'\int^{r'} e^{m_L^{(0)}/r''}dr'' + ar + b\right] \tag{58}$$

where a and b are constants. In the evaluation of the constants it is desirable to make a further assumption which is in accord with some observations for burning droplets; i.e.,

$$r_L^{(t)}/r_c^{(t)} = \text{constant}$$

This leads to the result:

$$\frac{r_L^{(0)}}{r_c^{(0)}} = \frac{r_{L(1,0)}}{r_{c(1,0)}} = \frac{r_{c(1,1)}}{r_{c(1,1)}} = \cdots = 1-C \tag{59}$$

Using equations (55), (56), (58) and (59) the solution for $T_{(1,0)}$ is:

$$T_{(1,0)} = \frac{e^{-m_L^{(0)}/r}\,\ell n(1+B)}{2\,r\,r_L^{(0)}\,C}\int_{r_L^{(0)}}^r dr'\int_1^{r'} e^{m_L^{(0)}/r''}dr'' -$$

$$- \frac{e^{-m_L^{(0)}\left(\frac{1}{r}-\frac{1}{r_L^{(0)}}\right)}}{r}\frac{\ell n(1+B)}{C\,B_s}\,r_{L(1,0)} + \tag{60}$$

$$+ e^{-m_L^{(0)}/r}\left(1-\frac{r_L^{(0)}}{r}\right)\left(\frac{C-1}{C^2}\right)\frac{\ell n(1+B)}{r_L^{(0)}}\left\{\frac{e^{m_L^{(0)}/r_L^{(0)}}}{B_s}\left[\,2-C\,\right]r_{L(1,0)} + \right.$$

$$\left. + \frac{1}{2\,r_L^{(0)}}\int_{r_L^{(0)}}^{r_c^{(0)}} dr'\int_1^{r'} e^{-m_L^{(0)}/r''}dr''\right\}$$

This still requires a solution of equation (57) for $r_{L(1,0)}$. Aside from the singularity at $r = 0$ there is an interesting singularity at $r_L^{(0)} = 0$. That is, unless $r_{L(1,0)} < 0$ so that the droplet vaporizes

faster than at the quasi-steady rate $r_L^{(o)}$ will become zero before the droplet is completely vaporized and the expansion will blow up.

The approximation is now made that $r_L/r_c \ll 1$ so that the last two terms in equation (60) are negligible compared to the first two. It will be stated without demonstration that this will only yield quantitative errors in the final result; qualitatively the solution will remain the same. Performing the necessary differentiation and evaluation at $r_L^{(o)}$ of equation (60) and using equations (49) and (50), equation (57) becomes:

$$\frac{d\, r_{L(1,0)}}{dt} - \frac{1}{2} \frac{r_{L(1,0)}}{1-t} = - \frac{B_3 \ln(1+B)}{4(1-t)} \int_1^{r_L^{(o)}} e^{m_L^{(o)}/r'} dr' \qquad (61)$$

which is to be solved under the condition:

$$r_{L(1,0)}(o) = 0 \qquad (62)$$

The solution is
$$r_{L(1,0)} = - \frac{B_3}{4(1-t)^{1/2}(1+B)} \int_0^t (1-t')^{-1/2} dt' \int_1^{r_L^{(o)}} e^{m_L^{(o)}/r'} dr' \qquad (63)$$

As suspected this solution blows up if $t = 1$; however, $r_{L(1,0)} < 0$ by inspection and the droplet disappears before $t = 1$. It is to be further noted that away from $r = 0$ all correction terms are of $O(1)$ and the expansion appears regular at least as far as carried. Discussion of this result is deferred until later.

Since the above analysis gives no information concerning the relaxation of the initial condition, this problem must be treated separately. Consideration will be given to a porous sphere, continually wetted with liquid at the wet bulb temperature of a surrounding high temperature gas into which the sphere is suddenly thrust. Thus, the initial conditions are presumed known and the droplet radius remains constant in time $(r_L = 1)$. It is convenient to adopt $y = (T^* - T_L^*)/(T_c^* - T_L^*)$

as the independent variable. Then the energy equation, the boundary conditions, and the initial condition become

$$\frac{\partial y}{\partial \tau} = -x\frac{\partial y}{\partial r} + \frac{1}{\beta r^2}\frac{\partial}{\partial r}\left(r^2\frac{\partial y}{\partial r}\right) \tag{64}$$

$$y(1,t) = 0 \qquad y(r_c,t) = 1 \tag{65}$$

$$y(r,0) = a(r) \tag{66}$$

where t has been contracted by:

$$\tau = \kappa t \tag{67}$$

It is desirable to convert equation (64) into a linear form so that the powerful methods of linear mathematics may be used. The assumption will be made that the density is not a function of time, but remains the function of distance as specified by the initial conditions. This will clearly abandon the state equation, but through equation (20) this requires that $x(r)$ is not a function of time. It is still hoped that the behavior of the relaxation of the initial condition to the steady state condition is not seriously affected by this simplification, at least for initial conditions which do not radically depart from the steady-state condition.

Under this idealization it is possible to adapt a method developed by Frisch (31) to obtain a useful result. Equation (64) may be written:

$$\frac{\partial y}{\partial \tau} = \mathcal{L}_r[y(r,t)] \tag{68}$$

where α_r is a linear operator in r defined by:

$$\alpha_r = \frac{1}{\rho \, r \cdot e^{m/r}} \frac{\partial}{\partial r} \left[r^2 e^{m/r} \frac{\partial}{\partial r} \right] \tag{69}$$

Define a steady-state solution given by

$$\alpha_r \left[y^{(s)}(r) \right] = 0 \tag{70}$$

under the boundary conditions

$$y^{(s)}(1) = 0 \qquad y^{(s)}(r_c) = 1 \tag{71}$$

Define a relaxation time lag:

$$T(r) = - \frac{\int_0^\infty Q_r \left[y - y^{(s)} \right] dt}{Q_r \left[y^{(s)} \right]} \tag{72}$$

where $\,_r$ is some other linear operator. If $\,_r \equiv 1, T(r)$ describes a typical relaxation time that the temperature takes to come to steady state. The interest here primarily concerns heat transfer so that from here on $\,_r = \frac{\partial}{\partial r}$ will be considered.

Let

$$u(r,t) = y(r,t) - y^{(s)}(r)$$

so that

$$\frac{\partial y}{\partial t} = \alpha_r \left[u(r,t) \right] \tag{73}$$

is subject to

$$u(1,t) = u(r_c, t) = 0 \tag{74}$$

Defining a Green's function

$$\alpha_r \left[G(r,r') \right] = - \delta(r - r') \tag{75}$$

subject to

$$G(1, r') = G(r_c, r') = 0 \tag{76}$$

yields as a solution to equations (73) and (74)

$$u(r, t) = - \int_1^{r_c} G(r, r') \frac{\partial y(r', t)}{\partial t} \, dr' \tag{77}$$

Substituting equation (77) into equation (72), using equations (66) and (70), and providing the order of integration may be justifiably changed,

$$T(r) = \frac{\int_1^{r_c} \frac{\partial}{\partial r} [G(r, r')] [y^{(s)}(r') - a(r')] \, dr'}{d y^{(s)} / dr} \tag{78}$$

Thus the problem is reduced to finding a solution to equations (75) and (76). The Green's function may be written:

$$G(r, r') = \frac{\varrho' r'^2 e^{m/r'}}{m[e^{-m} - e^{m/r_c}]} \left\{ [e^{-m/r_c} - e^{-m}][e^{-m/r'} - e^{m/r_c}] H(r' - r) + \right.$$
$$\left. + [e^{-m/r'} - e^{-m}][e^{-m/r} - e^{-m/r_c}] H(r - r') \right\} \tag{79}$$

where H is the Heaviside unit operator. The greatest interest is at r = 1 so that substituting equation (79) in to (78) and evaluating T(r) at r = 1,

$$T(1) = \frac{1}{\frac{dy^{(s)}}{dr}\bigg)_{r=1} [1 - e^{m(1 - \frac{1}{r_c})}]} \int_1^{r_c} \varrho' r'^2 [1 - e^{m(\frac{1}{r'} - 1)}] [y^{(s)}(r') - a(r')] \, dr' \tag{80}$$

The steady-state solution may be obtained from the previous problem as

$$y^{(s)} = \frac{1}{B} [e^{m(1 - \frac{1}{r})} - 1]$$

so that the time lag is:

$$T(1) = \frac{B(\frac{1}{r_c} - 1)}{\ln(1 + B)} \int_1^{r_c} \varrho' r'^2 \left[\frac{y^{(s)}(r')}{B y^{(s)}(r') + 1}\right] [y^{(s)}(r') - a(r')] \, dr' \tag{81}$$

This integral blows up if r_c is extended to large values of r. However, practically r_c is kept finite by convection, burning, or space limitations. Converting this time lag to a physical basis by equation (67):

$$\tau_{lag}^{*}(o) \Big/ t_f^{*} = \frac{T(1)}{K} \tag{82}$$

In order to discuss the meaning of equations (81) and (63) it is perhaps best to compute some numbers typical of rocket engine performance. The data are taken from Ref. 21 for a chamber pressure of 300 psia and a combustion gas temperature of 5000°R. A usual initial condition $a(r) = 1$ is chosen. $r_c = 5$ is chosen and heptane is assumed burning with liquid oxygen.

Propellant Remarks	C	T_L^* °R	ℓ/ρ_c^*	B^+	τ		K	T(1) order of magnitude	$t_{lag(1)}^*/t_f^*$ order of magnitude
Heptane	0.8	835	183.1	13.6	0.167	0.053	27.3	5	0.2
Liquid O_2	0.8	230	331	19.3	0.046	0.002	44.8	4	0.1

This short and rather specialized set of numbers shows some interesting facts which, however, may be altered for lower temperature work. First, because of the small value of ϵ, little error is made in stopping at the zeroth order term in ϵ in the first order term in $1/K$. The typical values of K show that approximately 3% error is made in predicting r_L if the quasi-steady assumption is made once the initial condition is reached. It also shows that although for the same drop size

---

+In quasi-steady theory the assumption of equal specific heats between the species may be relaxed. B is computed using the specific heat of the vaporizing species which is correct under the quasi-steady assumption.

oxygen has a shorter lifetime than heptane (21), the quasi-steady

assumption is poorer for heptane than for liquid oxygen. Such a result

is also true from the standpoint of initial condition relaxation. Assuming

t_f^* to be the droplet lifetime (which is, however, inconsistent with the

derivation of $\top$, a substantial portion of this time is spent in relaxing

the initial condition. In fact, it is comparable with the heating-up

period to the wet bulb temperature (21). Recalling that the initial

condition was quite severe, however, it might be conjectured that such

a condition hastens the heating-up period and vapor stratification around

the droplet so that the combined period of initial condition relaxation

and heating-up takes place in substantially the same time. This combined

condition should, however, be given some theoretical consideration. Again

it should be pointed out that the initial condition relaxation time

was developed on a basis which should not allow such a severe initial

condition. Finally, it is necessary to note that, as expected, the

validity of the quasi-steady assumption rests heavily on the ratio

between the liquid and gas densities. Therefore, in a very high pressure

rocket chamber the quasi-steady assumption becomes poorer.

REFERENCES

1. Crocco, L., Harrje, D. T., Reardon, F. H., and Strahle, W. C., "Combustion Instability in Liquid Propellant Rocket Motors" (Thirty-fifth Progress Report), Princeton University Aeronautical Engineering Report No. 216 - ii, June, 1961.

2. Crocco, L., Harrje, D. T., Sirignano, W. A., and Ashford, D. M., "Nonlinear Aspects of Combustion Instability in Liquid Propellant Rocket Motors" (First yearly Progress Report), Princeton University Aeronautical Engineering Report No. 553, June, 1961.

3. Crocco, L., Harrje, D. T., and Reardon, F. H., "Transverse Combustion Instability in Liquid Propellant Rocket Motors", ARS Journal, Vol. 32, No. 3, March, 1962, pp. 366-73.

4. Reardon, F. H., Crocco, L., and Harrje, D. T., "An Investigation of Transverse Mode Combustion Instability in Liquid Propellant Rocket Motors", Princeton University Aeronautical Engineering Report 550.

5. Crocco, L., Harrje, D. T., and Reardon, F. H., "Combustion Instability in Liquid Propellant Rocket Motors" (Thirty-fourth Progress Report), Princeton University Aeronautical Engineering Report No. 216-hh, November, 1960.

6. Somogyi, D., and Feiler, C. E., "Mixture Ratio Distribution in the Drops of Spray Produced by Impinging Liquid Streams", ARS Journal, vol. 30, No. 2, February 1960, pp 185 - 187.

7. Crocco, L., and Cheng, S. I., "Theory of Combustion Instability in Liquid Propellant Rocket Motors", AGARDograph No. 8, Butterworths Publications Ltd., London, 1956.

8. Rupe, J., " A Correlation Between the Dynamic Properties of a Pair of Impinging Streams and the Uniformity of Mixture Ratio Distribution in the Resulting Spray". J.P.L., PR 20 - 209, March 28, 1956.

9. Allen, W. D., "Experimental Studies of Transverse Waves in a Cylindrical Chamber", Princeton University Aeronautical Engineering Report No. 607, June 8, 1962.

10. Crocco, L., and Harrje, D. T., "Combustion Instability in Liquid Propellant Rocket Motors", (Twenty-sixth Quarterly Progress Report), Princeton University Aeronautical Engineering Report No. 216-Z, February, 1959.

11. Crocco, L., Grey, J., and Harrje, D. T., "Theory of Liquid Propellant Rocket Combustion Instability and Its Experimental Verification", ARS Journal, Vol. 30, No. 2, February, 1960, pp. 159-68.

12. Cohen, N., and Webb, M., "Evaluation of Swirl Atomizer Spray Characteristics by a Light Scattering Technique", Princeton University Aeronautical Engineering Report No. 597, February, 1962.

13. Dobbins, R. A., "Light Scattering and Transmission Properties of Sprays", Princeton University Aeronautical Engineering Report No. 530, November, 1960.

14. Foa, J. V., "Mach Number Functions for Ideal Diatomic Gases", Cornell Aeronautical Laboratory, Inc., Buffalo, New York, October, 1949.

15. Bartz, D. R., "A Simple Equation for Rapid Estimation of Rocket Nozzle Convertive Heat Transfer Coefficients", Jet Propulsion, Vol. 27, No. 1, January, 1957.

16. Bartz, D. R., "An Approximate Solution of Compressible Turbulent Boundary - Layer Development and Convective Heat Transfer in Convergent - Divergent Nozzles", Transactions of the ASME, Vol. 77, No. 8, November, 1955.

17. Voitsekhouskii, B. V., "Maintained Detonations", Soviet Physics Doklady, Vol. 4, No. 6, May, 1960

18. Sommers, W. P., "The Interaction of a Detonation Wave with an Inert Boundary" (Ph. D. Thesis), University of Michigan, Report IP-501, March, 1961.

19. Culick, F. E. C., "Stability of High Frequency Pressure Oscillations in Gas and Liquid Rocket Combustion Chambers", M.I.T. Aerophysics Lab. Tech. Rep. 480, June, 1961.

20. Pelmas, R., Glassman, I., and Webb, M., "An Experimental Investigation of Longitudinal Combustion Instability in a Rocket Motor Using Premixed Gaseous Propellants", Princeton University Aeronautical Engineering Report No. 589, December, 1961.

21. Priem, R. J., and Heidmann, M. F., "Propellant Vaporization as a Design Criterion for Rocket Engine Combustion Chambers", NASA Tech. Rep. R-67, 1960.

22. Adler, J., "A One - Dimensional Theory of Liquid Fuel Rocket Combustion III: The Effect of Non - Uniform Droplet Radii, Injection Velocities, and Physical Properties", British A. R. C. Tech. Rep. 20, 830, February 18, 1959.

23. Spalding, D. B., " A One - Dimensional Theory of Liquid - Fuel Rocket Combustion", British A. R. C. Tech. Rep. 20, 175, 1959.

24. Scala, S. M., "Transverse Wave and Entropy Wave Combustion Instability in Liquid Propellant Rockets", Princeton University Aeronautical Engineering Report No. 380, April, 1957.

25. Penner, S. S., and Fuhs, A. E., "On Generalized Scaling Procedures for Liquid - Fuel Rocket Engines", Combustion and Flame, Vol. 1, No. 2, June, 1957.

26. Penner, S. S., "Chemistry Problem in Jet Propulsion", Permagon Press, New York, 1957.

27. Fuchs, N., "Concerning the Velocity of Evaporation of Small Droplets in a Gas Atmosphere", _Physikalische Zeitschrift der Sowjetunion_, Vol. 6, 1934.

28. Kirkaldy, I. J., "The Time Dependent Diffusion Theory for Condensation on Spherical and Plane Surfaces", _Canadian Journal of Physics_, Vol. 36, No. 4, April, 1958.

29. Kolodner, I. I., "Free Boundary Problem for the Heat Equation with Applications to Change of Phase", _Communications on Pure and Applied Mathematics_, Vol. IX, No. 1, February, 1956.

30. Carslaw, H. S., and Jaeger, J. C., "Conduction of Heat in Solids", 2nd Edition, Clarendon Press, Oxford, England, 1959.

31. Frisch, H. L., "Time Lag in Transport Theory", _J. Chem. Phys._, Vol. 36, No. 3, January 15, 1962.

32. Krieg, H. C., Jr., "The Tangential Mode of Combustion Instability", ARS Preprint No. 1723-61, Palm Beach, Florida, April, 1961.

33. Mower, W., Baker, D., and Jackson, E., "Application of Stability Rating Techniques to Large Thrust Chambers" (CONFIDENTIAL) ARS Meeting, Palm Beach, Florida, April, 1961.

(a) 1 group of 12 spuds
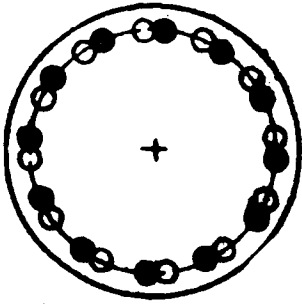
Spinning - favorable
Standing - unfavorable

(b) 2 groups of 5 spuds + 2 groups of 1 spud
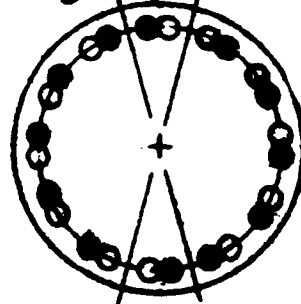
Spinning - favorable
Standing - unfavorable

(c) 2 groups of 6 spuds
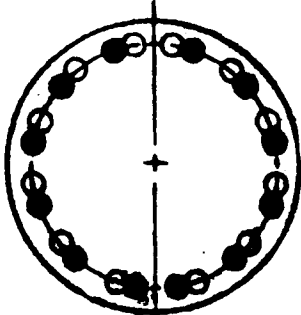
Spinning - unfavorable
Standing - unfavorable

(d) 4 groups of 3 spuds
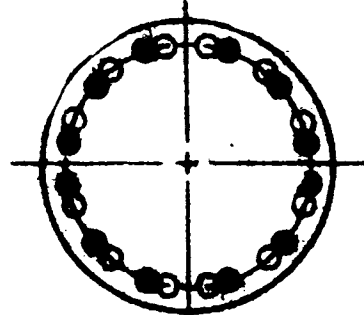
Spinning - unfavorable
Standing - favorable (1T, 3T)

(e) 6 groups of 2 spuds
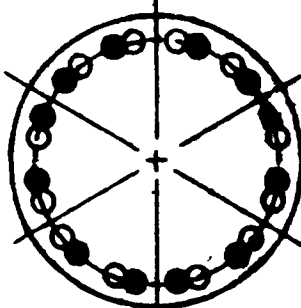
Spinning - unfavorable
Standing - unfavorable

(f) 12 groups of 1 spud
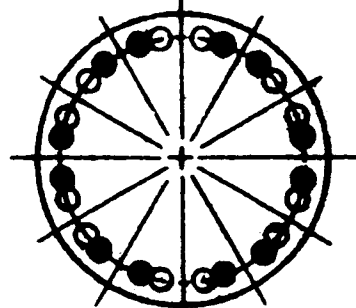
Spinning - unfavorable
Standing - favorable (3T)

Linear velocity sensitivity characteristics of tangential injectors

Figure 1

Figure 2

Chamber arrangement for investigating orientation effects on stability limits

9-7 tangential, 1.4 design $\bar{r}$, 500 lb. thrust

Figure 3

First tangential
Spinning mode
(no baffle)

$t \longrightarrow$

First tangential
Standing mode
(with baffle)

$t \longrightarrow$
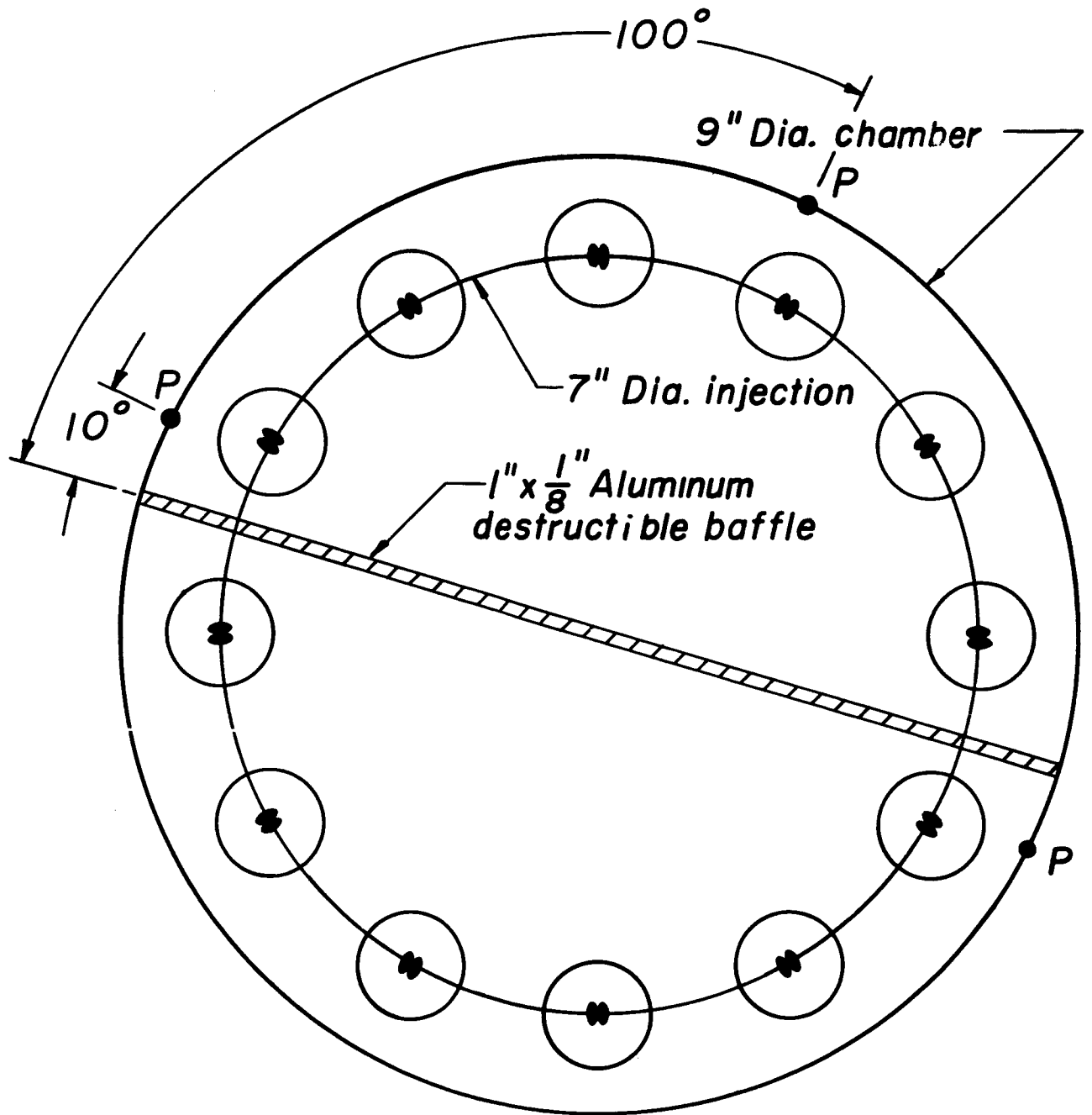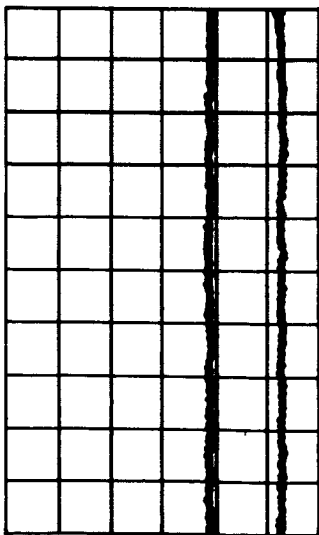
Stable
(with or without baffle)

$t \longrightarrow$

P_2

P_1

P_2

P_1

P_2

P_1

90°
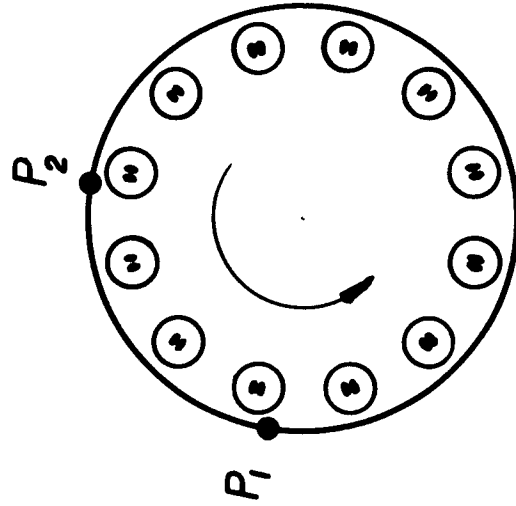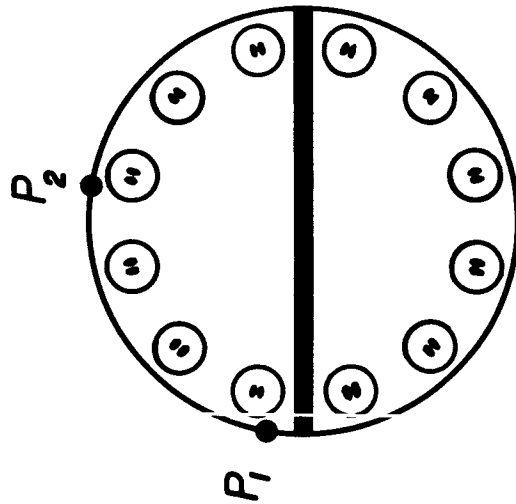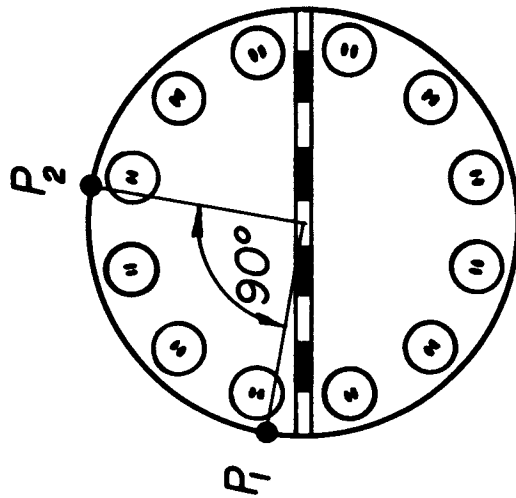
Stability conditions, injection orientation tests

Figure 4a

50 millisec

$\tilde{P}=270psi$

baffle burnout

P_5

inserts shown below

P_4

Stable operation | Transition region | Spinning mode
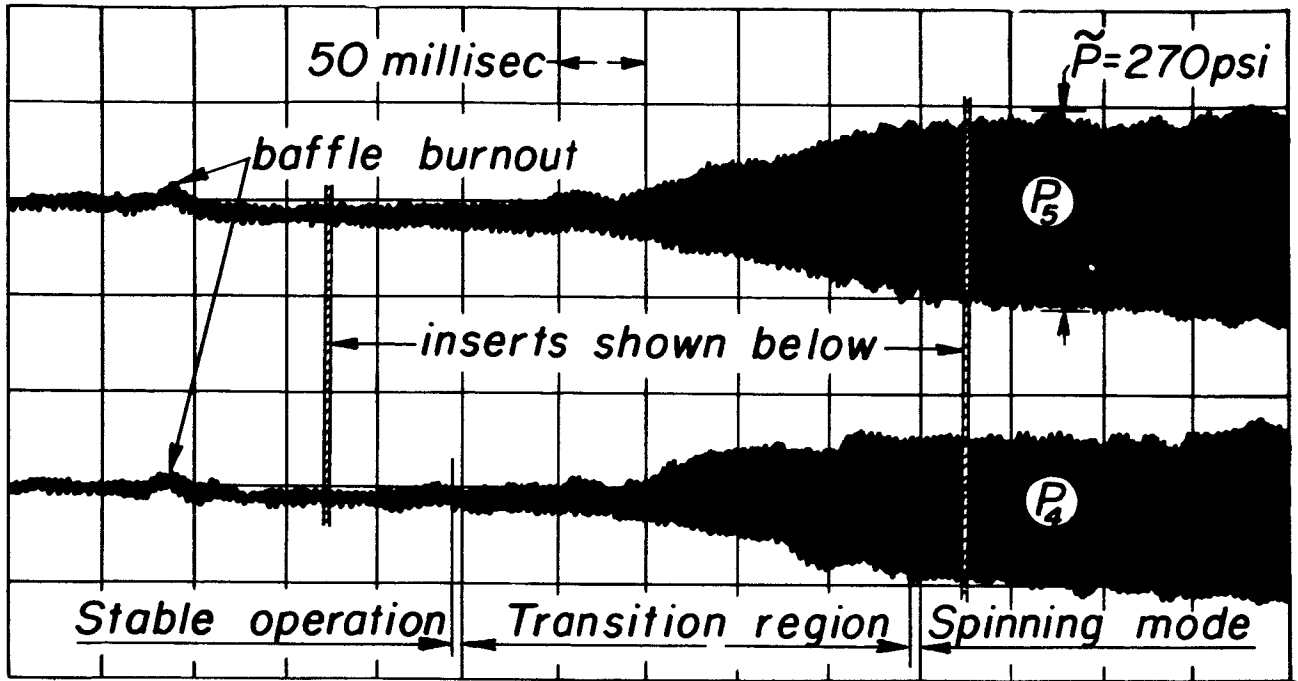
Stability record after baffle burnout

time →

P_5

P_4

5 millisec

Stable operation

P_5

P_4 leads P_5 by $90°$

P_4

5 millisec
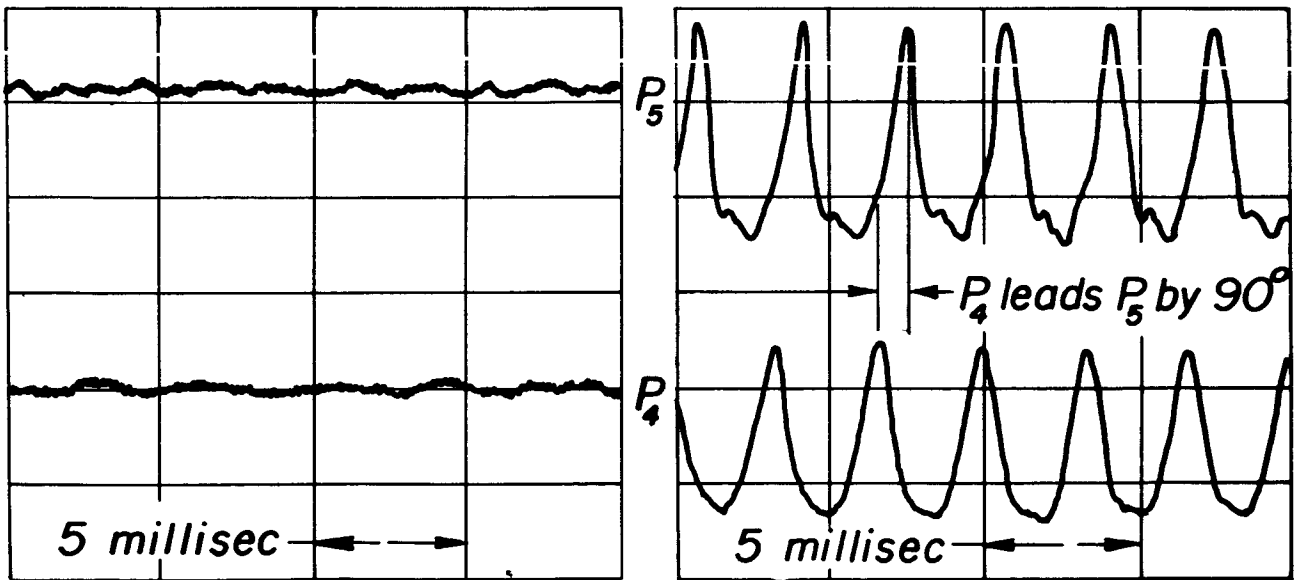
Spinning first tangential mode

Figure 4b

Figure 5

Tangential 2 × 6 orientation tests
(9" chamber, 7" injector, 150 psia, 500 lb. thrust)
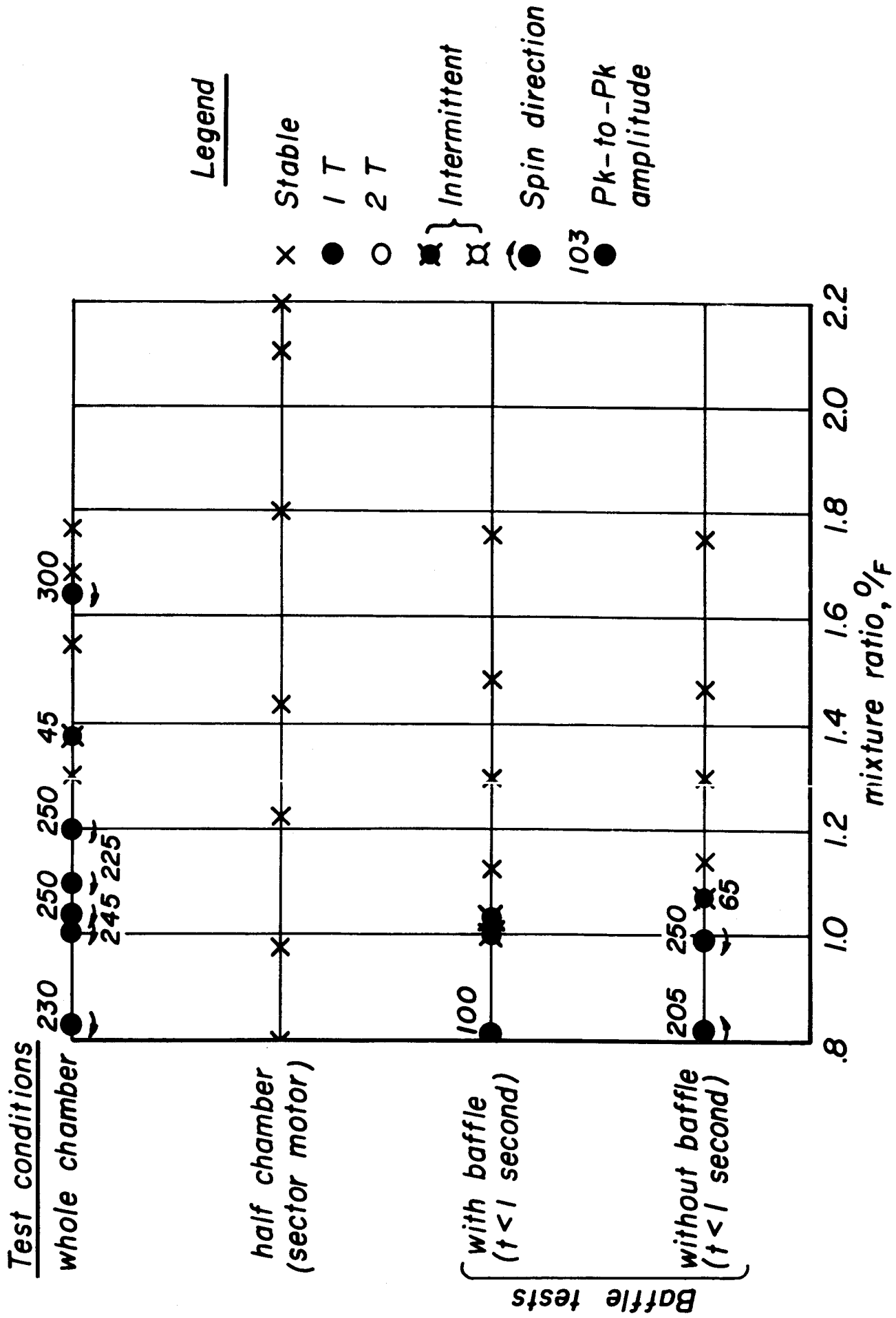
Figure 6
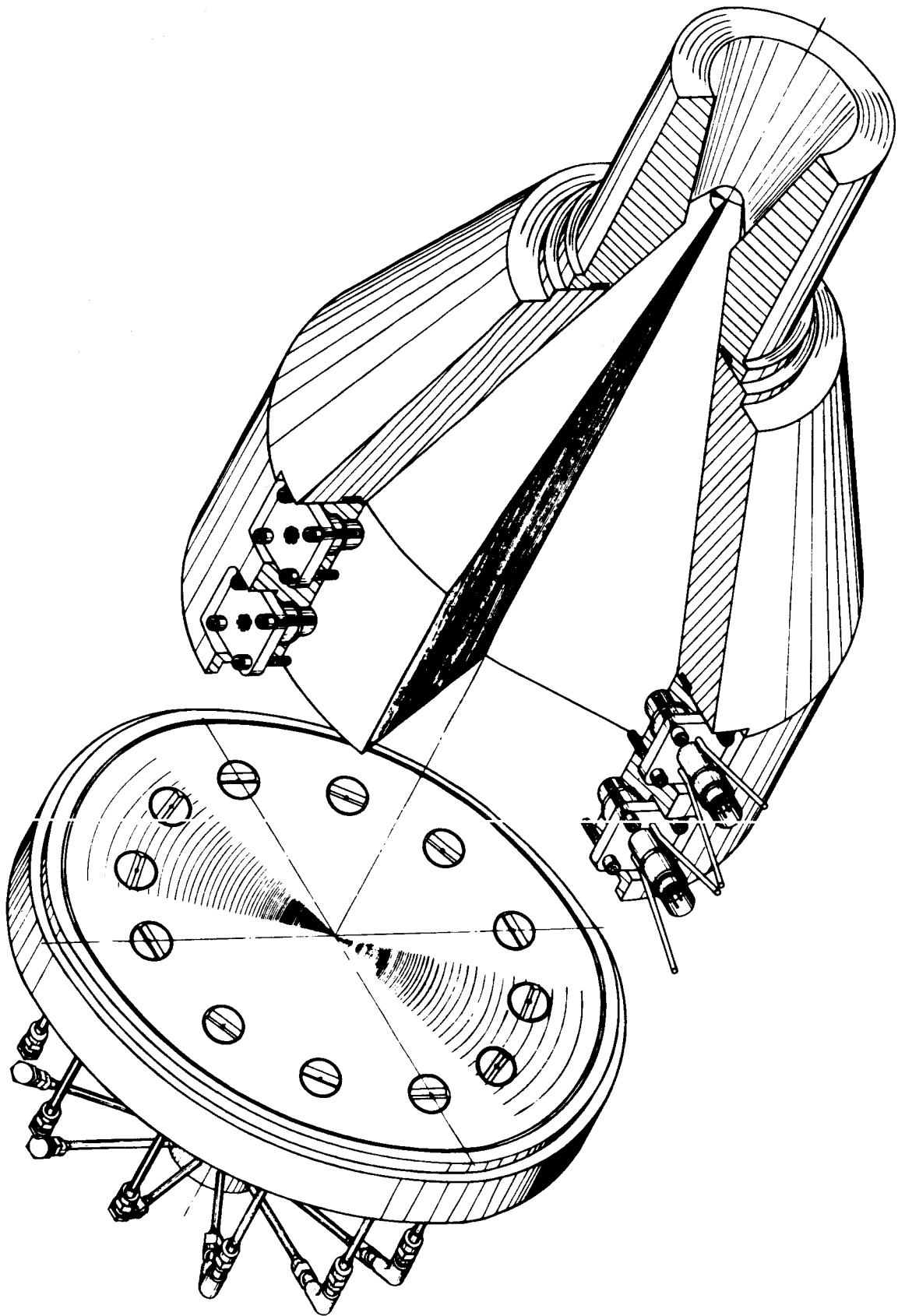
Figure 7

Sectionalized view of the variable-angle sector motor

Figure 8

Oxidizer

Injector spuds
(several possible
orientations)
total 36

Copper face &
zirconium oxide
coating

Propellant
distribution to
individual radii

Fuel
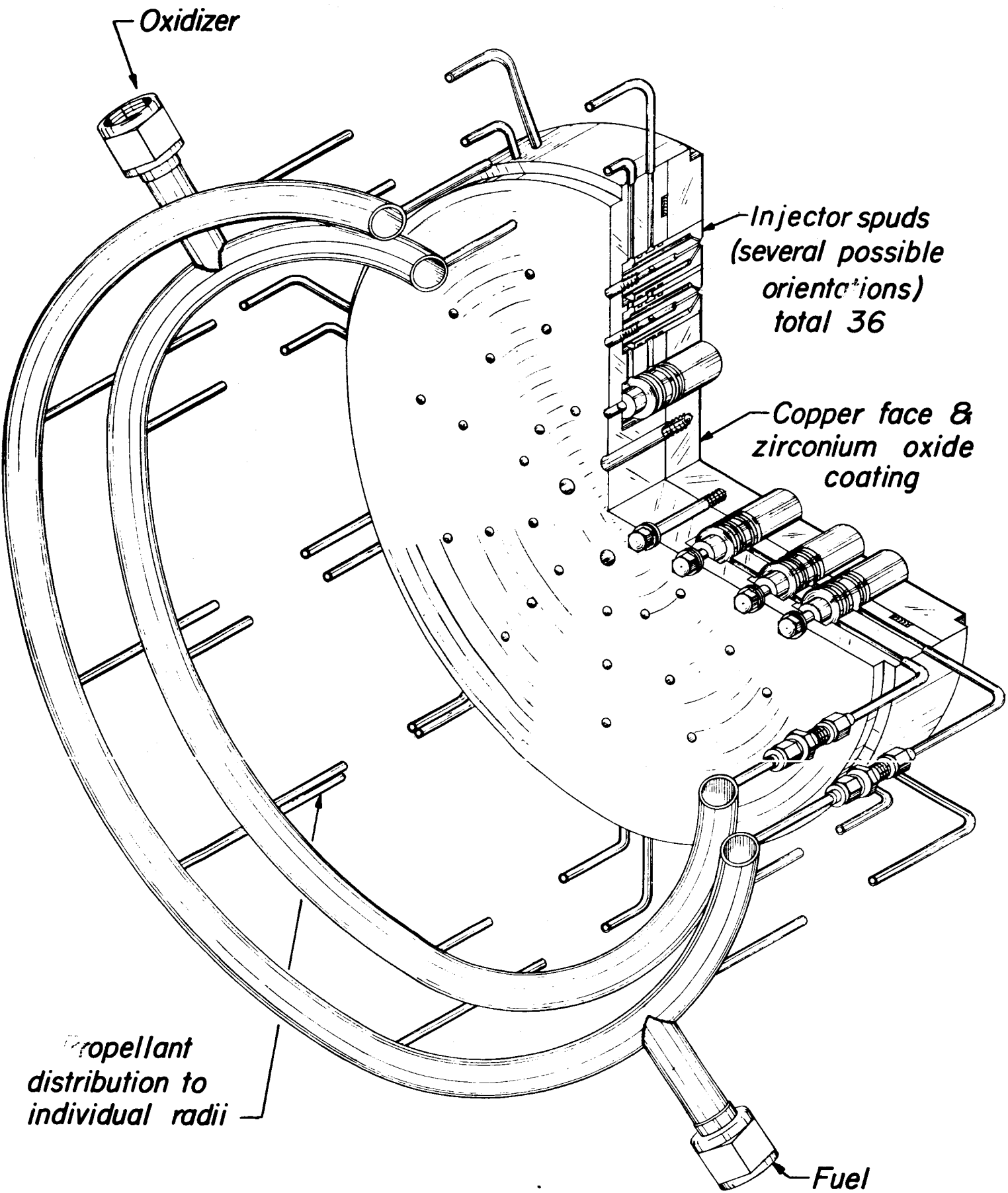
Distributed Injector
for transverse mode stability limits
Investigation

Figure 9

Radial orientation sector tests
9" chamber, distributed injector, $\bar{r}_{design} = 1.4$,
p_c (nominal) = 150 psia,   F (nominal) = 1000 lb

Key: ● IT   ○ 2T   ◑ IT & 2T mixed
     ✕ Stable   ✖ ✖ intermittent instability
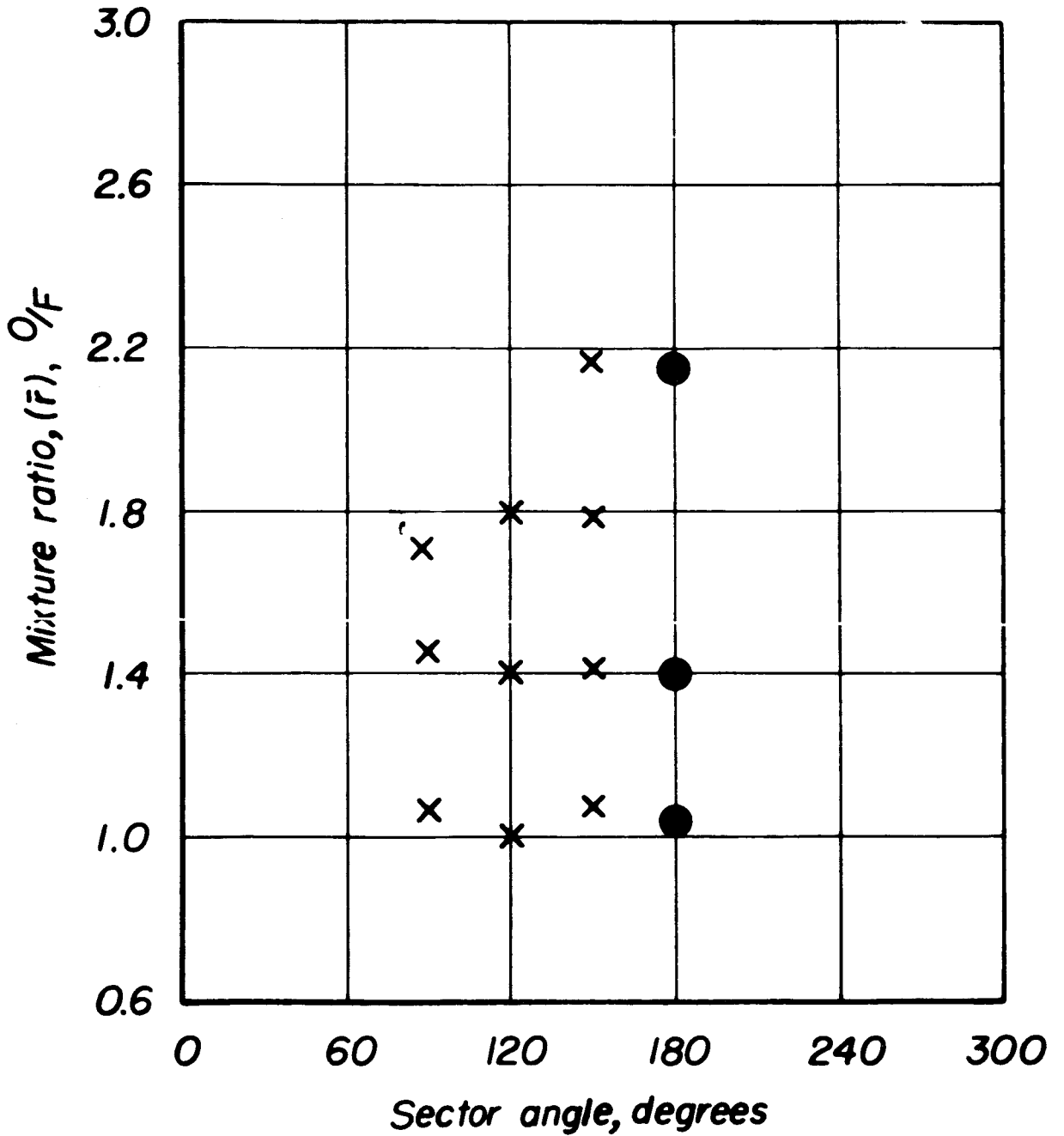
Figure 10

Tangential orientation sector tests
9" chamber, 7" Injector, $\bar{r}_{design}$ = 1.4,
p_c (nominal) = 150 psia,   F (nominal) = 1000 lb

Key: ● IT   ○ 2T   ◑ IT & 2T mixed
      ✕ Stable   ▣ ▣ intermittent instability
   numbers indicate pk-to-pk pressure amplitudes
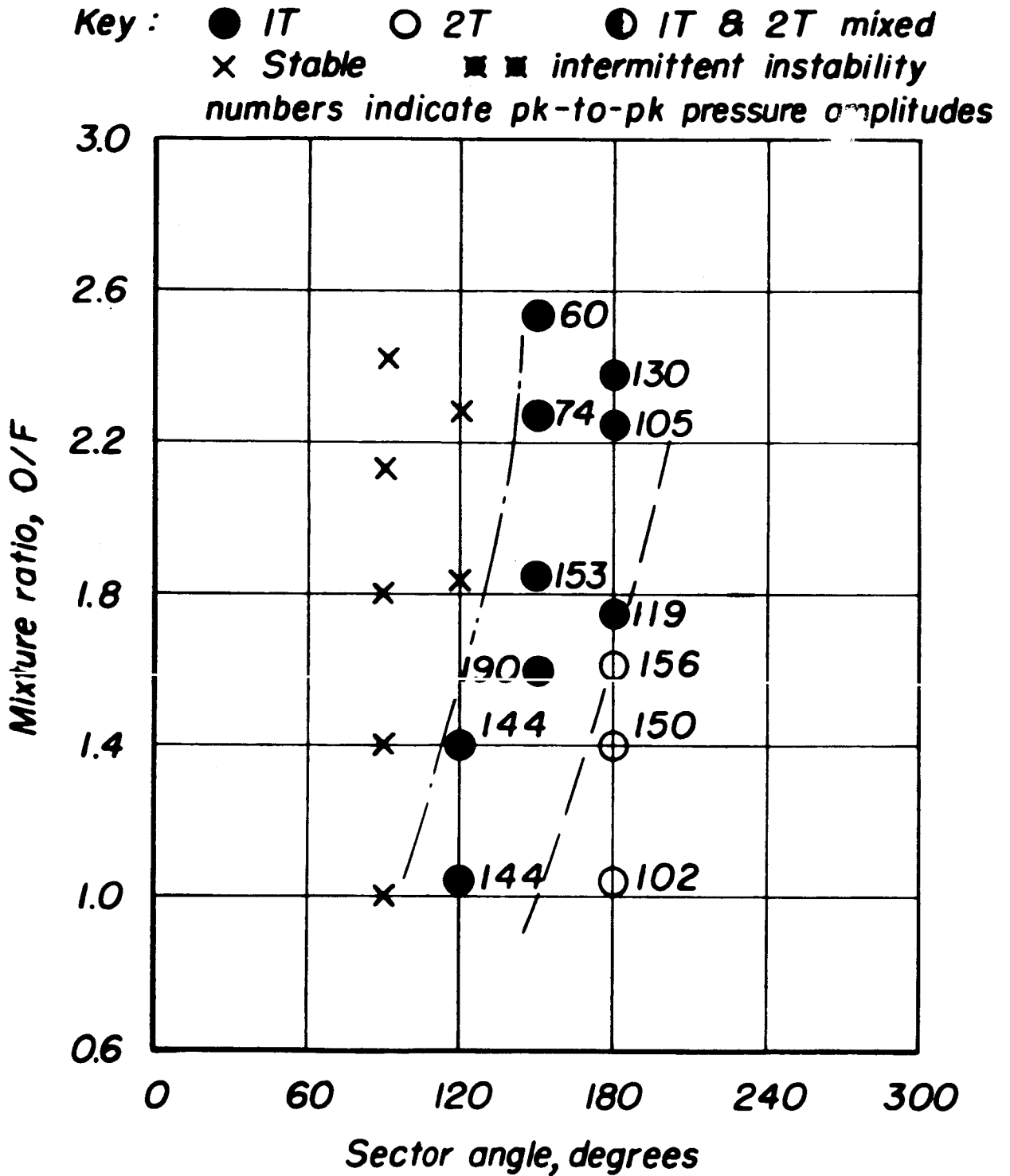
Figure 11

Theoretical sector motor stability limits, first tangential mode, 9" chamber diameter, 7" & 8" injection diameters, $p_c = 150$ psia, $F = 1000$ lb no velocity effects

Figure 12

Spark plug used with hydrogen start

Multi-orifice nozzle

Injector 30° "pie-shaped" sector from either "distributed" or "concentrated" injectors

Flat gasket

Hydraulic cylinder

Propellant feed system

Double spud

4" long chamber section typical (also 2" & 1")
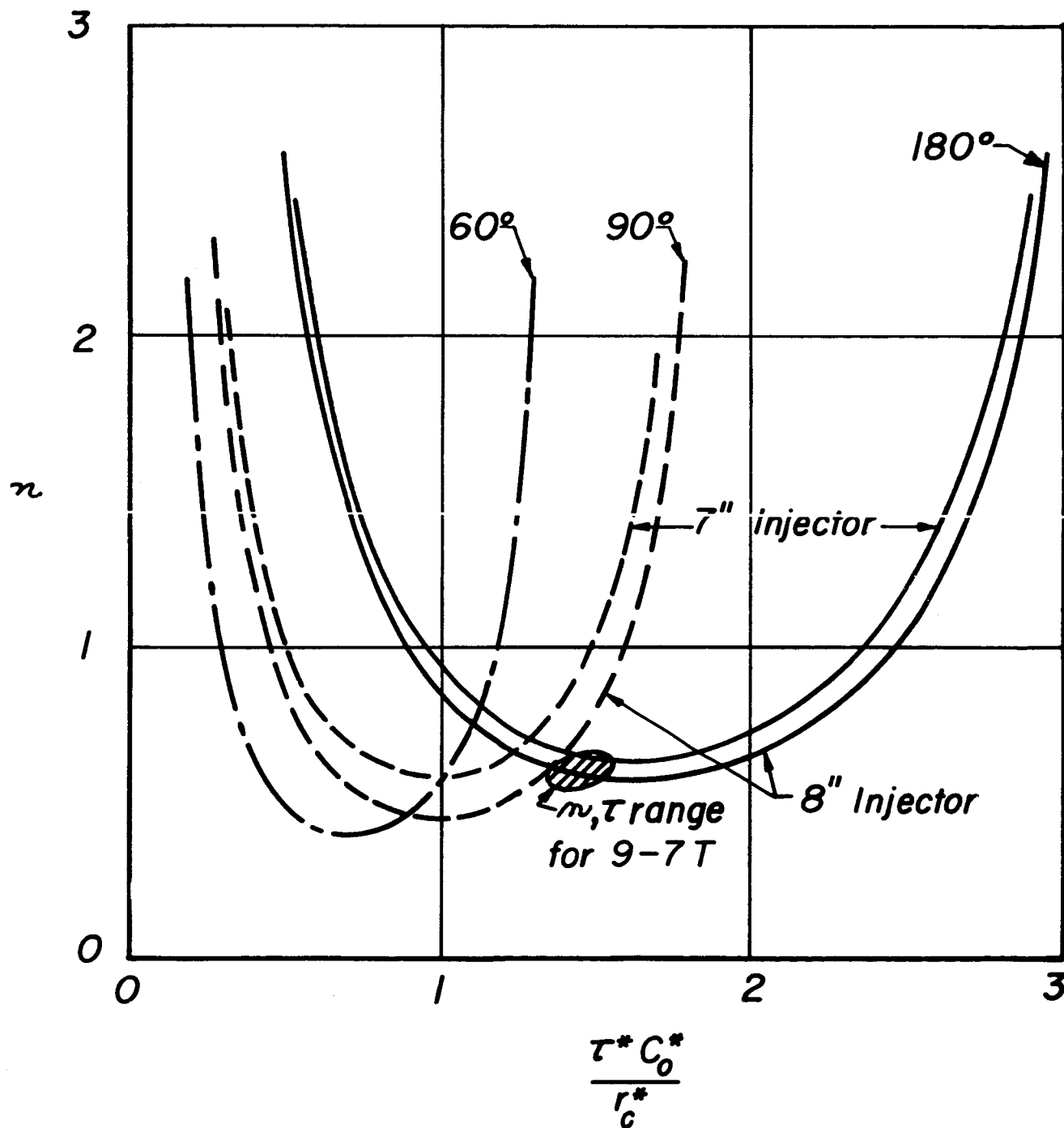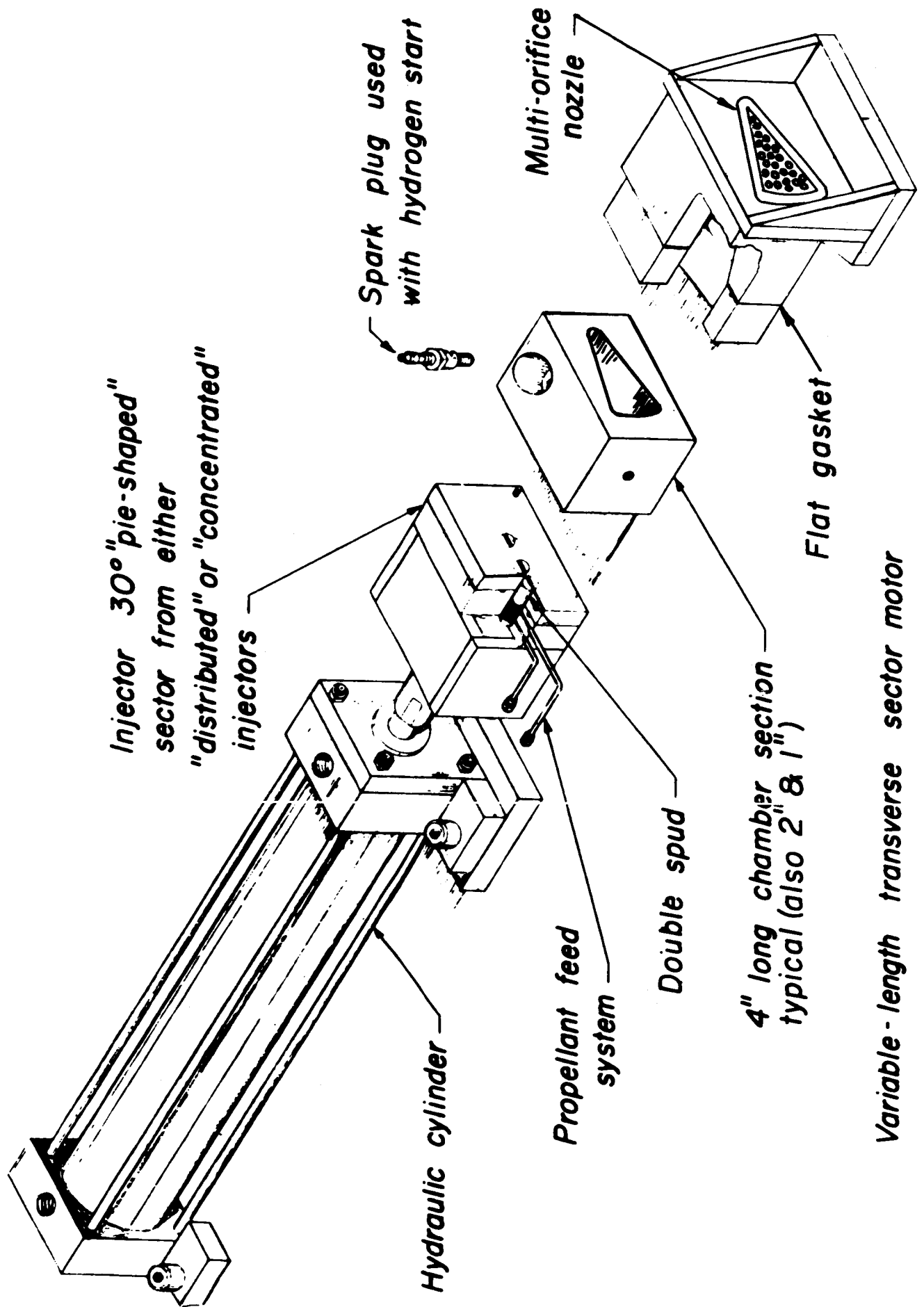
Variable-length transverse sector motor

Figure 13

Variable length, 30° sector motor tests
distributed injector (3 T pairs – .046" dia.)
1000# thrust (whole motor), 150 psia
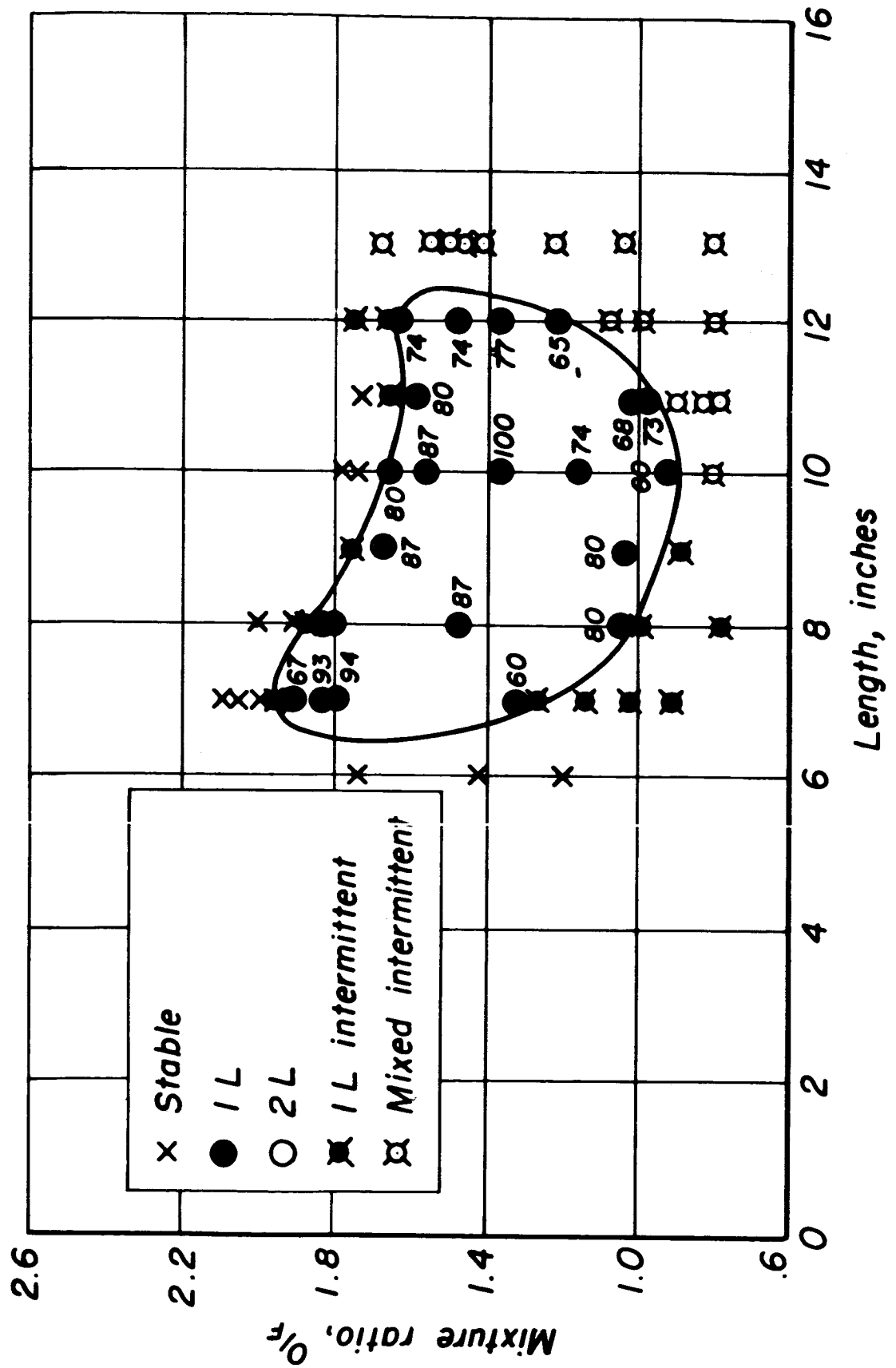
Figure 14

Variable length, 30° sector motor tests, distributed injector (3R pairs-.046" dia.-short hole i.e L/D≈5), 1,000# thrust (whole motor),150 psia

X Stable
● I Longitudinal
✱ I L intermittent
— Early tests

Mixture ratio, O/F

Length, inches
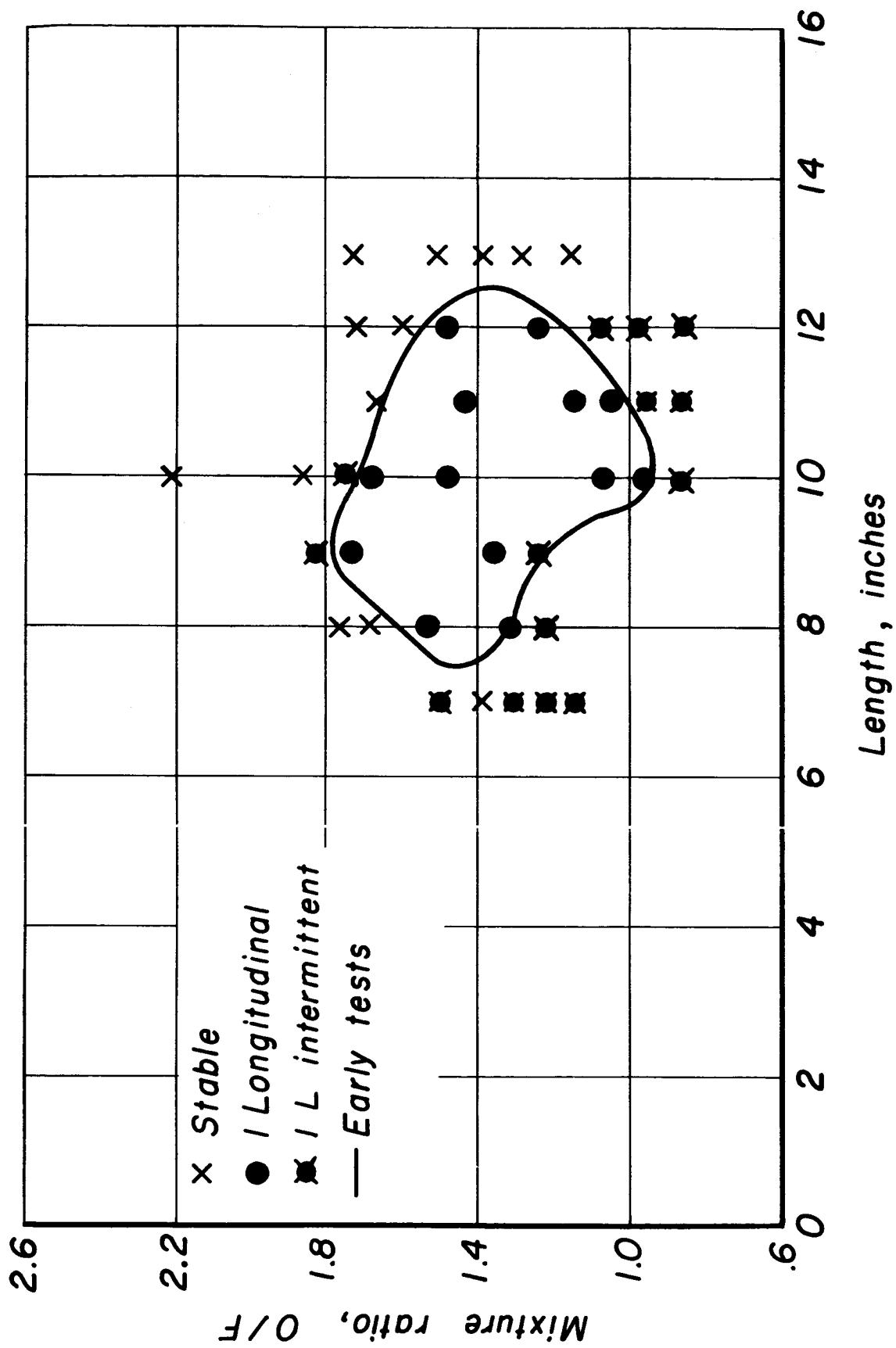
Figure 15

Variable length, 30° sector motor tests, distributed injector (3 T pairs-.046" dia. - long hole i.e. L/D ≈ 20), 1000# thrust (whole motor), 150 psia
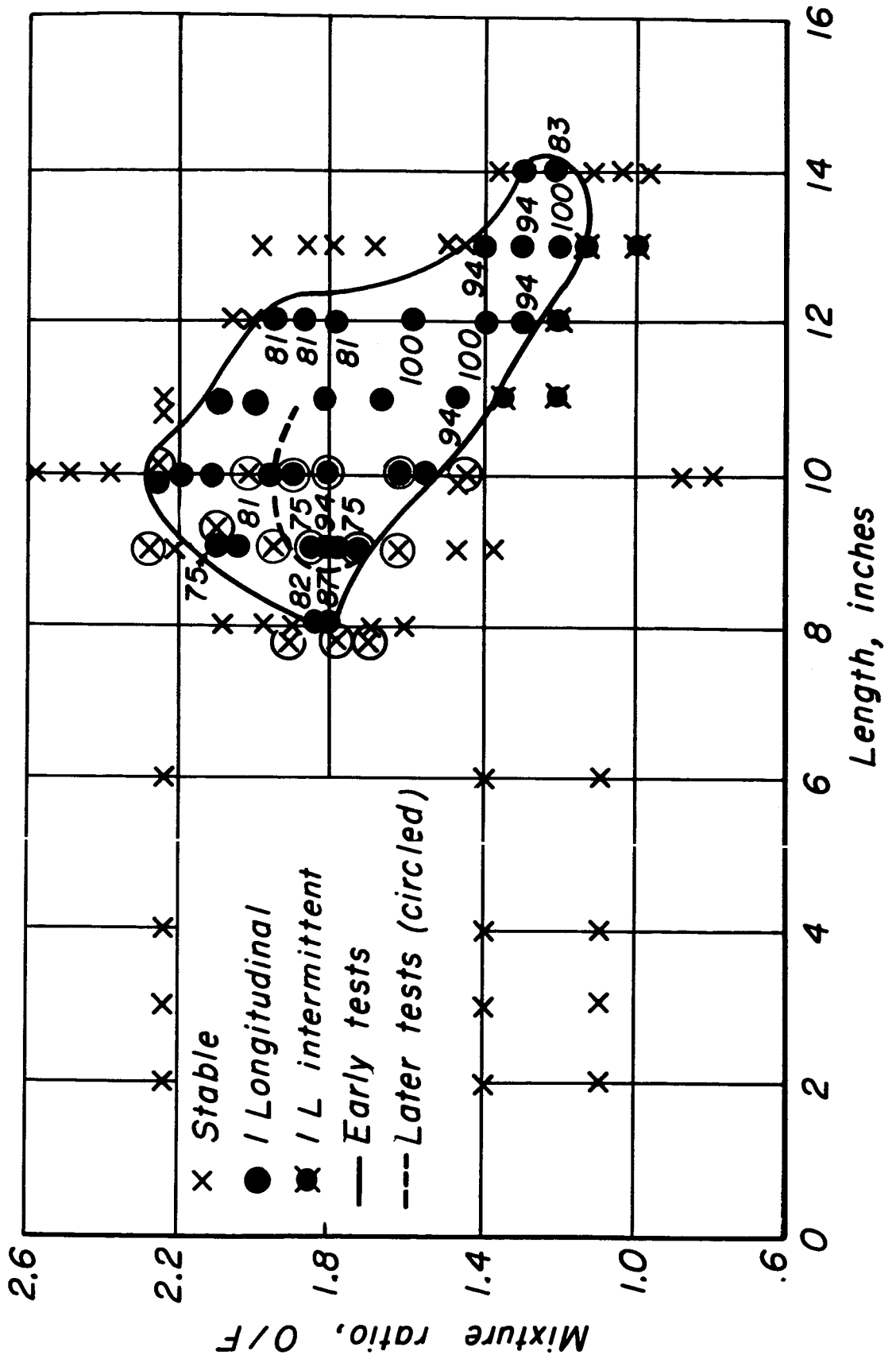
Figure 16

Performance comparison for long hole and short hole injectors ($1.4 \, \bar{r}_{design}$) using the variable-length sector motor
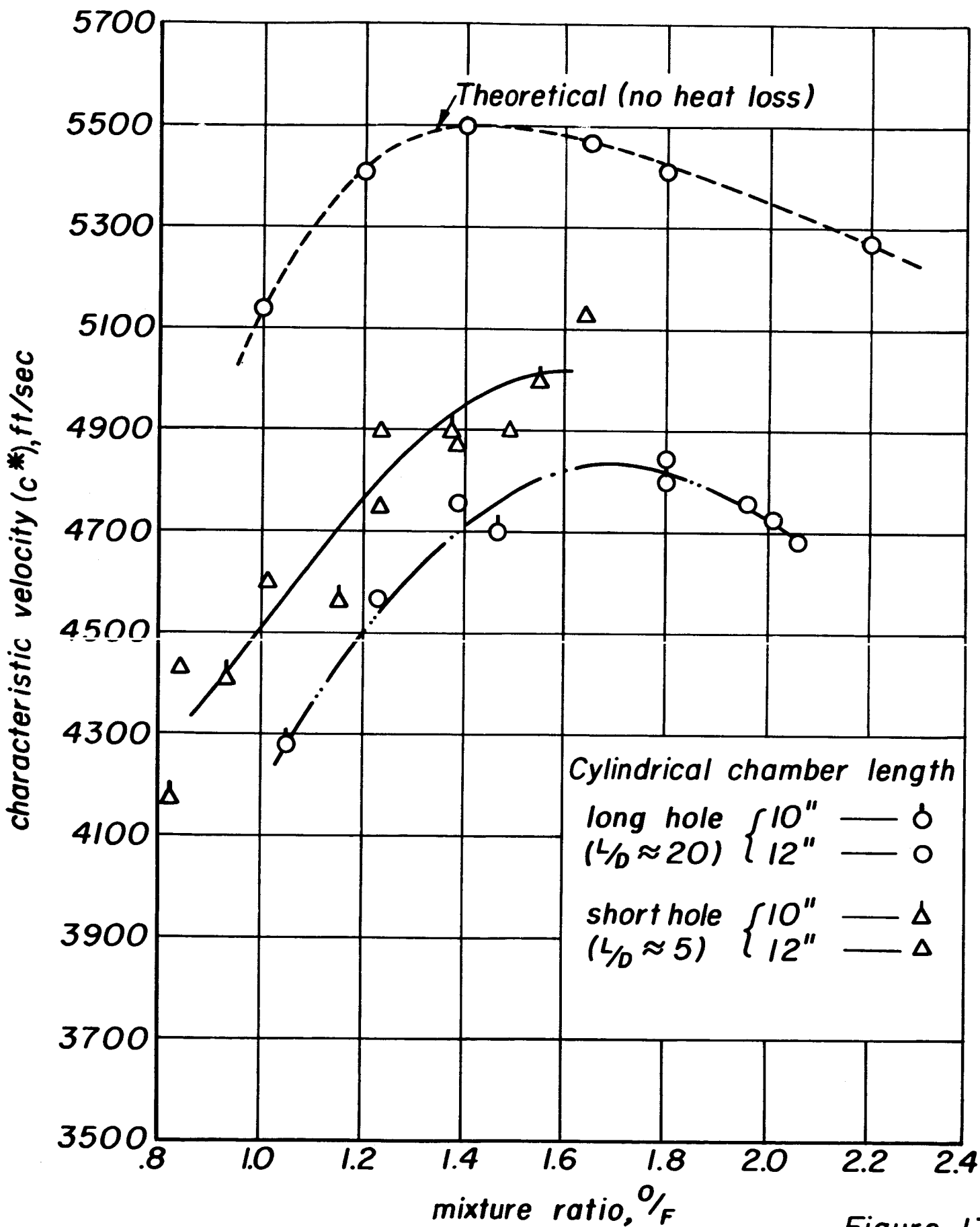
Figure 17

Performance characteristics for the variable-length 30° sector motor using the distributed injector, $\bar{r}_{design} = 1.4 - L/D = 20$ holes, 150 psia, 1000 lb thrust (whole motor)

Theoretical (no heat loss)

Cylindrical chamber length

△——△ —	15"
□—·—□ —	6"
●····● —	4"
▽—··—▽ —	3"
■——■ —	2"

characteristic velocity (c*), ft/sec

mixture ratio, O/F
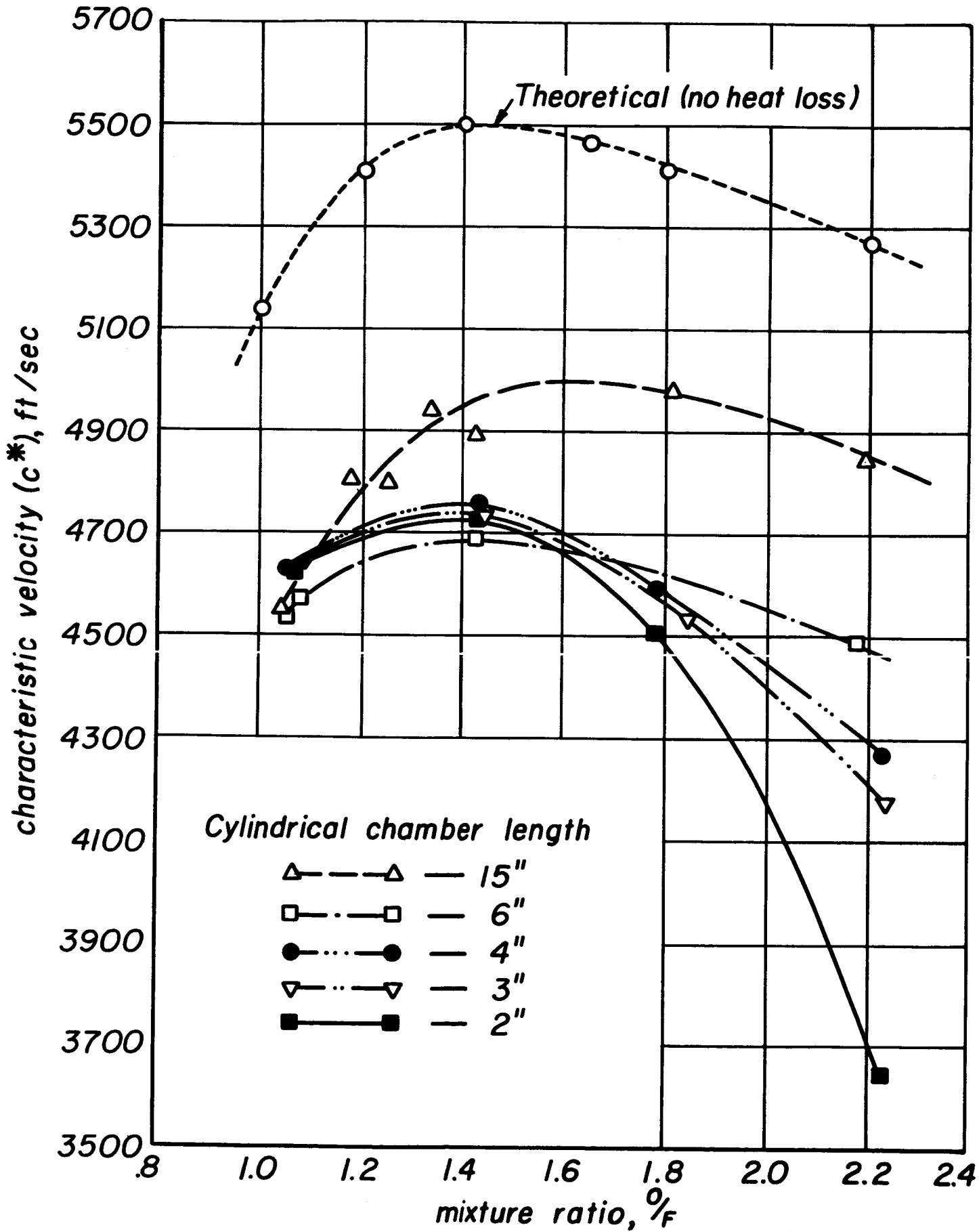
Figure 18

Theoretical longitudinal stability limits, multi-orifice nozzle
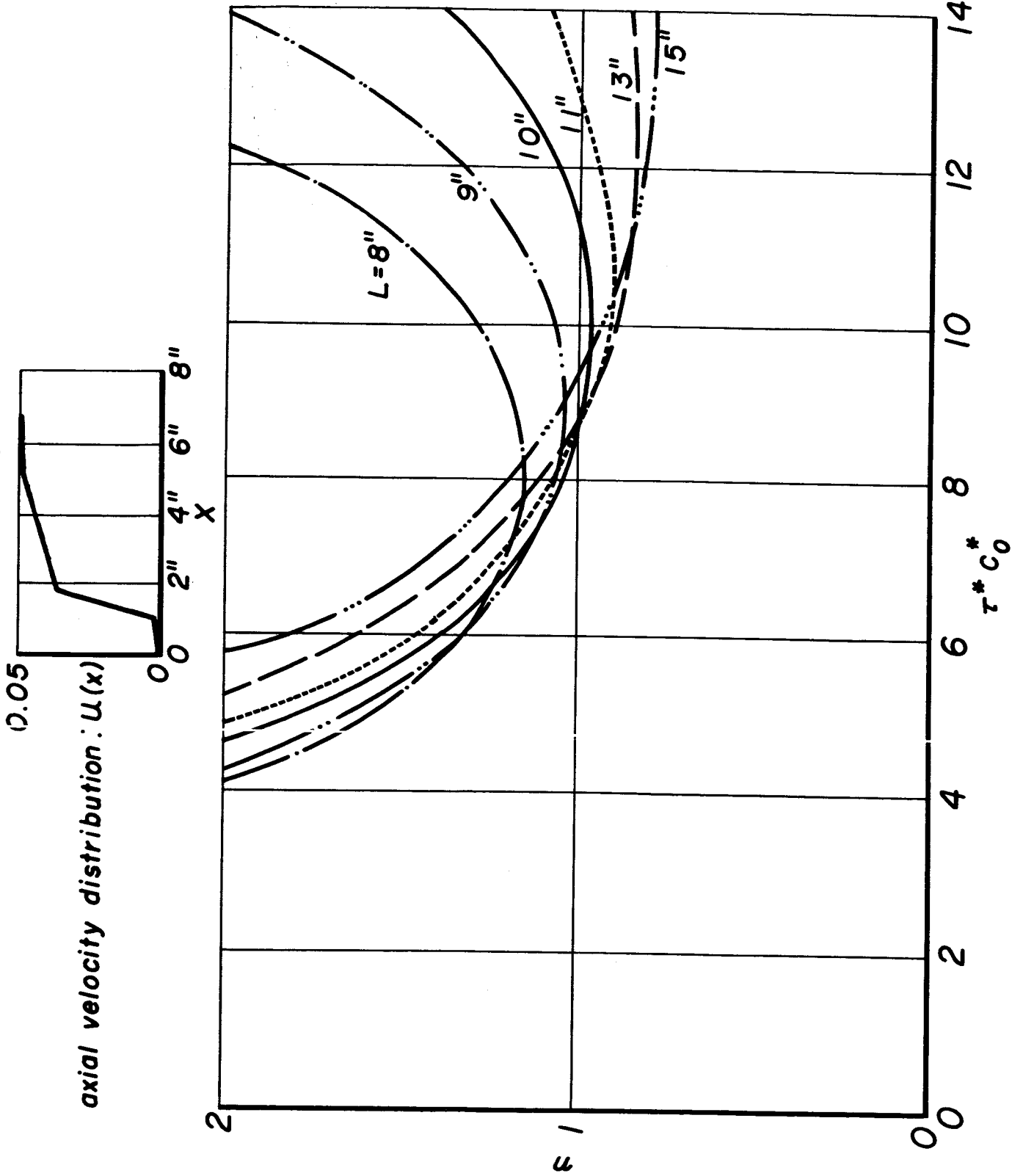
Figure 19a

Theoretical longitudinal stability limits, multi-orifice nozzle

axial velocity distribution: $u_o(x)$
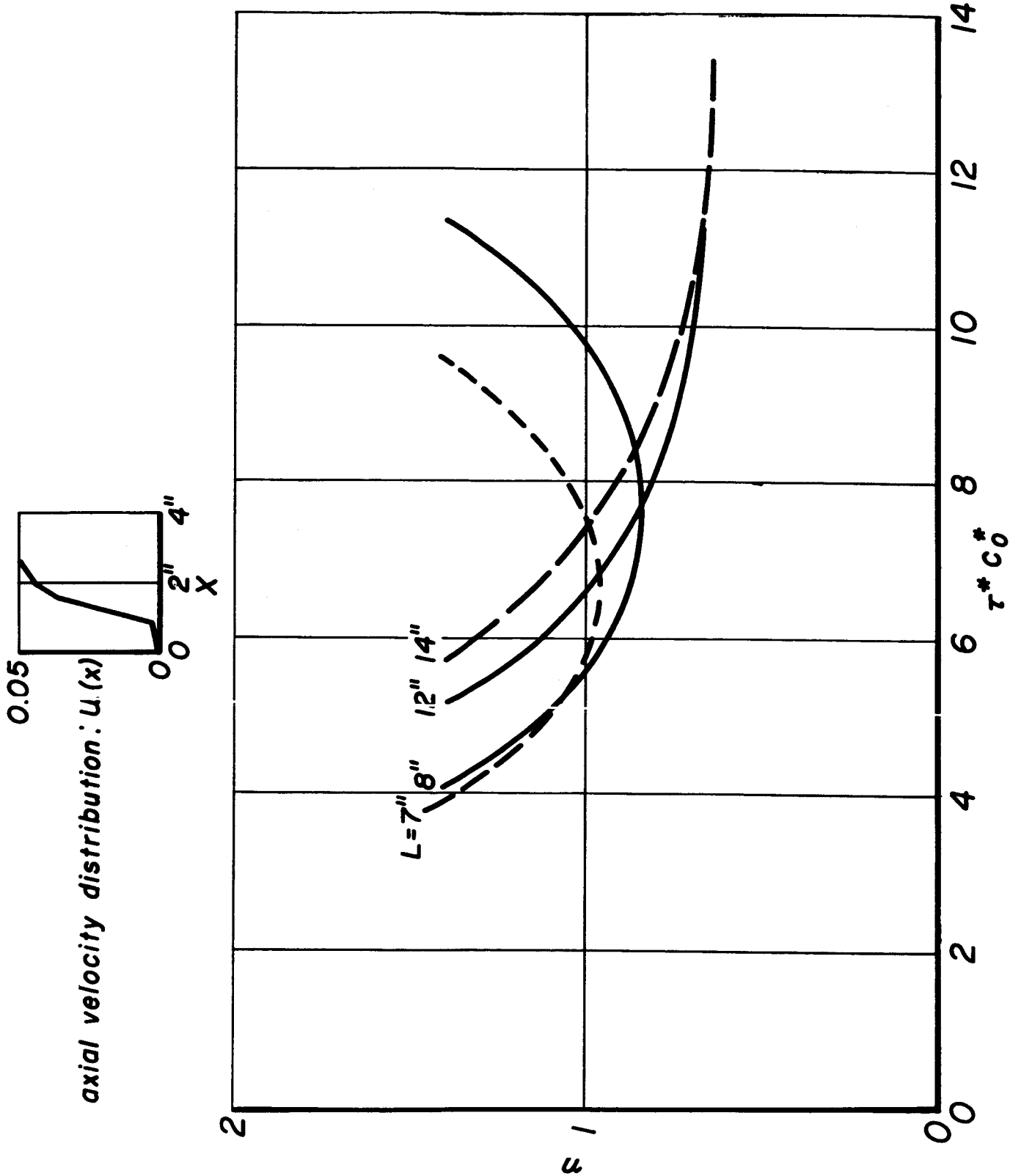
Figure 19b

Effect of nozzle heat loss on c* as deduced from stability limits testing with the variable-length 30° sector motor

heat transfer correction

o----o Theoretical (no heat loss)
□——□ Theoretical measurement through isentropic nozzle from stability limits measurement
△——△ 15" experimental measurement
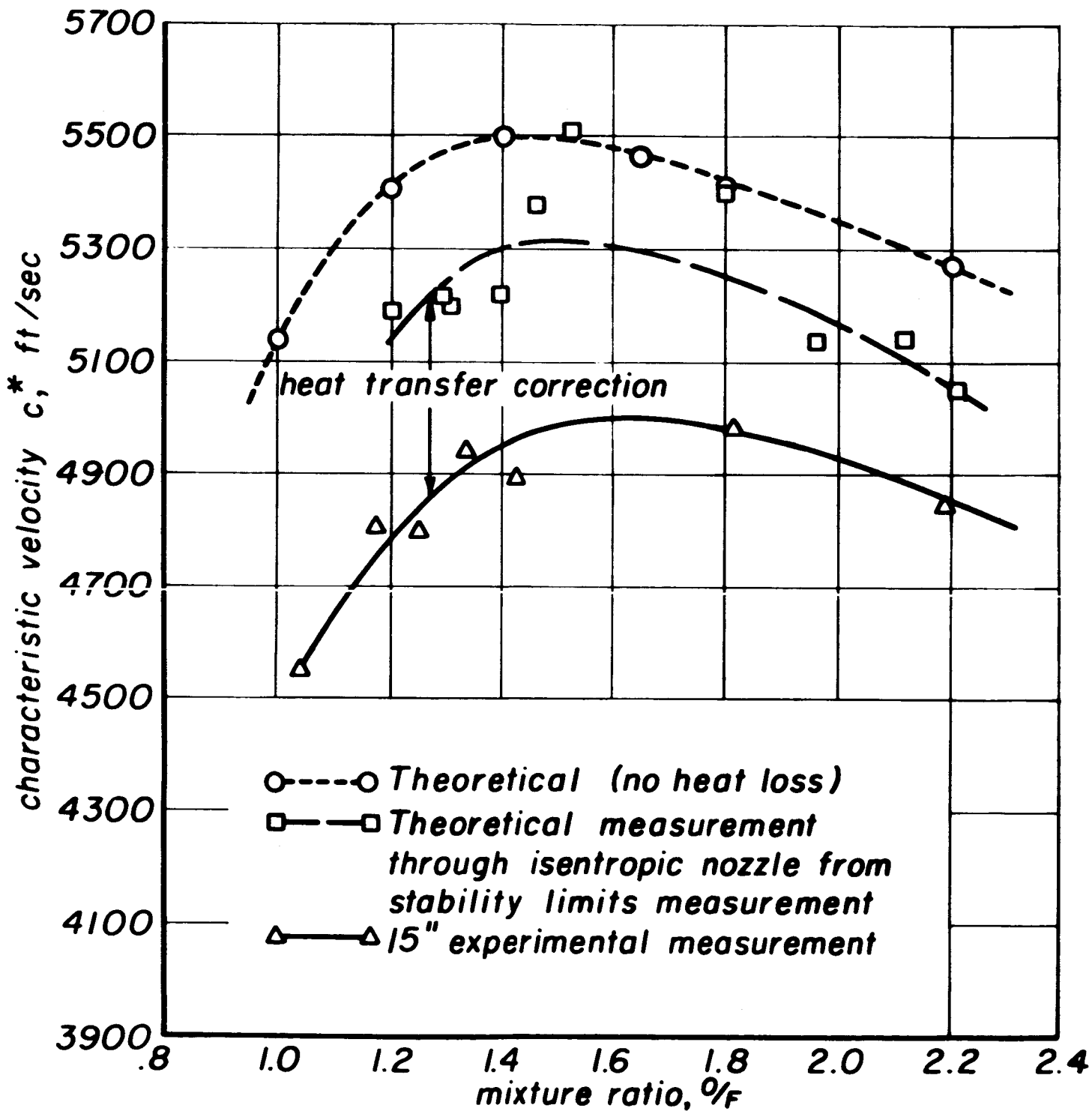
Figure 20a

Comparison between theoretical and experimental C* losses for sector motor, multiorifice nozzle
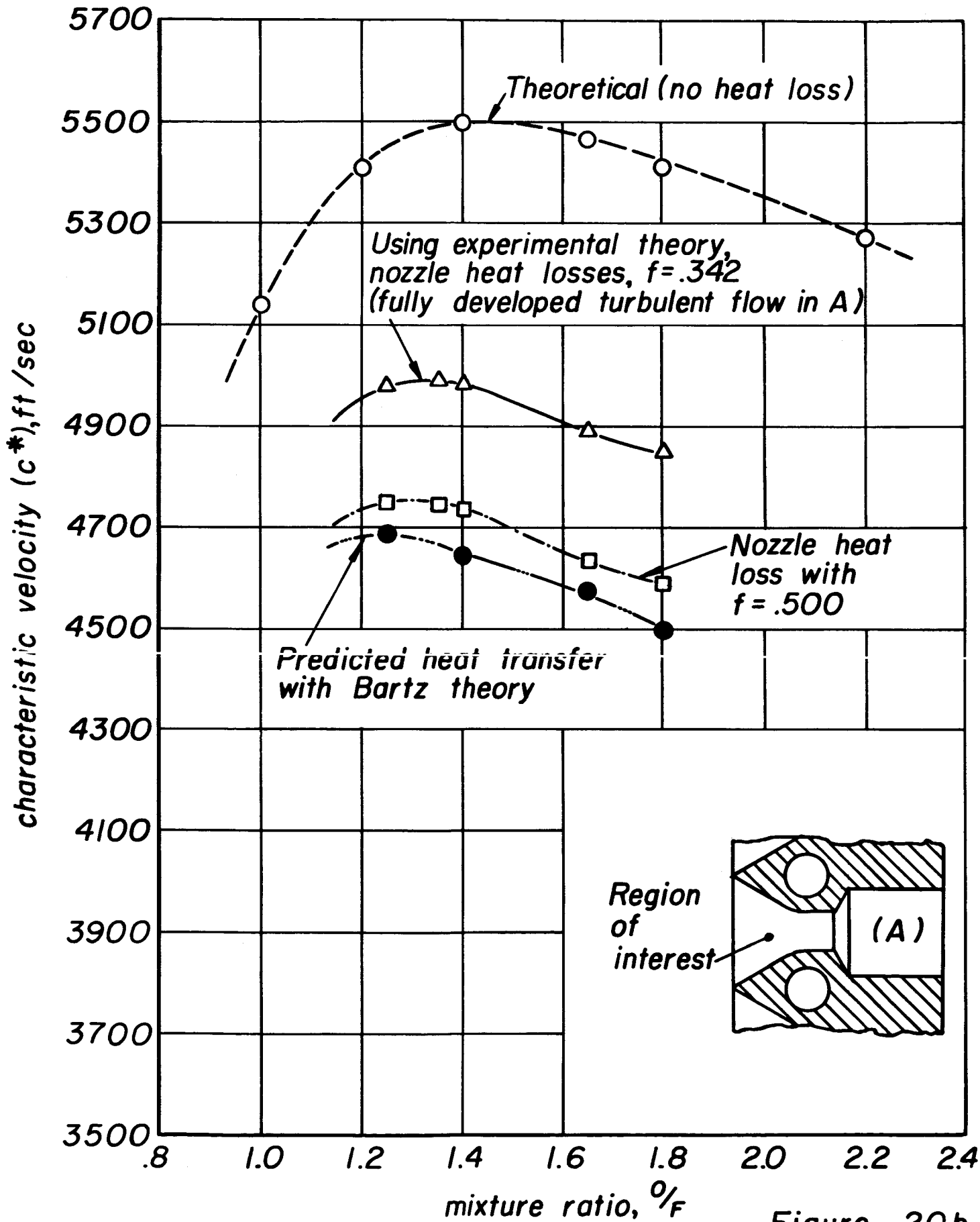
Figure 20b

Combustion parameters determined with the variable-length, with 30° sector motor using the multi-orifice nozzle, injector hole $L/D \approx 20/1$, $P_c = 150$ psia, alcohol-oxygen
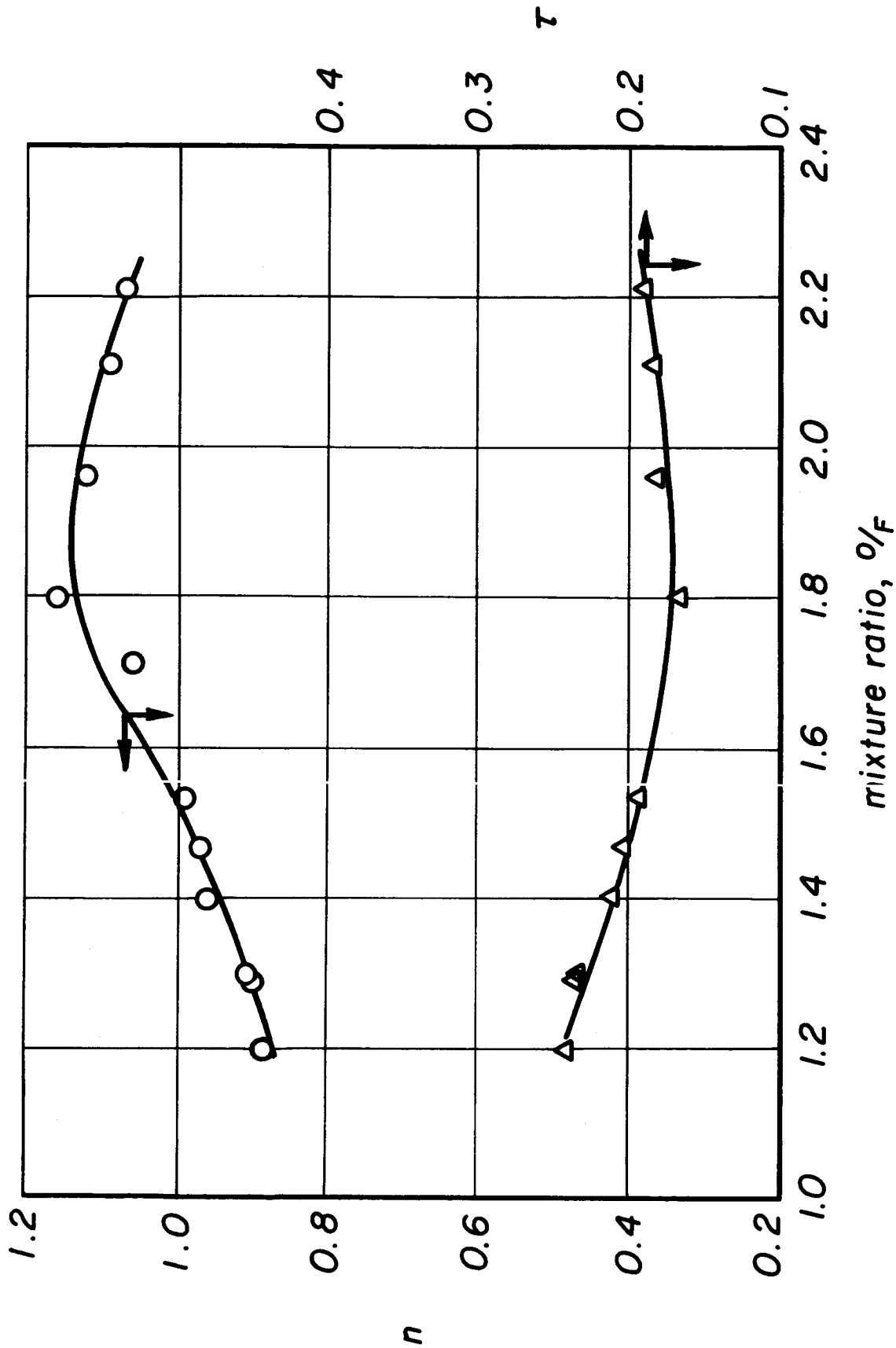
Figure 21

Chamber arrangement for investigating shock pulse effects on stability limits
9-7 tangential, 1.4 $_{design}$ $\bar{r}$, 500 lb. thrust

Shock pulse gun

P

9" Dia. chamber

7" Dia. injection

$1" \times \frac{1}{8}"$ Aluminum destructible baffle

P

P

| start | baffle burnout | shock pulse | shutdown |

Time, sec.
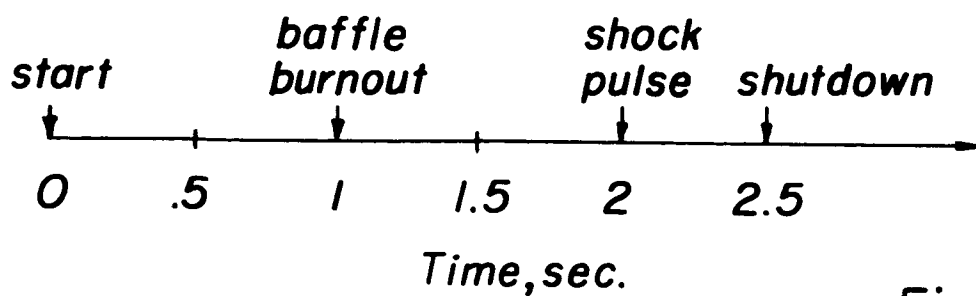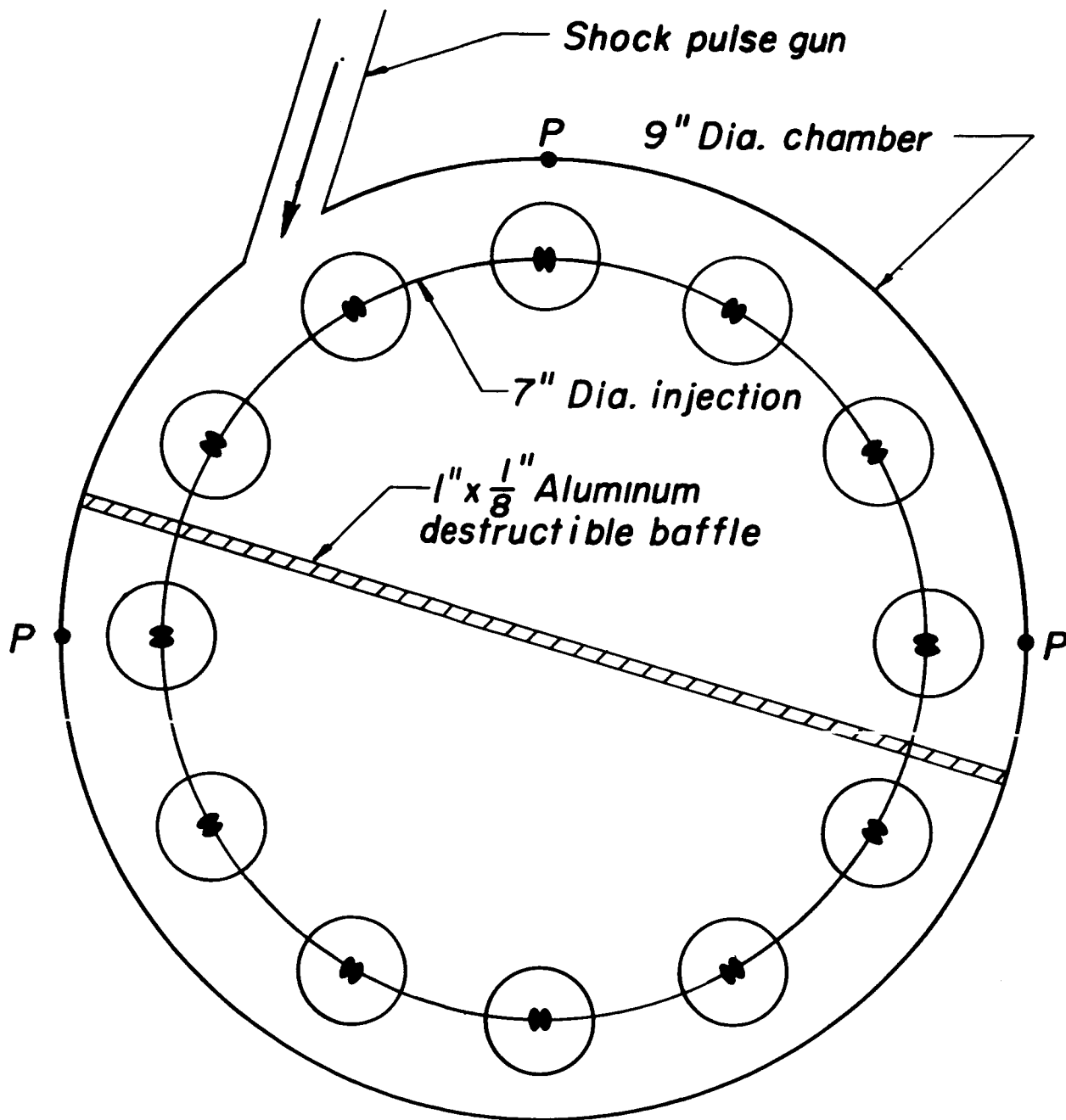
Figure 22

9-7 1.4 Tangential (1x12 Spuds) 500 lbs thrust 150 psi pulsed instability limits tests
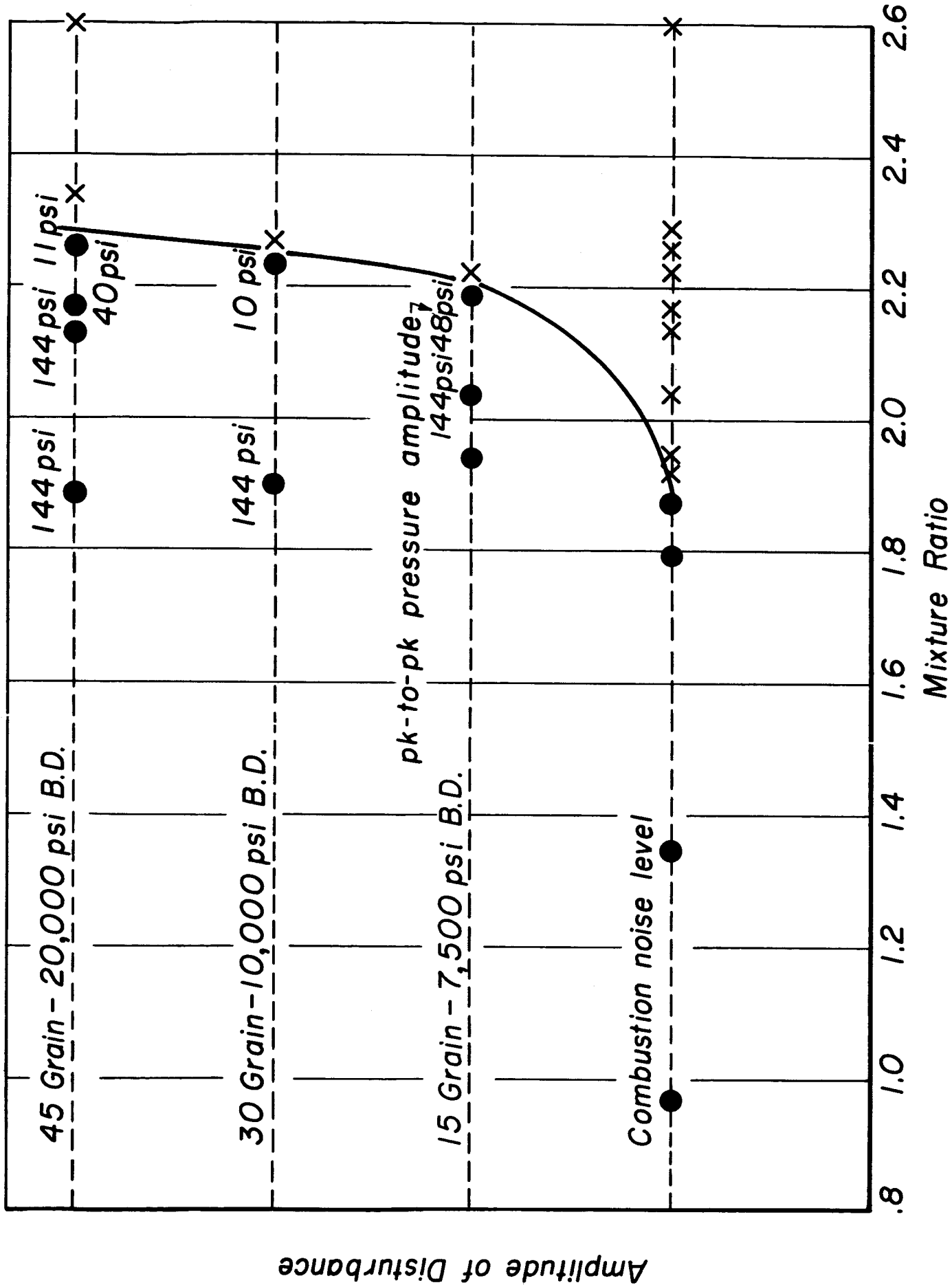
Figure 23

Chamber arrangement for investigating
shock pulse effects on stability limits
9-7 tangential, 1.4 $_{design}$ $\bar{r}$, 1000 lb. thrust

Shock pulse guns

P

7" Dia. injection

$1"$ x $\frac{1}{8}$" Aluminum
destructible baffle
(optional)

P

Inter fan spacing

P

radial spacing

9"Dia. chamber

start

shock
pulse

shutdown

0   .5   1   1.5   2   2.5

Time, sec.
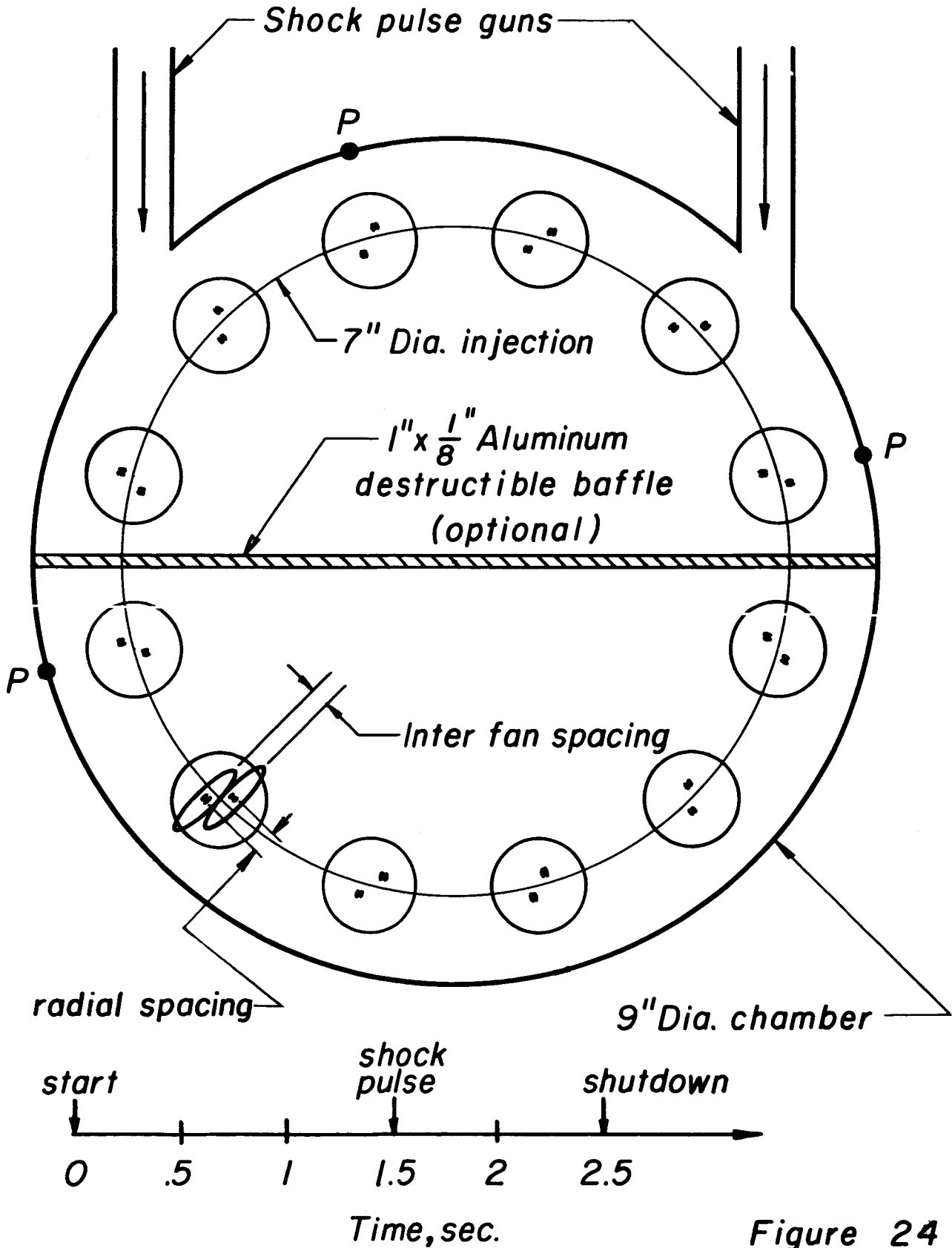
Figure 24

Pulse gun tests ($\bar{O} \rightarrow F$) of like-on-like injector using 9" chamber, 7" injector, 150psia, 1000lb thrust (O on outside)
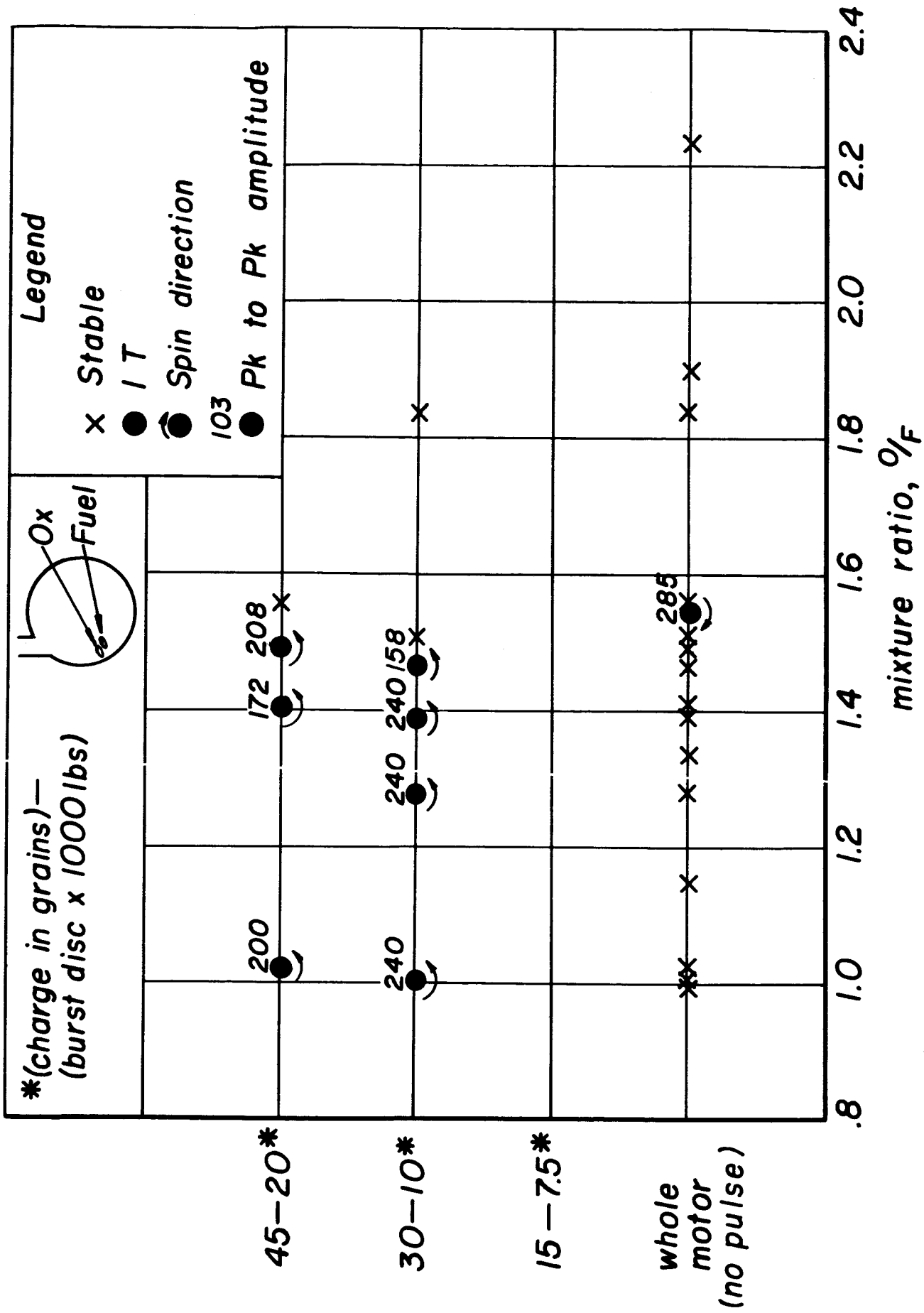
Figure 25

alcohol oxygen 1.4r design, 9"diameter chamber with
7"injection, 150 psia and 1000 lb thrust
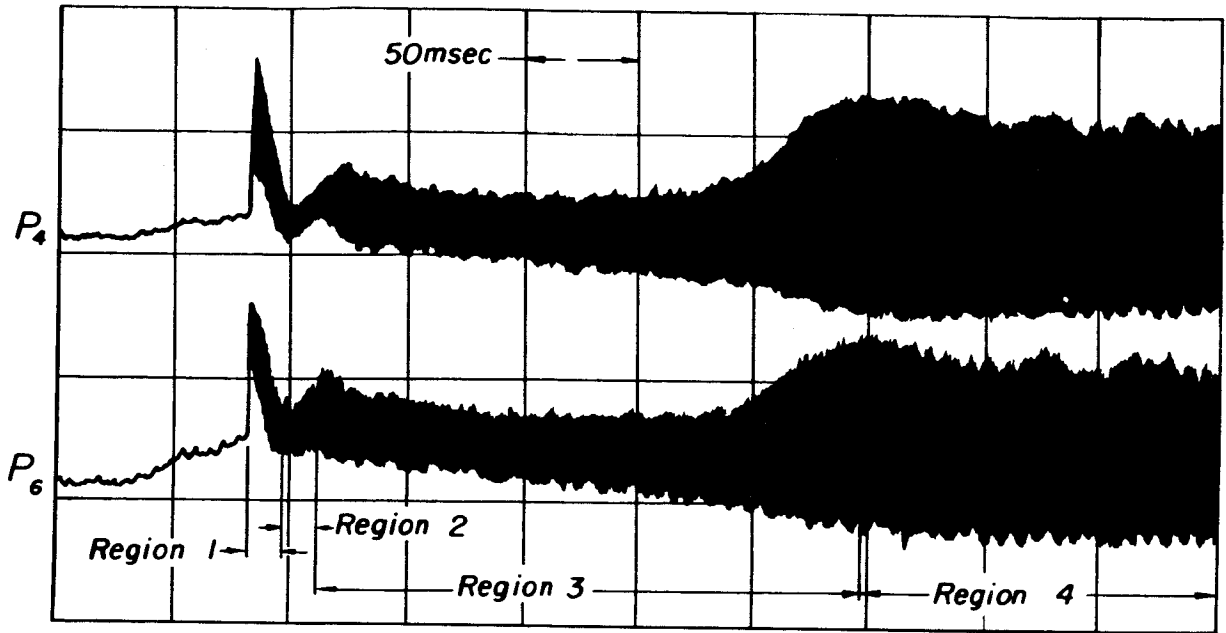
Nonsteady pressure recorded on two pressure transducers
(spaced at 90°)for a fuel to oxidizer oriented pulse
supplied by a 30 grain charge and 10,000 lb burst disc

Region 1-Pulse disturbance, Spinning wave

Region 2 - Standing wave pattern

Region 3-Increasing amplitude, Spinning wave

Region 4-Full amplitude, Spinning wave

Initial wave travel due to pulse

Final wave travel
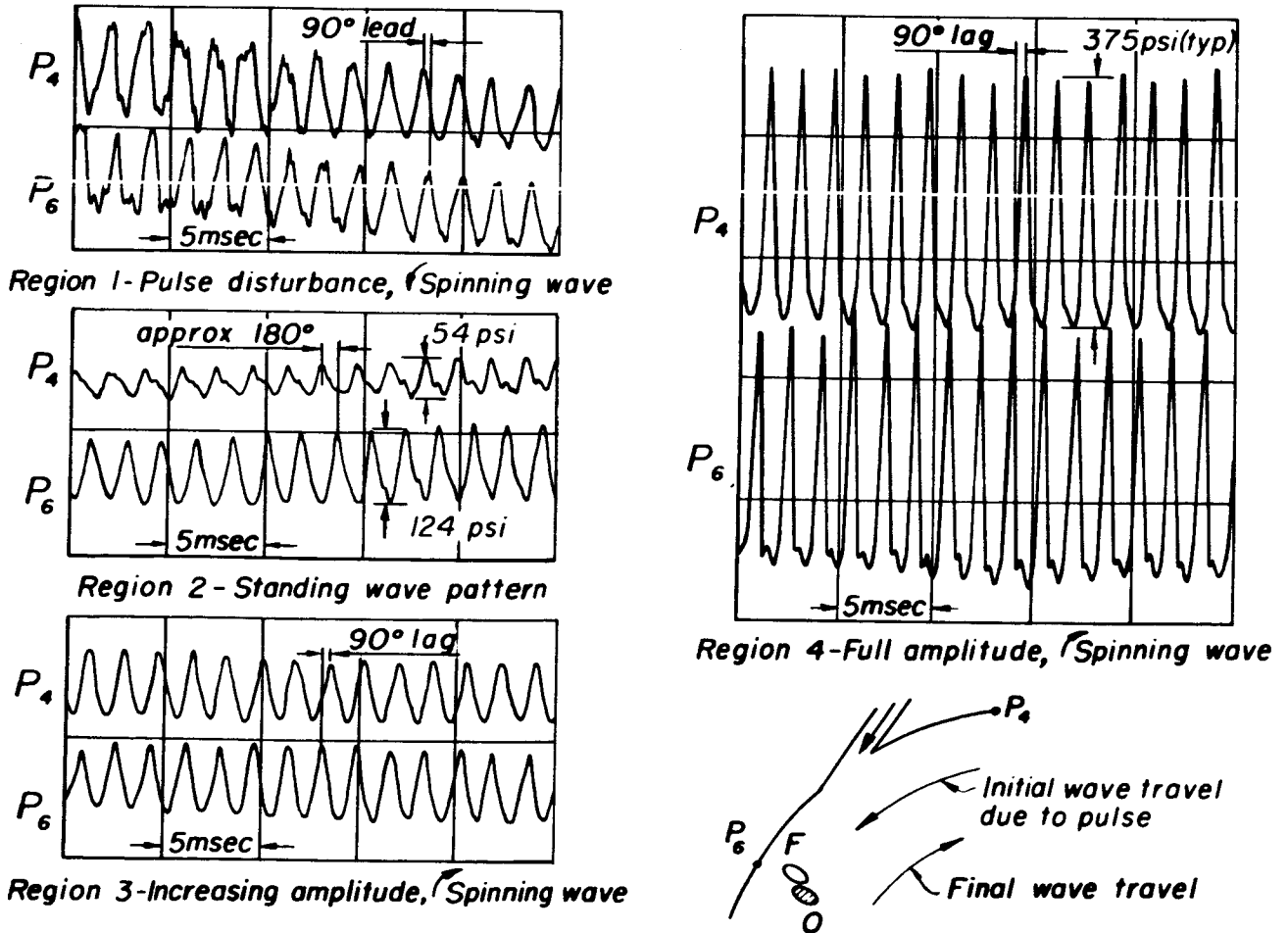
Figure 26

Pulse gun tests ($F \rightarrow O$) of like-on-like injector using 9" chamber,

7" injector, 150 psia, 1000 lb thrust (F on outside)
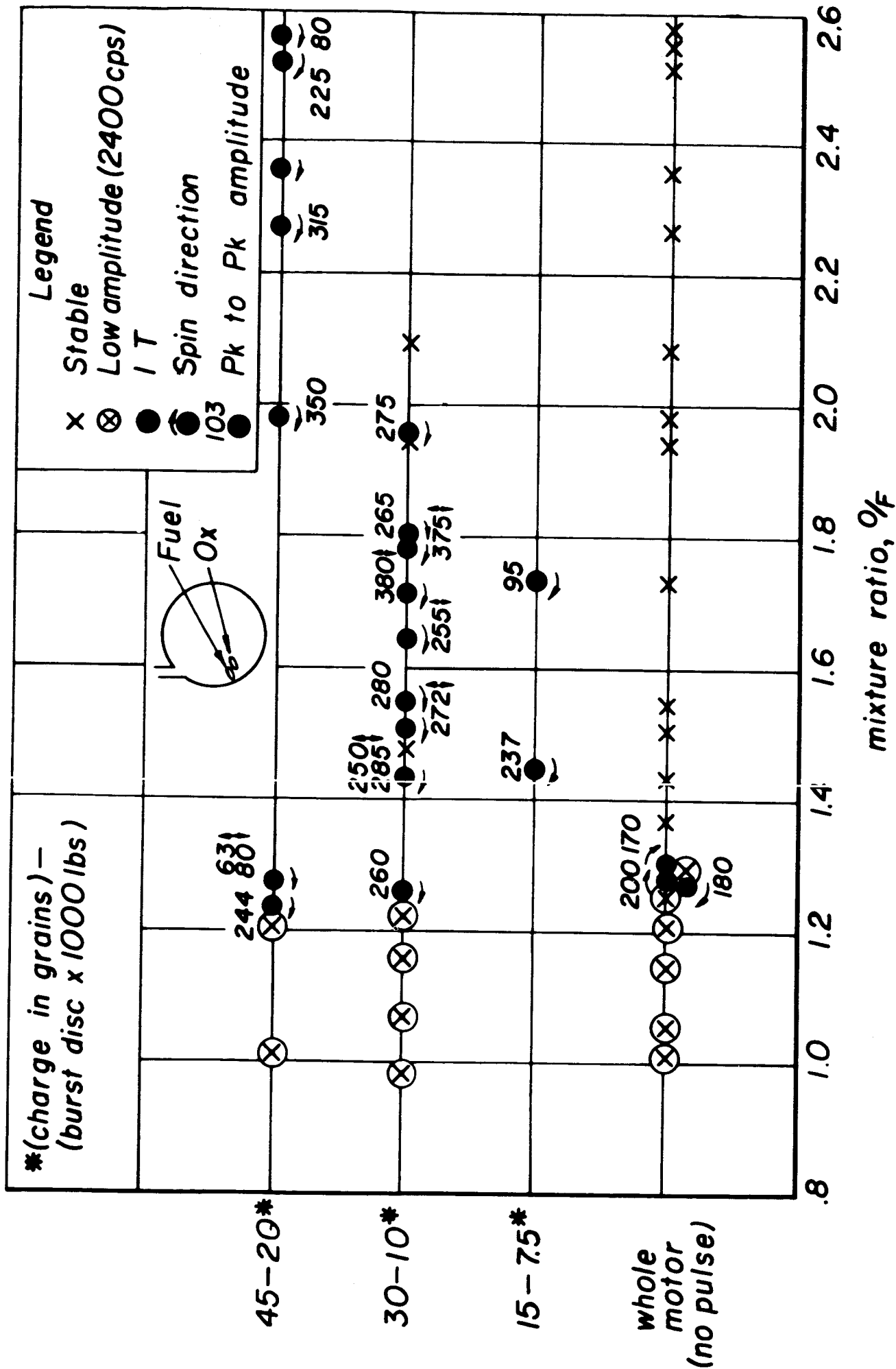
Figure 27

Pressure amplitude versus time for a number
of 30 grain charges using the 10,000 lb burst
discs in the stable, low mixture ratio range (r~.9 to 1.2)

$\widetilde{P}_{ave.} = 230 \, e^{-107t}$

Pressure amplitude, psi peak-to-peak

Time, millisec
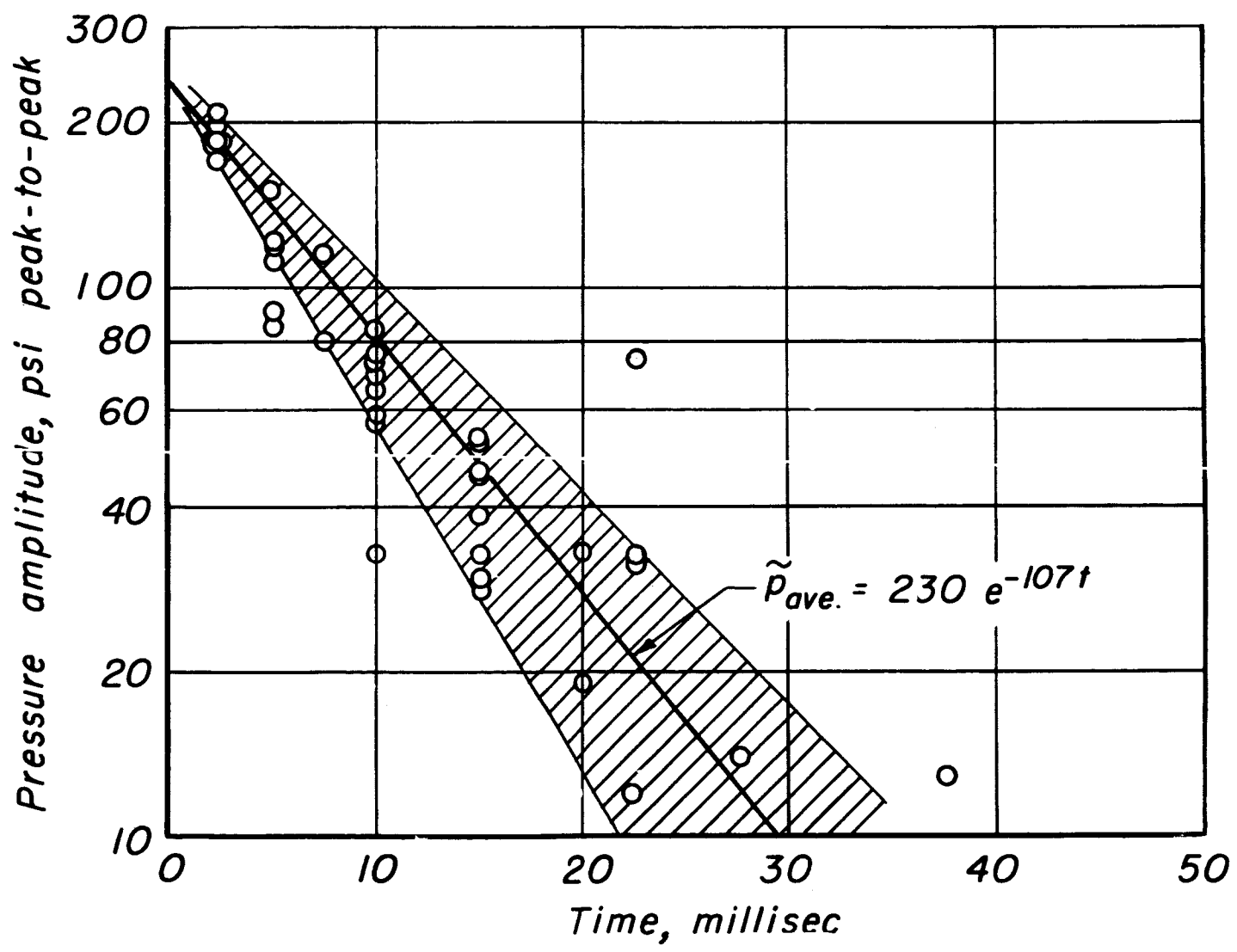
Figure 28

Pressure amplitude versus time for a number
of 30 grain charges using the 10,000 lb burst
discs in the stable, high mixture ratio range (r~2.0)

$$\tilde{p}_{ave.} = 185\, e^{-62t}$$
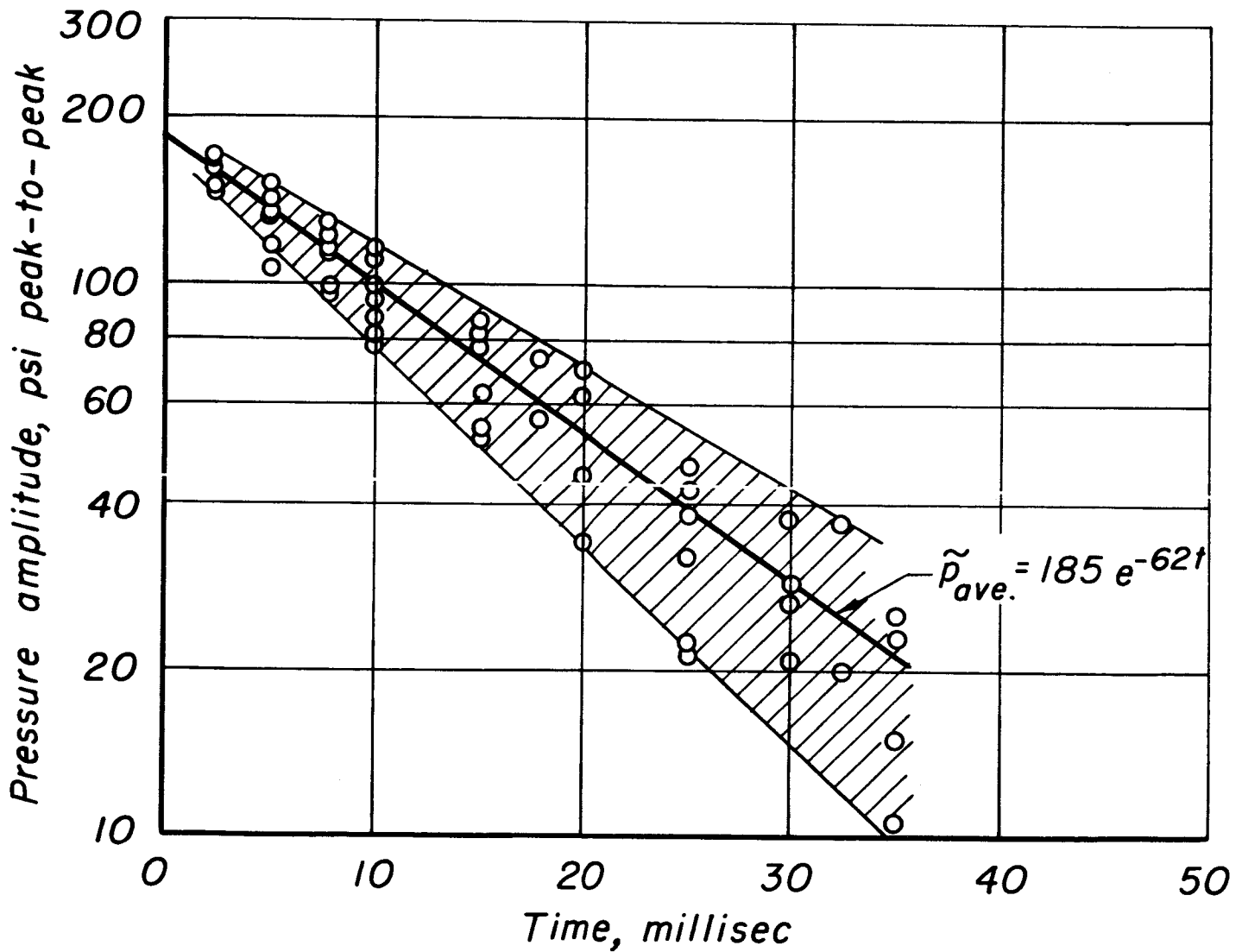
Figure 29

Four shock pulse arrangements
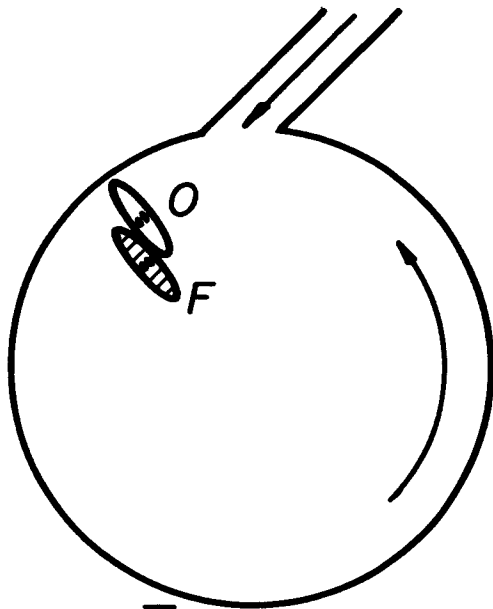
$\overline{O} \longrightarrow F$

Pulse: ox-to-fuel
oxidizer outside
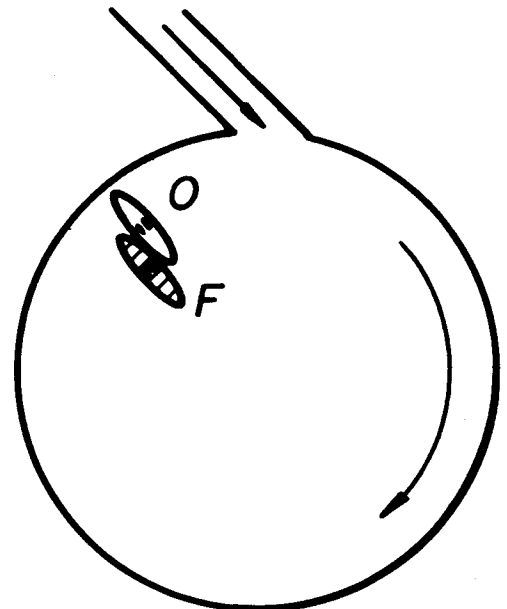
$F \longrightarrow \overline{O}$

Pulse: fuel-to-ox
oxidizer outside
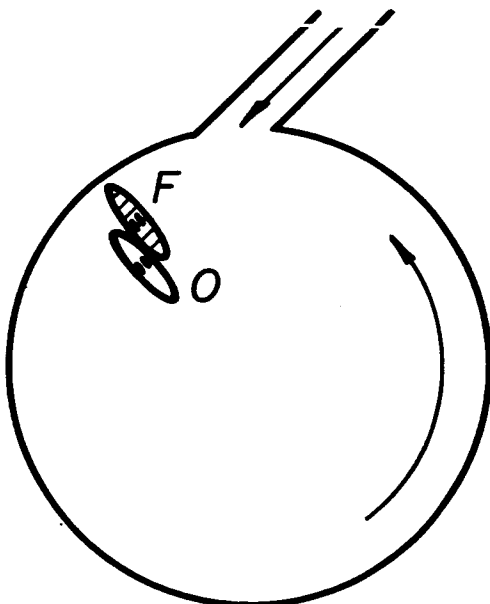
$\overline{F} \longrightarrow O$

Pulse: fuel-to-ox
fuel outside
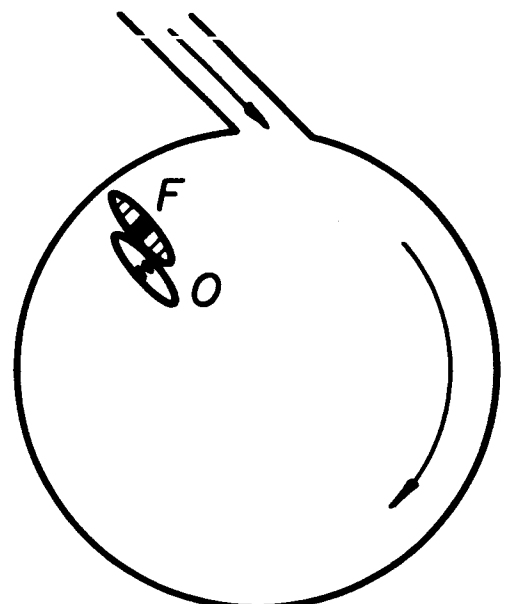
$O \longrightarrow \overline{F}$

Pulse: ox-to-fuel
fuel outside

Figure 30

Effect of combustion on initial oscillating pressure amplitudes
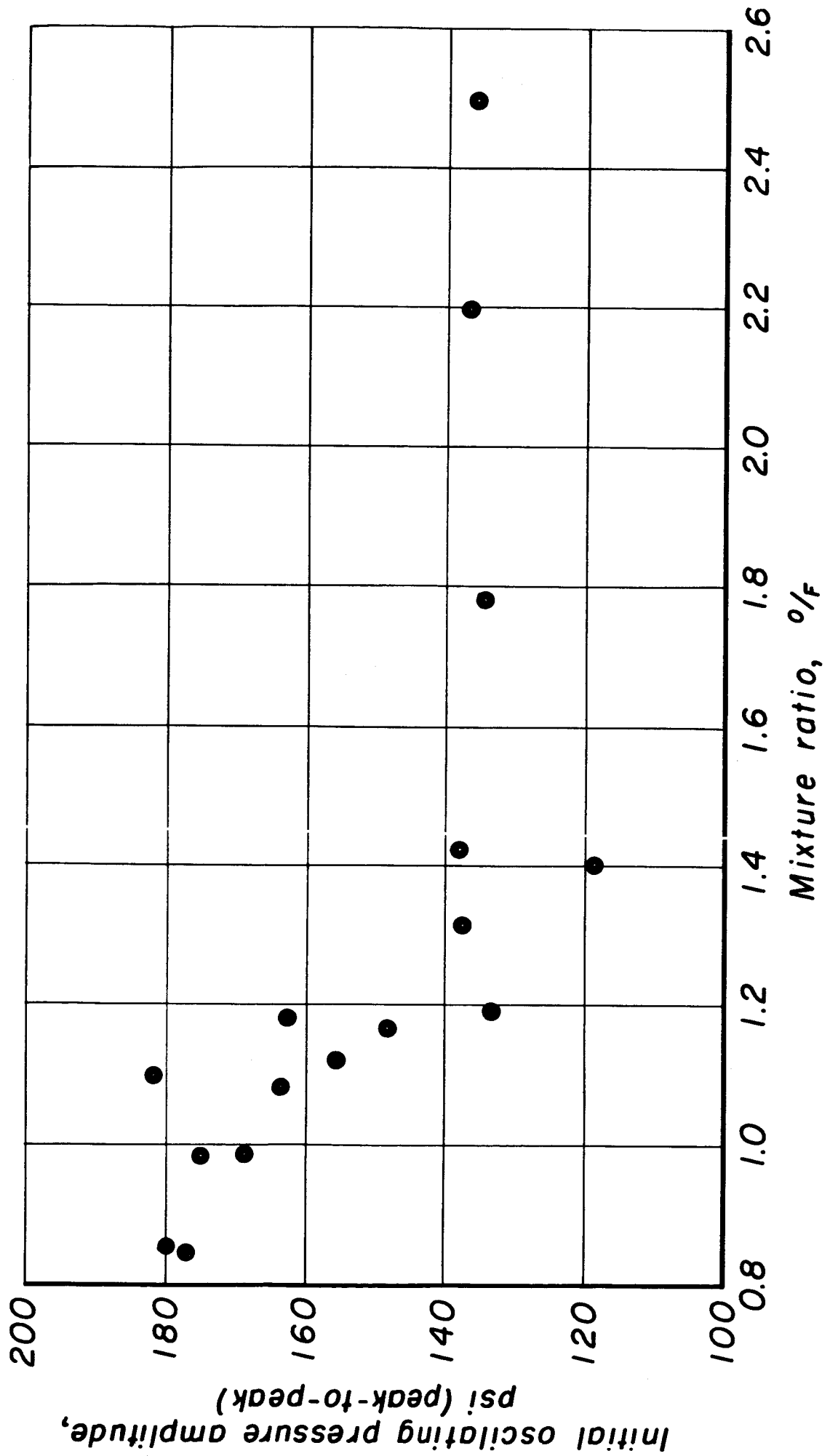
Figure 31

Pulsed instability limits tests
0.2" like-on-like, $O \rightarrow \overline{F}$, alcohol-oxygen, 9-7 chamber,
150 psia, 1000 lb thrust
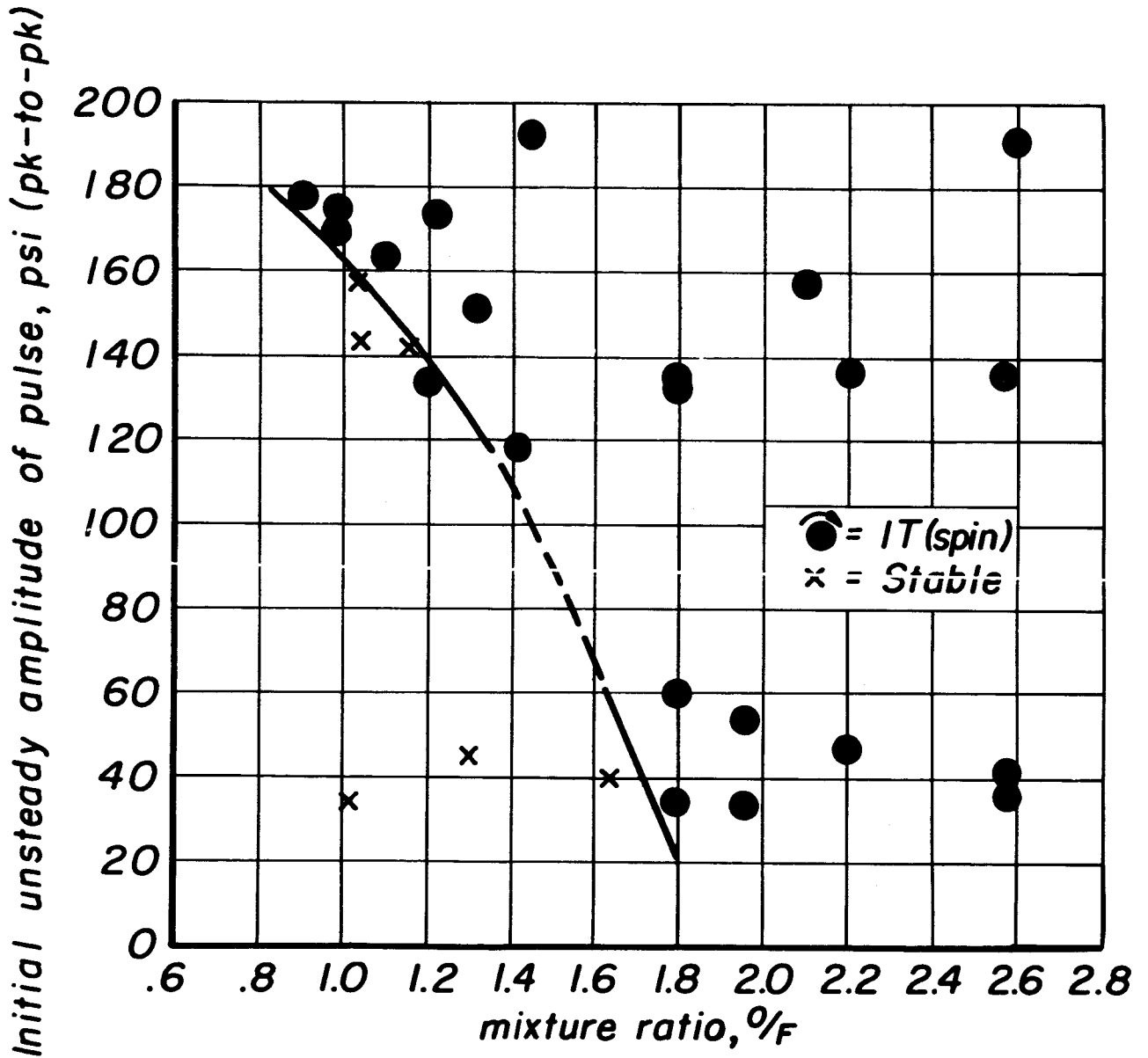
Figure 32

Pulsed instability limits tests
0.2" like-on-like, $\overline{O} \rightarrow F$, alcohol-oxygen, 9-7 chamber,
150 psia, 1000 lb thrust
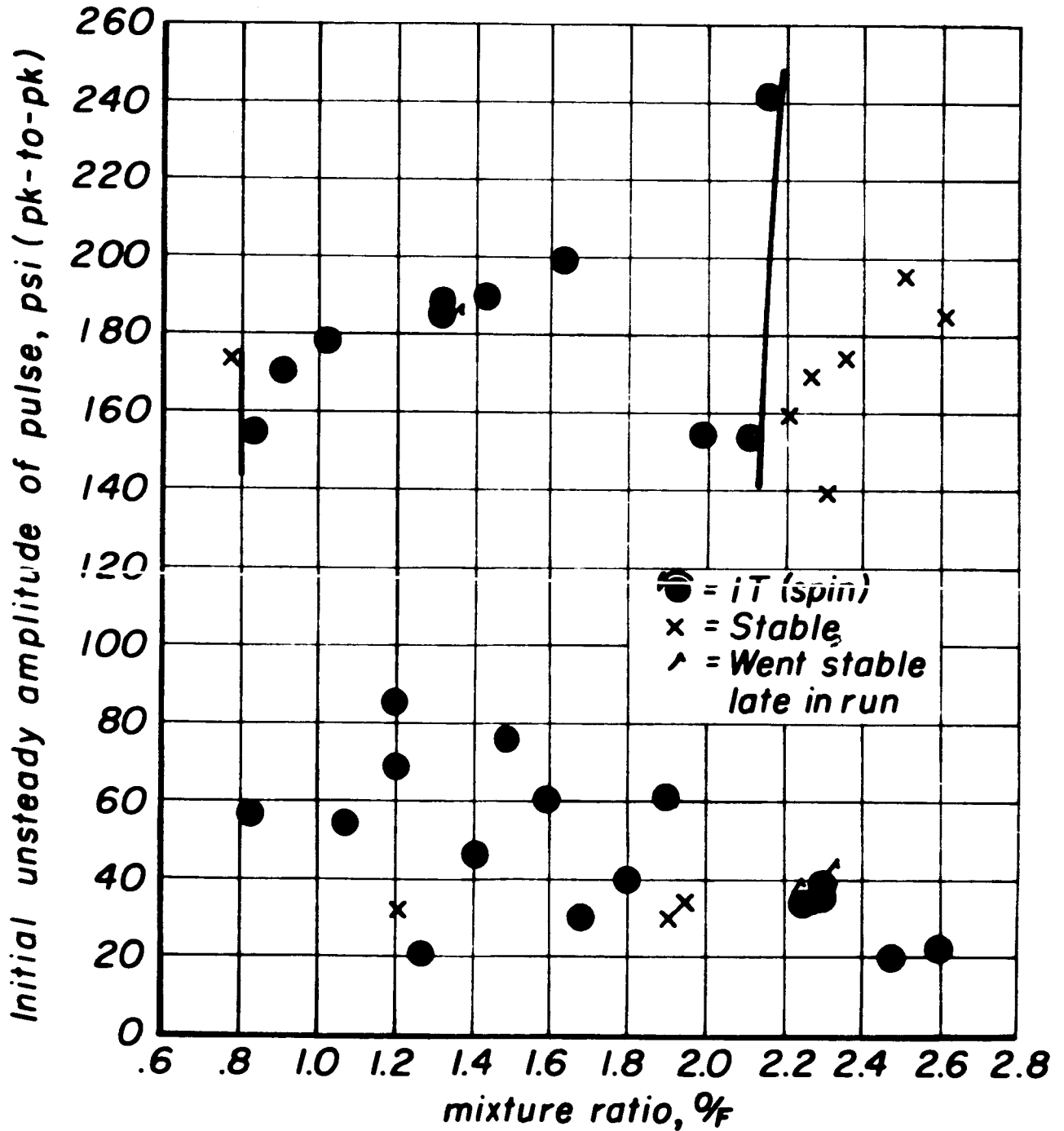
Figure 33

Pulsed instability limits tests
0.2" like-on-like, F→Ō, alcohol-oxygen, 9-7 chamber, 150 psia, 1000 lb thrust
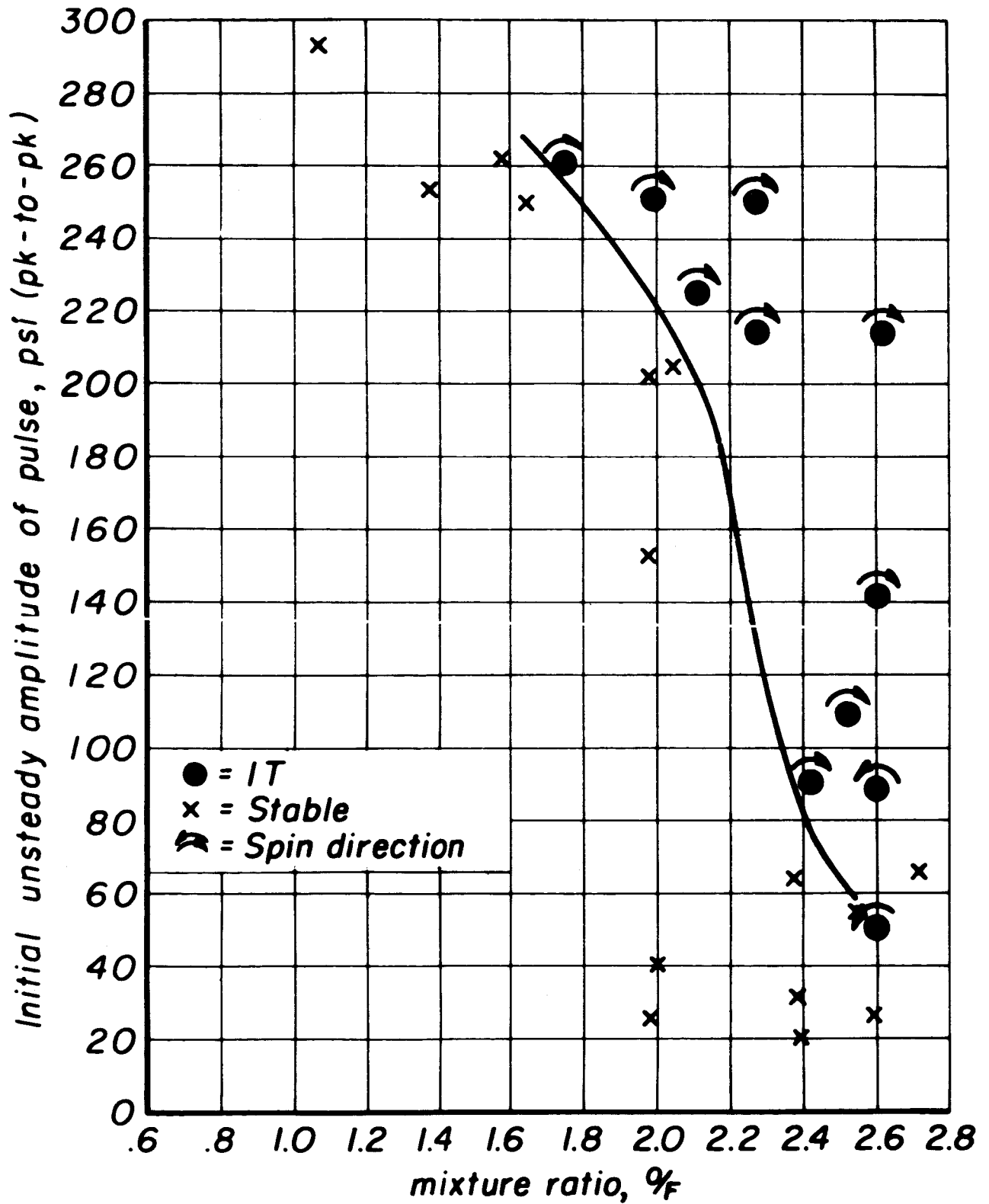
Figure 34
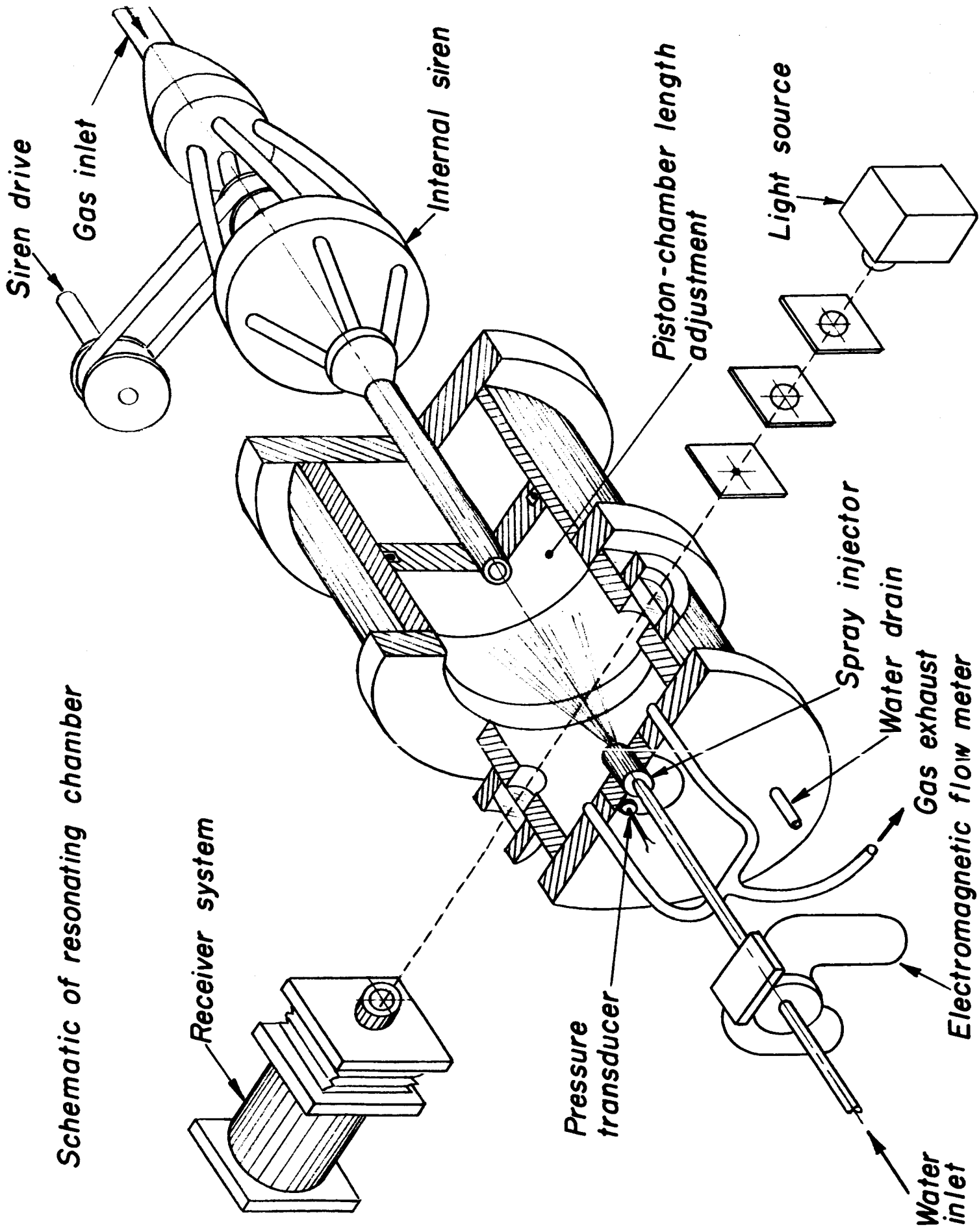
Schematic of resonating chamber

Siren drive

Gas inlet

Internal siren

Piston-chamber length adjustment

Light source

Receiver system

Spray injector

Water drain

Gas exhaust

Pressure transducer

Electromagnetic flow meter

Water inlet

Figure 35

Resonance characteristics for various chamber lengths in the "Resonating Chamber"
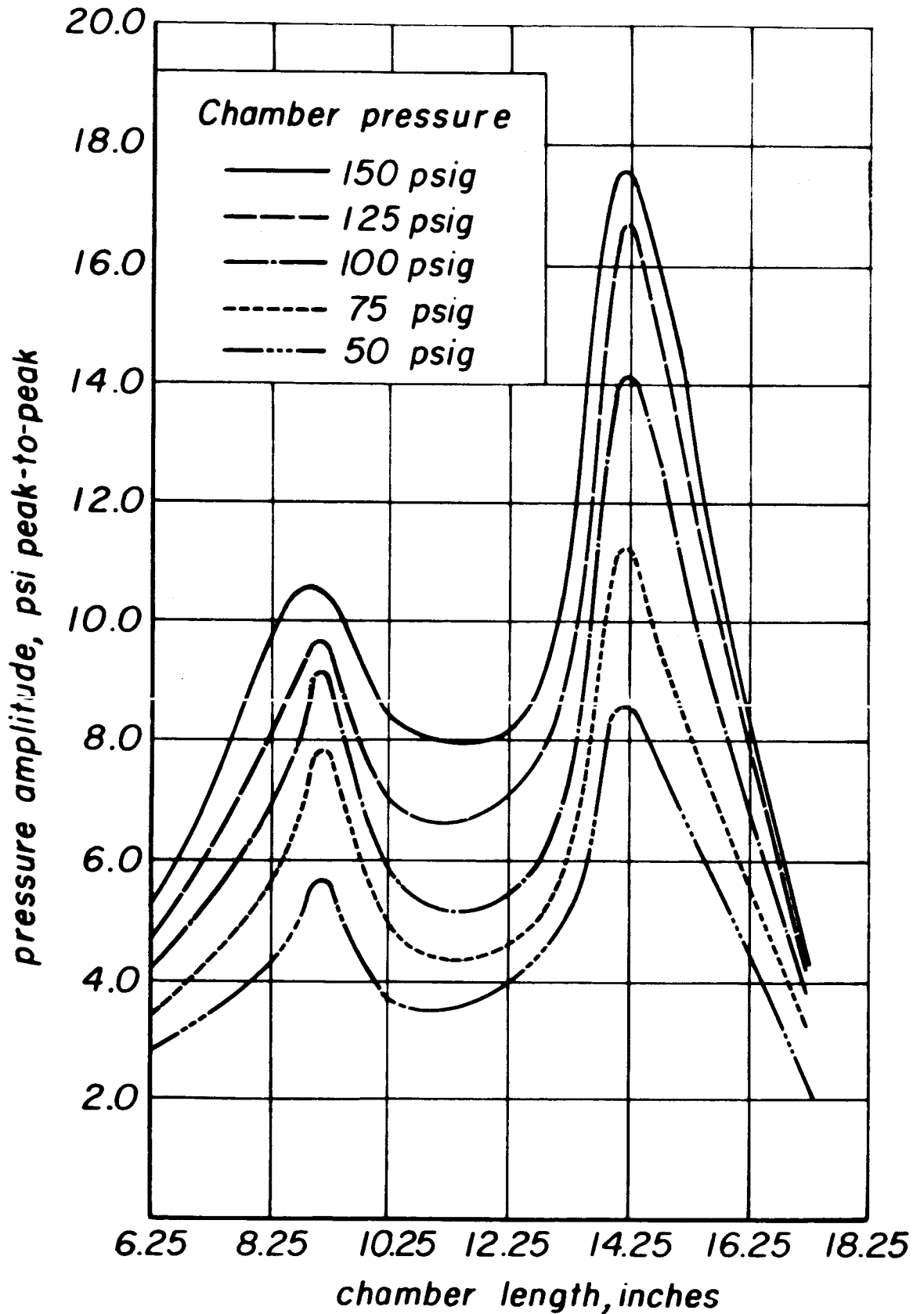
Figure 36

Experimental schematic for vaporization and propellant displacement study

Pressure gauge

Temperature controlled pressurize container for working fluid

Line pressure gauge

Thermometer

Straightening vanes

Electrical horn driver

Velocity probe

Exhaust

Inlet gas supply

Porous material

Screen to induce controlled turbulence

Pressure pickup

Optical glass front and rear for schlieren system
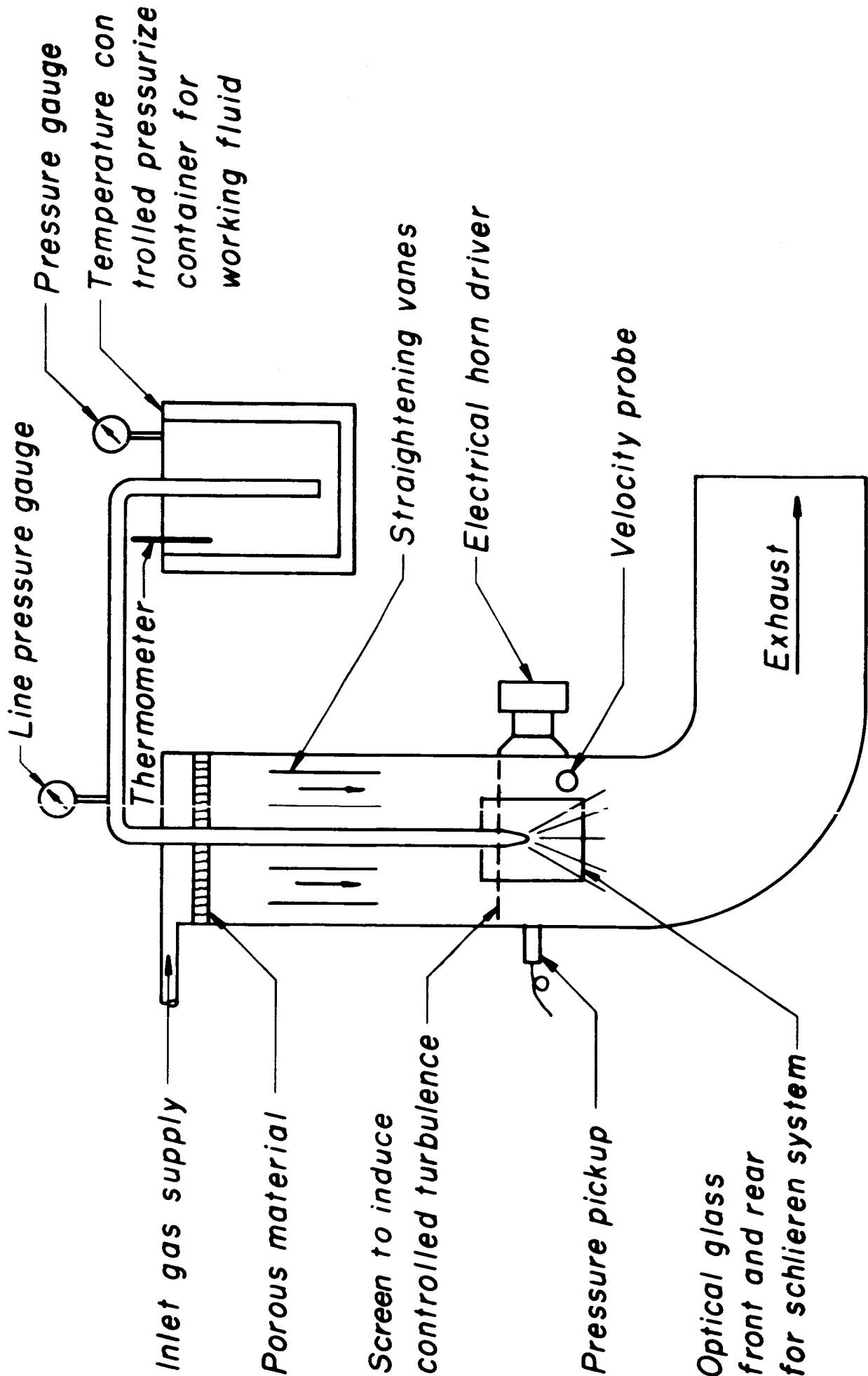
Figure 37

Velocity distribution from c* data 9-1.4 T, 30° sector fuel-on-oxidizer, $L/D \approx 20/1$, $\bar{U}_e = 0.05$
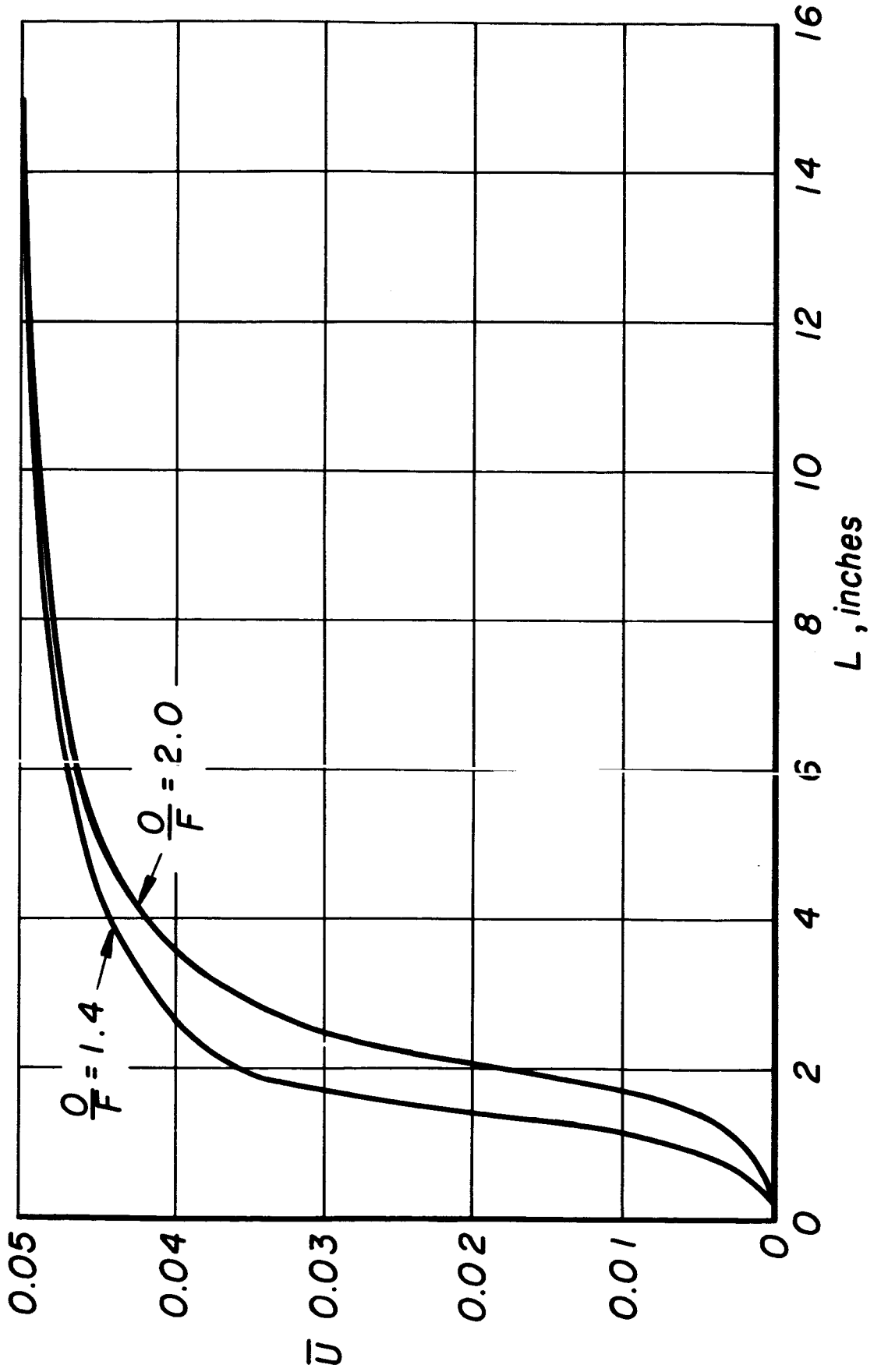
Figure 38

Error in minimum interaction index vs chamber length for two velocity profiles

Figure 39

Microswitch to sequence timer

Radial pulse

Camera

Drum camera

Alternate system

Multiple spark

Pulsegun

Tangential pulse

Spark

Pressure instrumentation

Velocity probes

Optical ground injector plate

Knife edge

Optical glass plate

Spherical mirror
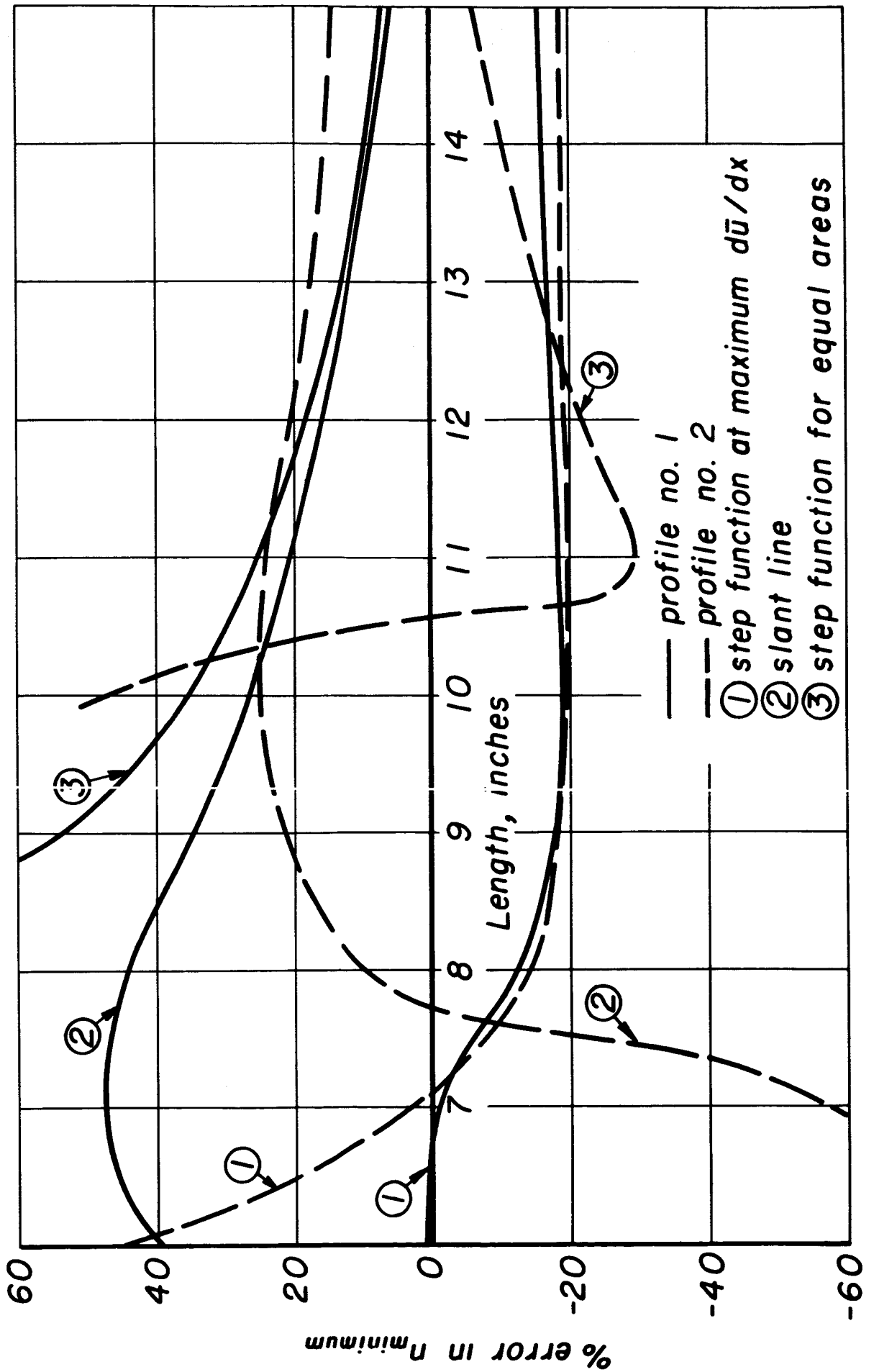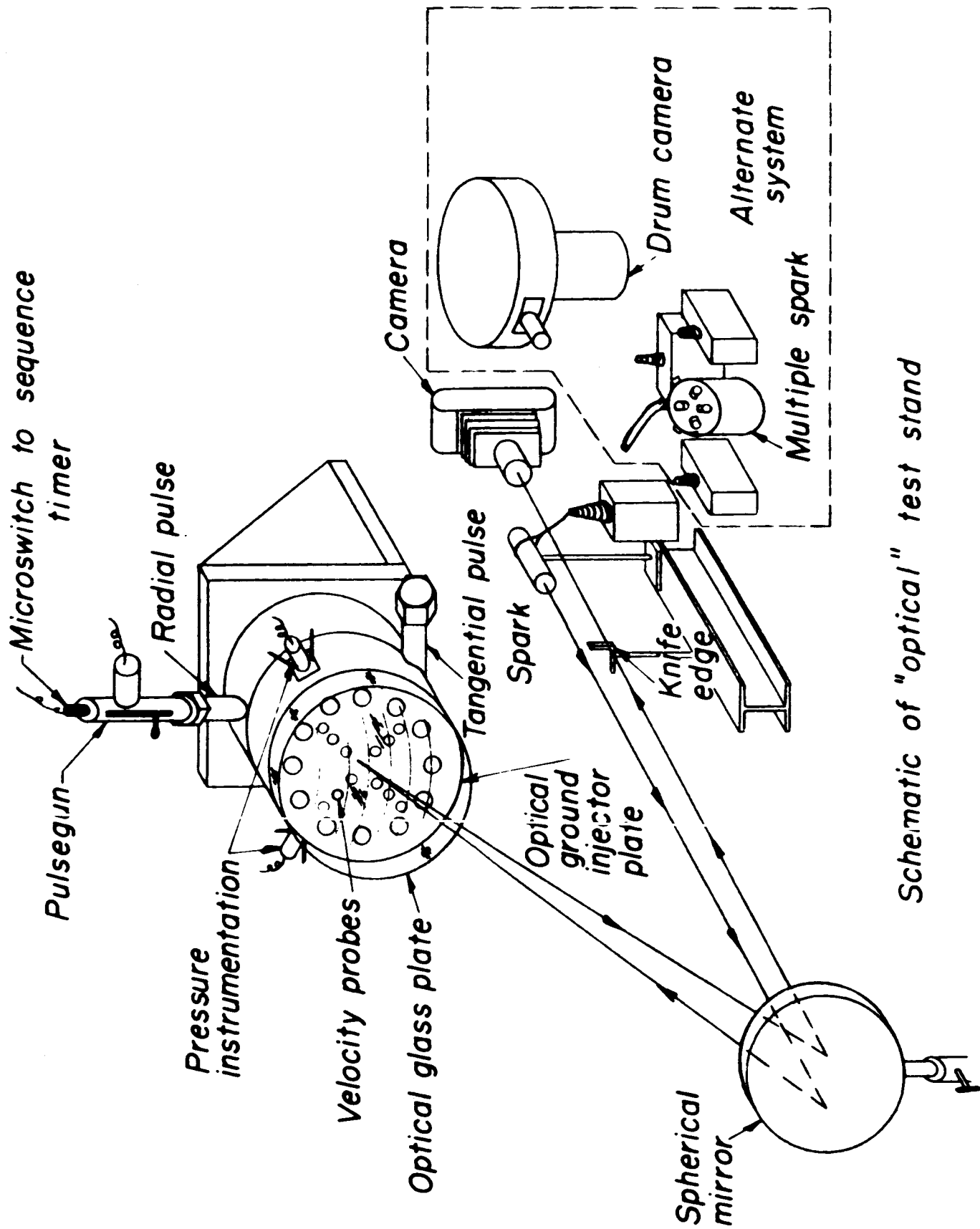
Schematic of "optical" test stand

Figure 40
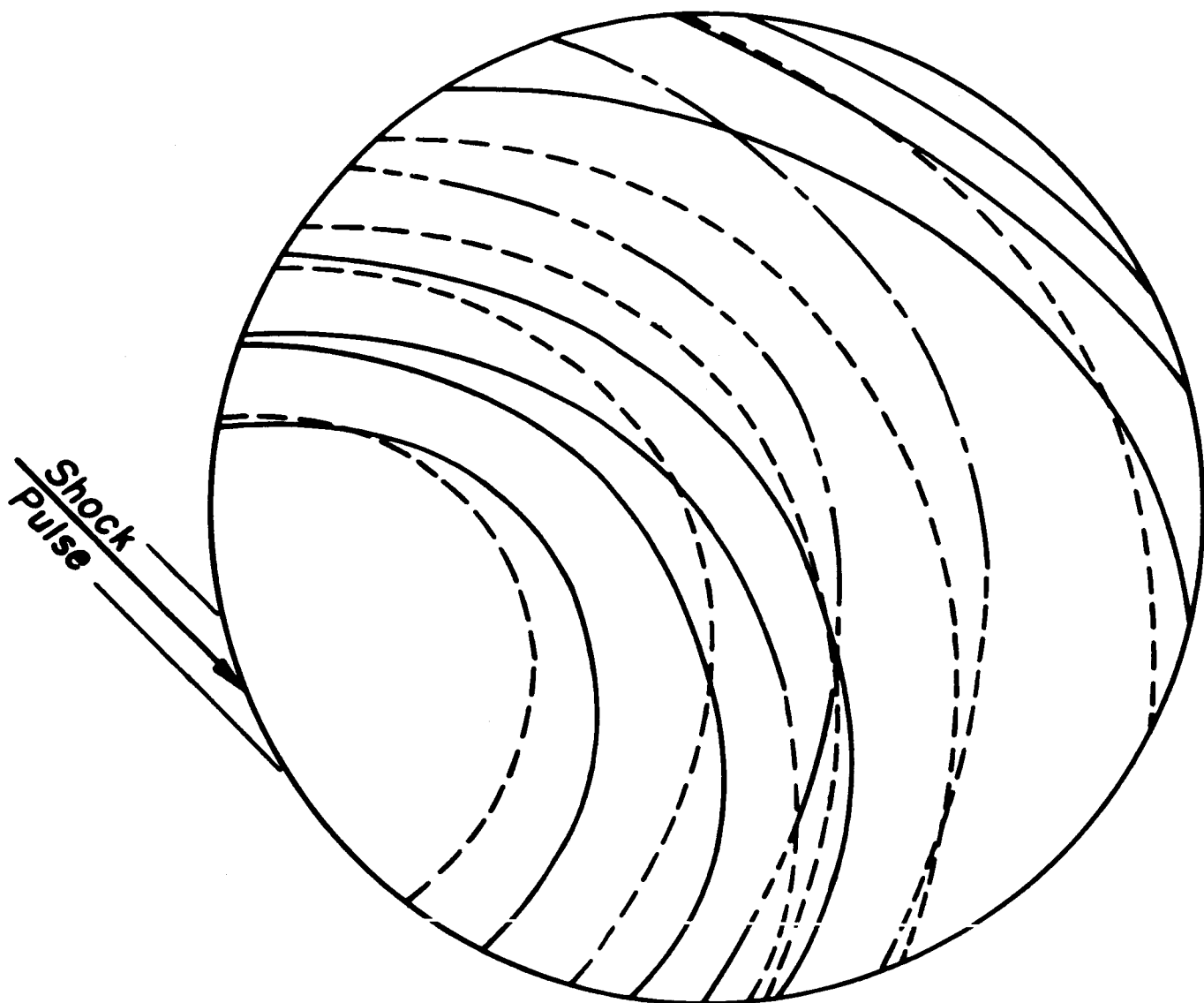
Shock pulse travel across the injector face
for various chamber pressures

Figure 41

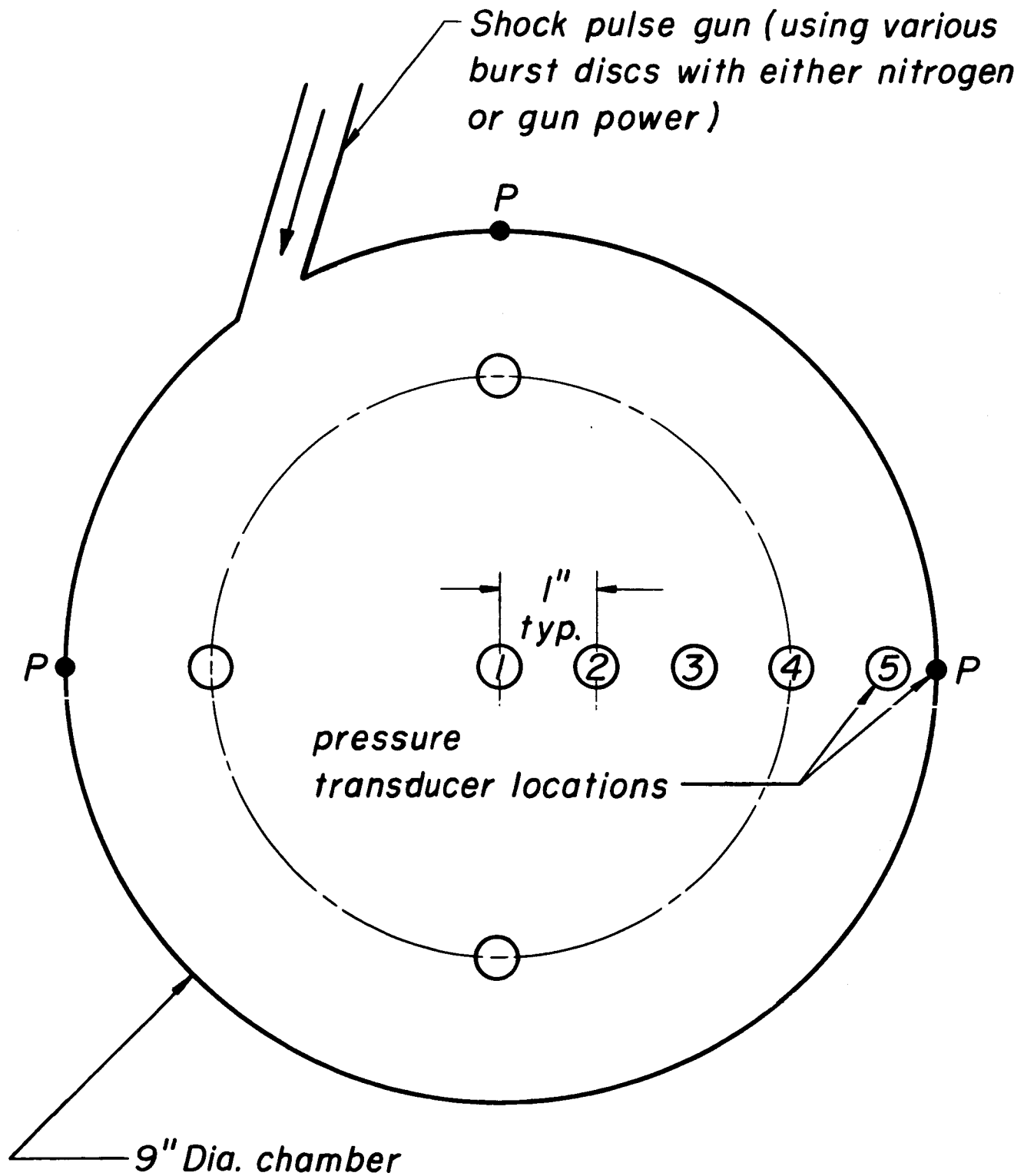Chamber arrangement for evaluating
shock pulse effects without combustion

Shock pulse gun (using various burst discs with either nitrogen or gun power)

P

1" typ.

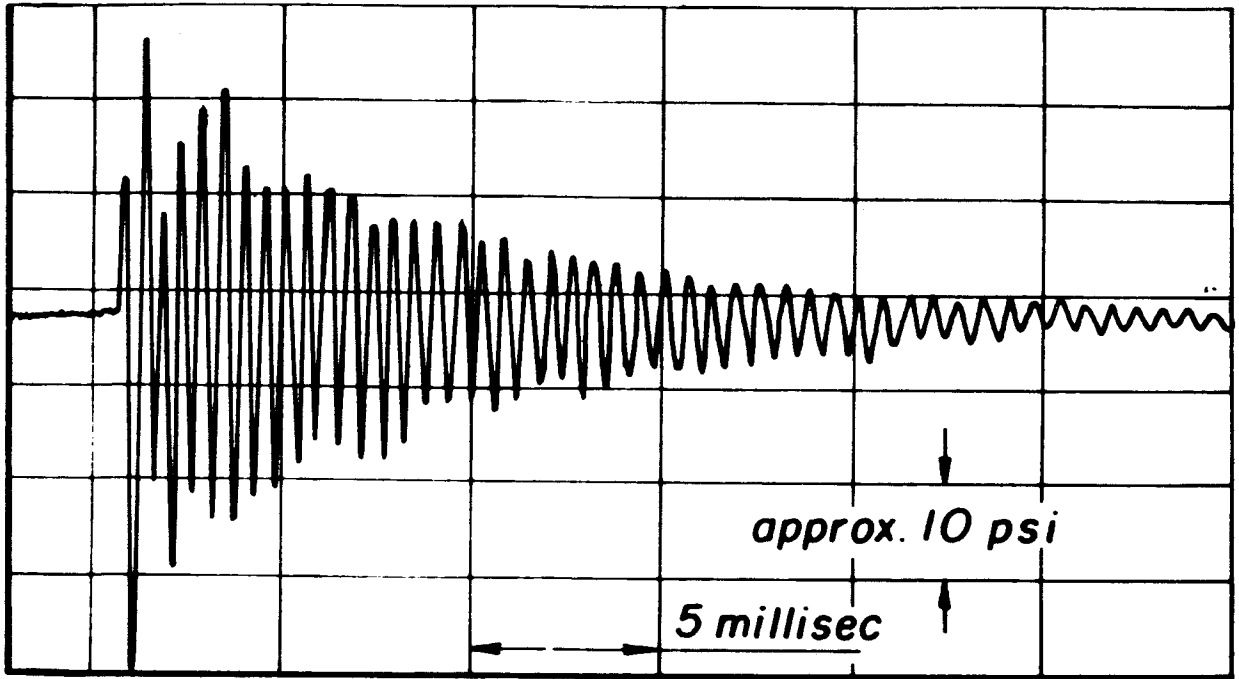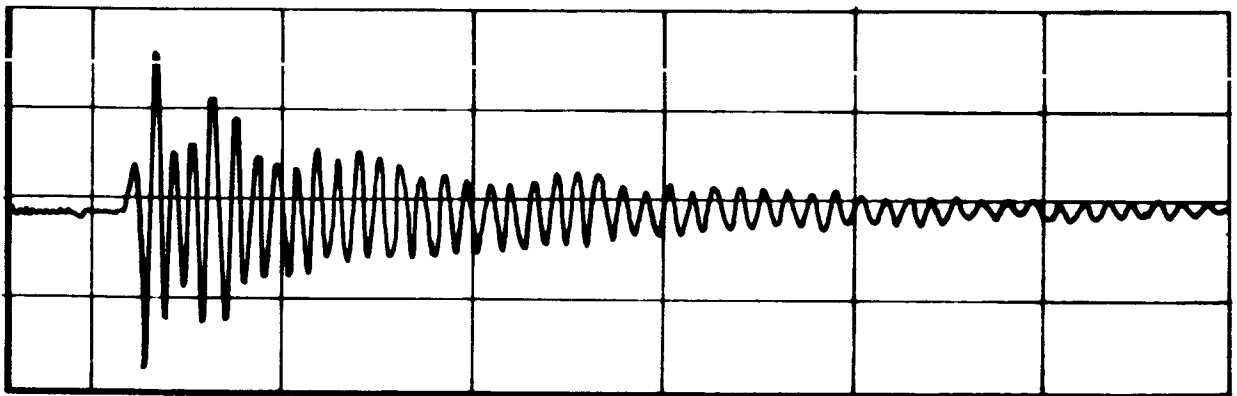P

① ② ③ ④ ⑤

P
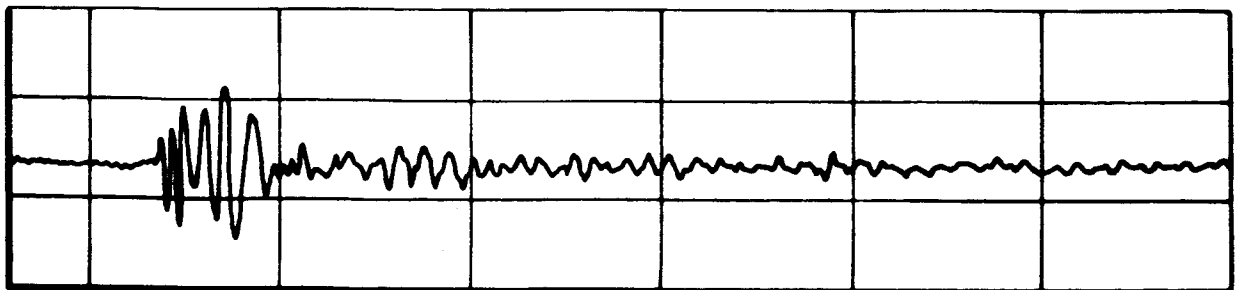
pressure transducer locations

9" Dia. chamber

Figure 42

Oscillating pressure amplitude versus time at various locations on the injector face. Pulse due to 30-10 combination in a 9" diameter chamber

approx. 10 psi

5 millisec

Station 5 (4 inches from center)

Station 3 (2 inches from center)

Station 1 (center of injector face)

Figure 43

Distribution of the unsteady component of pressure 30 millisec. after pulse firing (30 gr - 10 K), axisymmetric
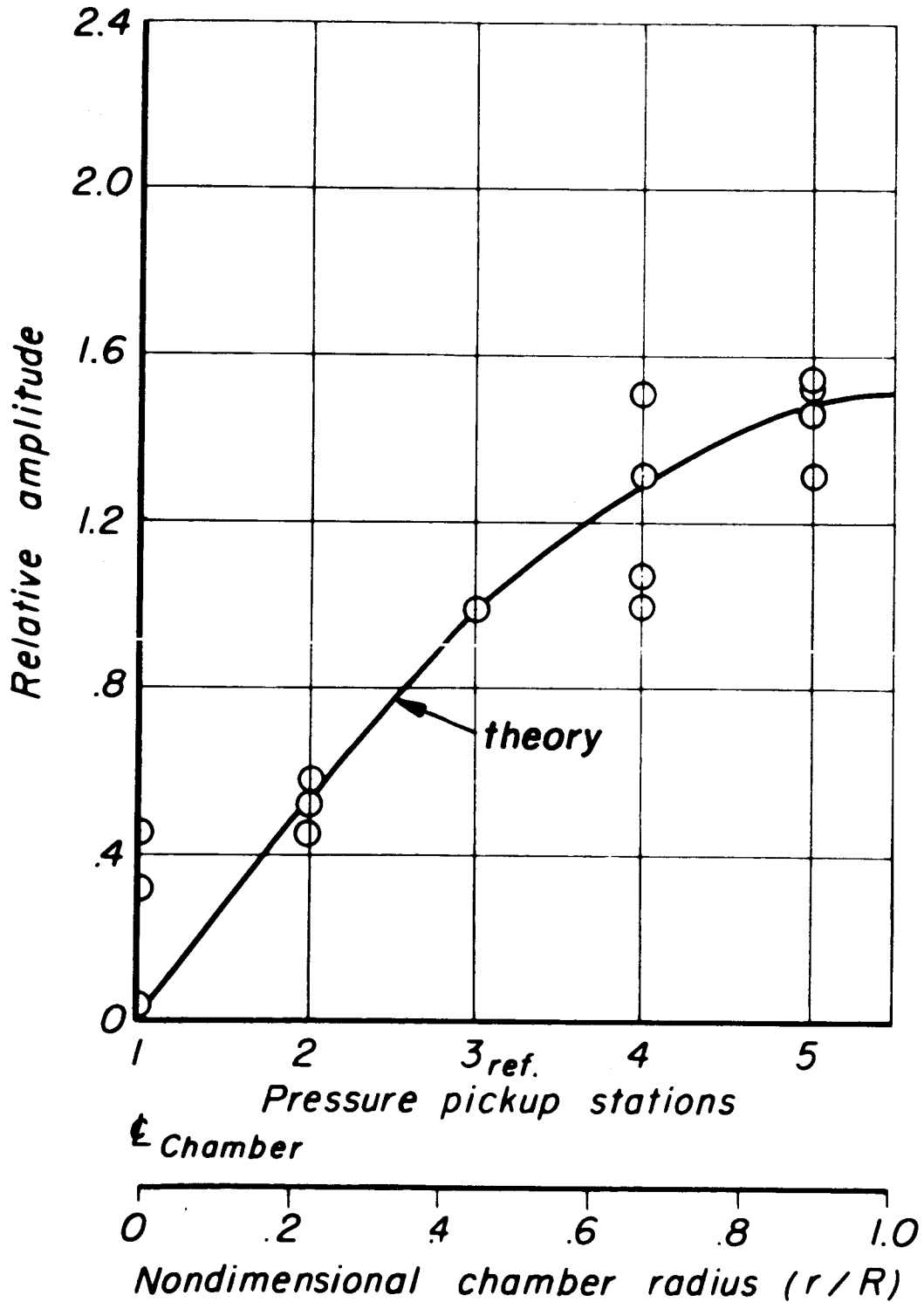
Figure 44

Peak-to-peak pressure amplitude time history for various grain charges and burst disc combinations in a nitrogen filled chamber at one atmosphere

A. 15 grain charge, 7,500 psi burst diaphragm
B. 30 grain charge, 10,000 psi burst diaphragm
C. 45 grain charge, 20,000 psi burst diaphragm

$P' = 74e^{-124t}$
$f = 2000 cps$

$P' = 40e^{-87t}$
$f = 1400 cps$

$P' = 53e^{-104t}$
$f = 1700 cps$

9"Dia.
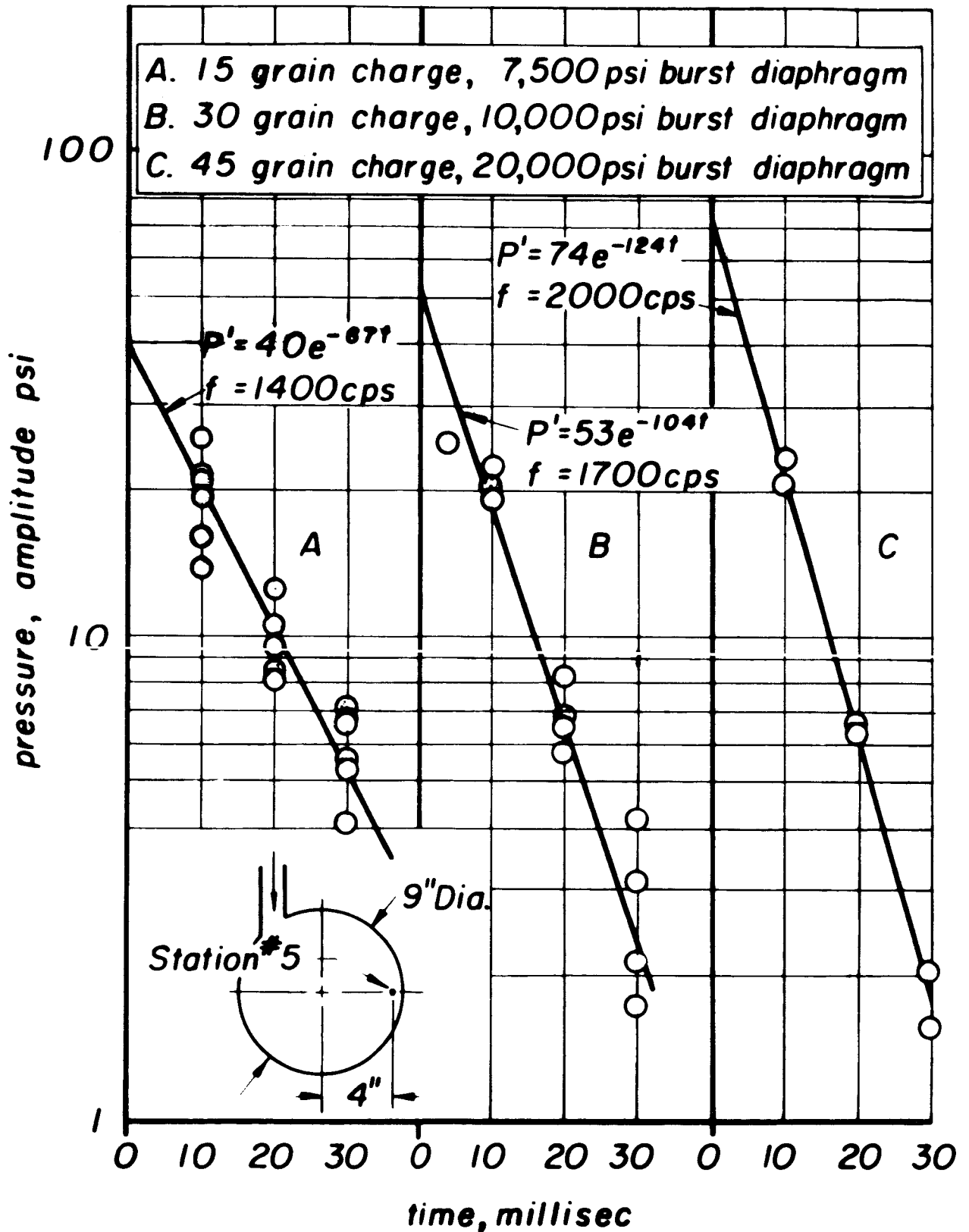Station #5
4"

pressure, amplitude psi

time, millisec

Figure 45a

Effect of chamber pressure on amplitude and
duration of pulses for 30 grain charges and
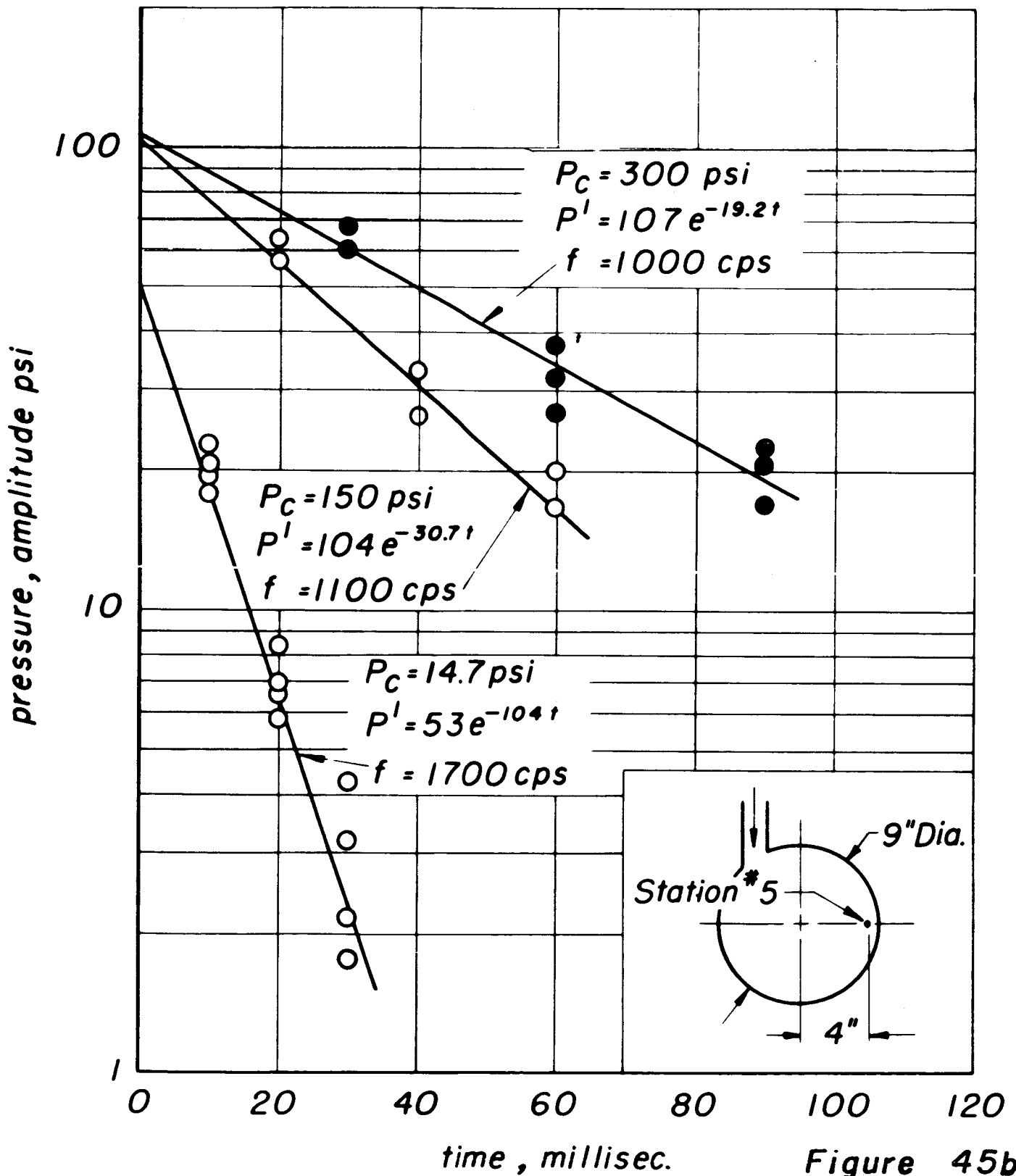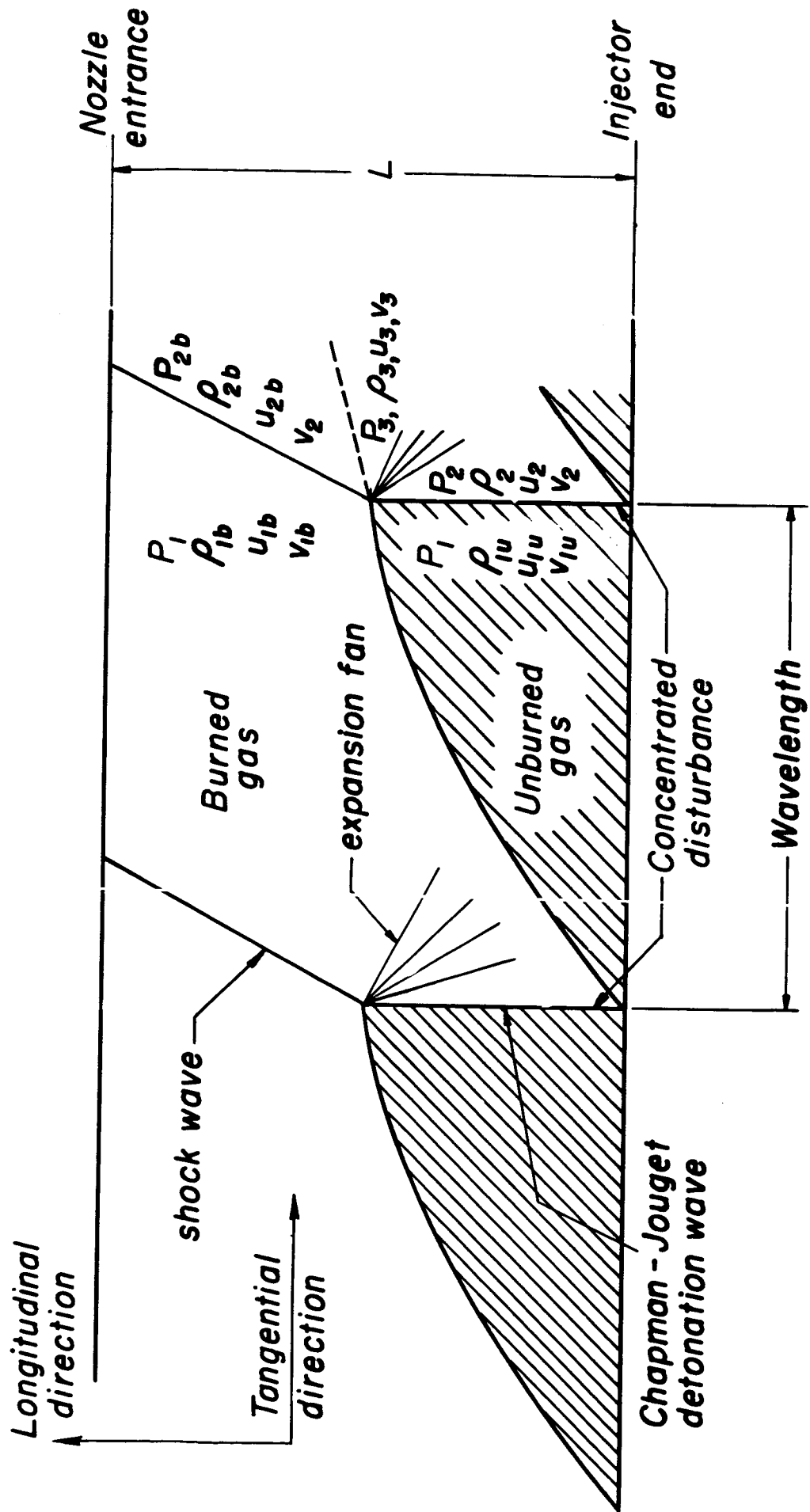10,000 psi burst discs in a nitrogen
filled chamber

$P_C = 300$ psi
$P^I = 107 e^{-19.2t}$
$f = 1000$ cps

$P_C = 150$ psi
$P^I = 104 e^{-30.7t}$
$f = 1100$ cps

$P_C = 14.7$ psi
$P^I = 53 e^{-104t}$
$f = 1700$ cps

pressure, amplitude psi

time, millisec.

9"Dia.
Station #5
4"

Figure   45b

Second nonlinear combustion instability model

Figure 46

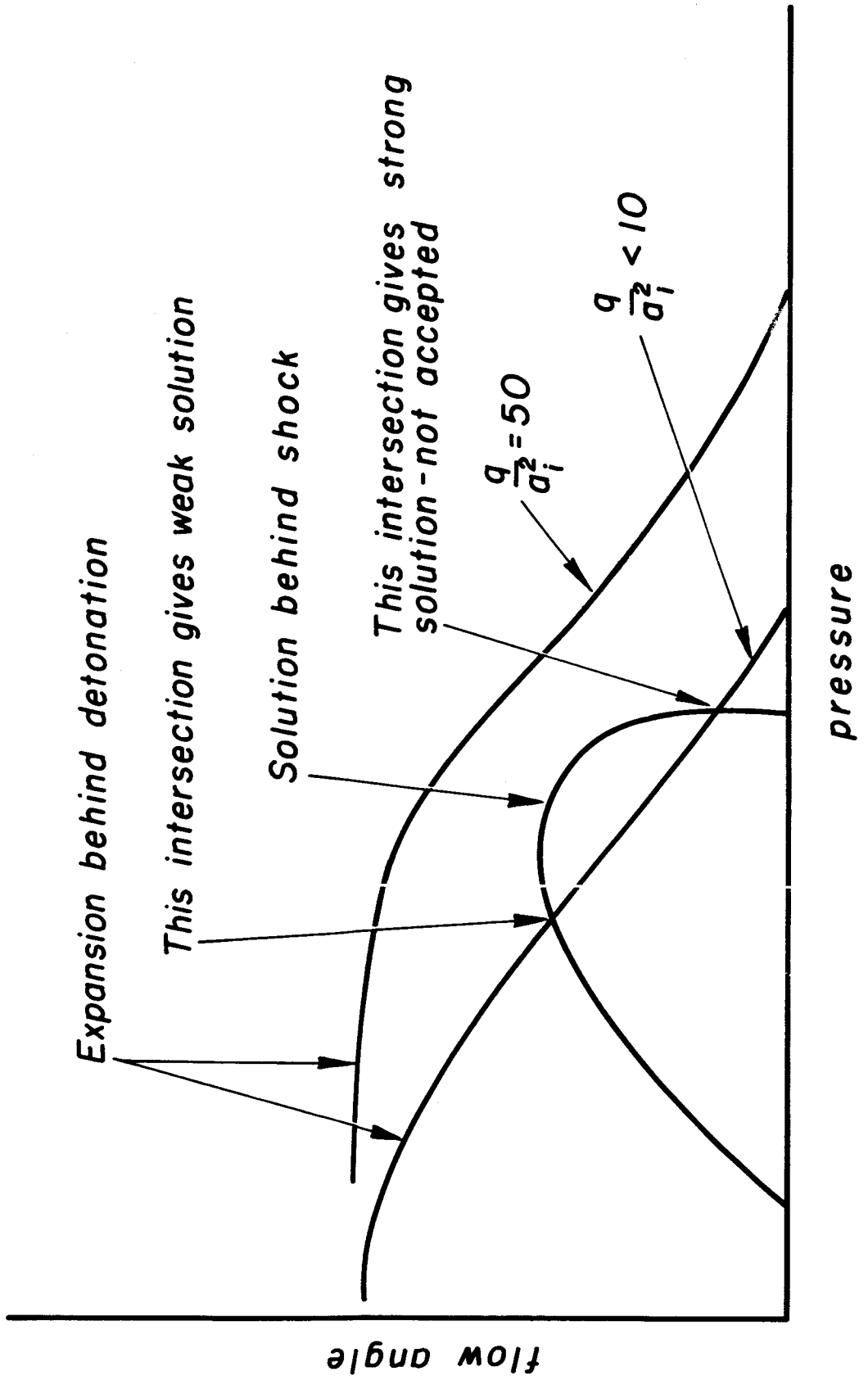Graphical Illustration of solution to theoretical model
of transverse instability

Figure 47

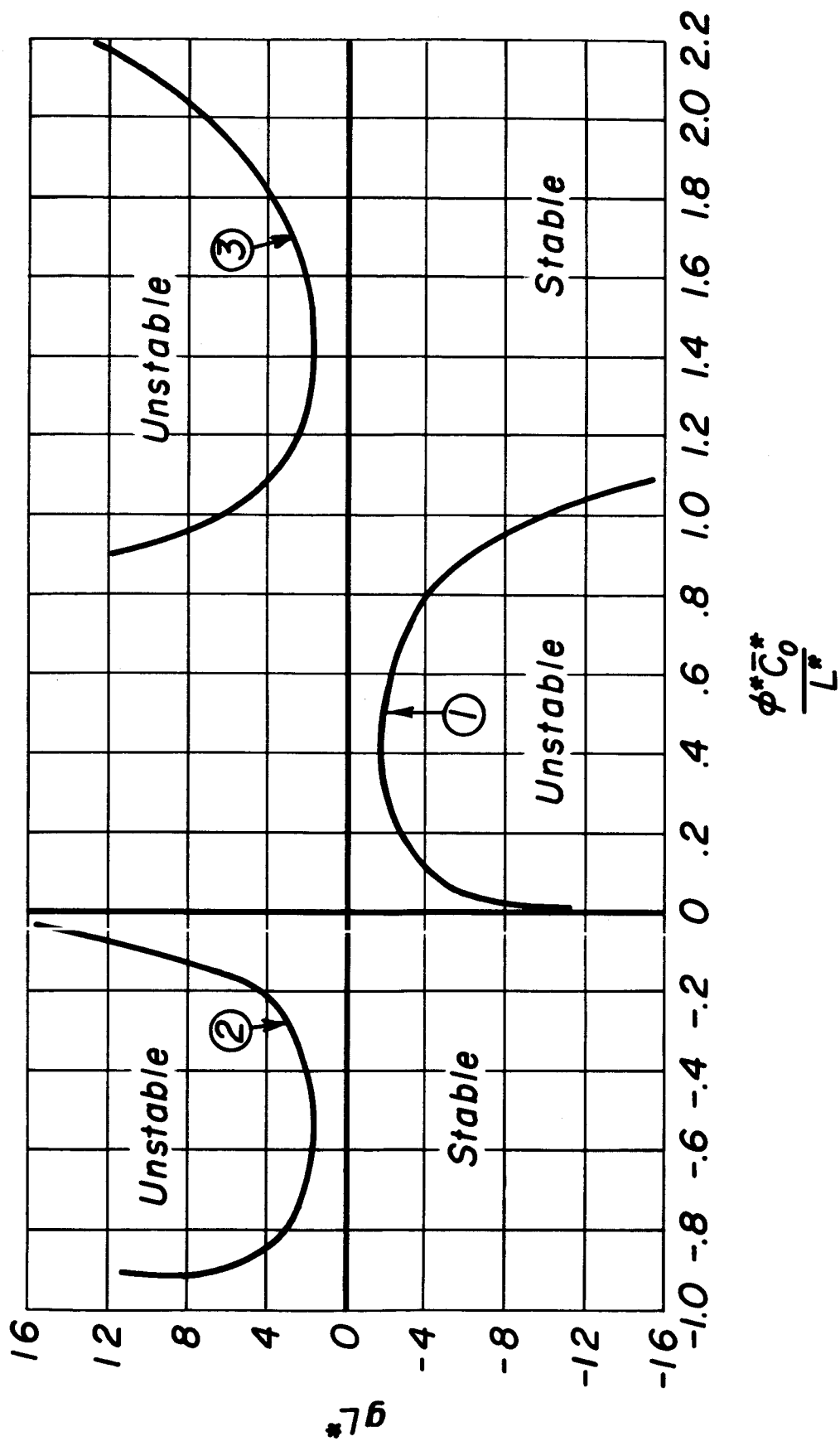Instability regions for median
injected drop size fluctuations

Figure 48

Injector response lag vs frequency at a stability limit
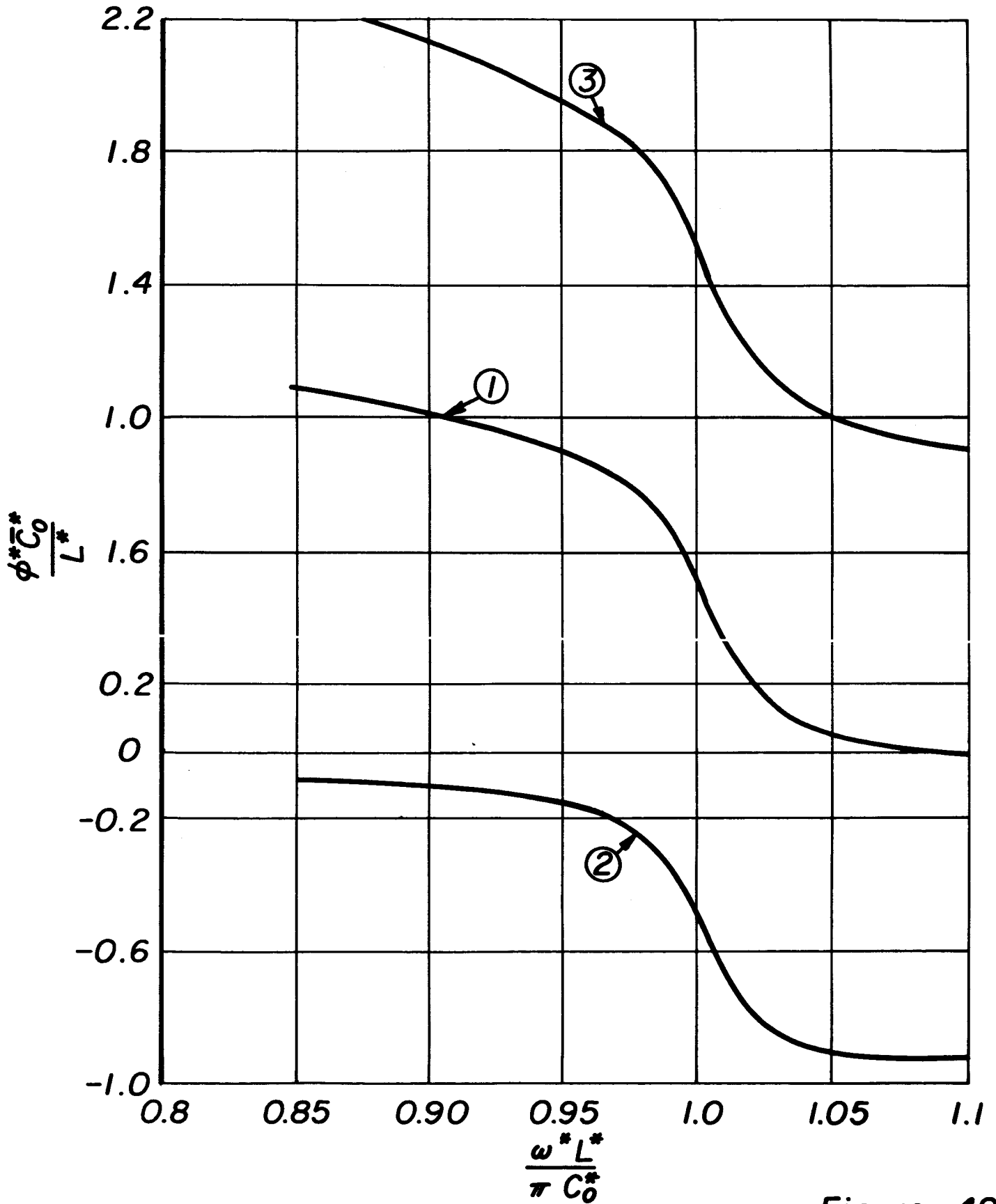
Figure 49

DISTRIBUTION LIST

TECHNICAL AND YEARLY PROGRESS REPORTS

U. S. Dept. of the Interior
Bureau of Mines
4800 Forbes Avenue
Pittsburgh 13, Pennsylvania
ATTN: M. M. Dolinar, Rept. Lib.
     Explosives Res. Lab. (1)

Central Intelligence Agency
2430 E. Street, N. W.
Washington, 25, D. C.
ATTN: OCD, Std. Dist. (1)

Nat'l Aeronautics & Space Admin.
1512 H Street, N. W.
Washington 25, D. C.
ATTN: Chief Div. Res. Info. (5)

Nat'l Aeronautics & Space Admin.
Langley Research Center
Langley Field, Virginia
ATTN: E. R. Gilman, Librn. (1)

Nat'l Aeronautics & Space Admin.
Lewis Research Center
21000 Brookpark Road
Cleveland 35, Ohio
ATTN: Library (1)

Commander
Air Force Flight Test Center
Edwards AFB, California
ATTN: FTOTL (1)

Department of the Air Force
Headquarters USAF, DCS/D
Washington 25, D. C.
ATTN: AFDRT/AS (1)

ARO, Inc.
Arnold Engng. Dev. Center
Arnold AF Station, Tennessee
ATTN: Dr. B. H. Goethert
     Director of Engng (1)

Commander
Air Force Missile Dev. Center
Holloman, AFB, New Mexico
ATTN: MDGRT (1)

Commander
Air Force Missile Test Center
Patrick AFB, Florida
ATTN: MTASI (1)
     MTRSS (1)

Commander
AF Office of Scientific Research ARDC
Washington 25, D. C.
ATTN: SRHP, Dr. J. F. Masi (1)

Commander
Air Force Systems Command
Andrews Air Force Base
Washington 25, D. C.
ATTN: SCTAP (1)

ASTIA
Arlington Hall Station
Arlington 12, Virginia
ATTN: TIPCR (10)

Office of the Director of Defense
  Research and Engineering
Washington 25, D. C.
ATTN: D. B. Brooks, Off. of
     Fuels & Lubricants (1)

Space Systems Division
Air Force Systems Command
P. O. Box 262 AF Unit Post Office
Los Angeles 45, California
ATTN: TDC

Commanding Officer
Picatinny Arsenal
Liquid Rocket Propulsion Lab.
Dover, New Jersey
ATTN: Tech. Lib. (2)
     Mr. Jenkins (1)

Commander
Arnold Engng. Dev. Center
Air Force Systems Command
Tullahoma, Tennessee
ATTN: EOIM (1)

Commanding General
Aberdeen Proving Ground
Maryland
ATTN: Ballistics Res. Lab.
ORDBG-BLI (1)

Commander
U.S. Army Ordnance Missile Command
Redstone Arsenal, Alabama
ATTN: Tech. Lib. (3)

U.S. Army Chemical Research and
Development Labs
Army Chemical Center, Maryland
ATTN: Keith H. Jacobson
Medical Res. Dir. (1)

Commanding Officer
Diamond Ordnance Fuze Lab
Washington 25, D. C.
ATTN: ORDTL (012) (1)

Commanding Officer
Army Research Office
Box CM, Duke Station
Durham, North Carolina (1)

Commanding Officer
Picatinny Arsenal
Dover, New Jersey
ATTN: Librn. (1)

Commander
Army Rocket & Guided Missile Agency
Redstone Arsenal, Alabama
ATTN: Tech. Lib. (2)

Commanding Officer
ONR Branch Office
1030 Green Street
Pasadena, California (1)

Superintendent
U. S. Naval Postgraduate School
Naval Academy
Monterey, California (1)

Commanding General
White Sands Missile Range
New Mexico
ATTN: Lib. (1)

Bureau of Naval Weapons
Department of the Navy
Washington 25, D. C.
ATTN: RMMP-24 (3)

Bureau of Naval Weapons
Department of the Navy
Washington 25, D. C.
ATTN: RRRE-6 (1)

Bureau of Naval Weapons
Department of the Navy
Washington 25, D. C.
ATTN: RMMP-4 (1)

Commander
Pacific Missile Range
Point Mugu, California
ATTN: Tech. Lib., Code 212 (2)

Commander
Naval Ordnance Lab
White Oak
Silver Spring, Maryland
ATTN: E. C. Noonan (1)

Commander
U. S. Naval Ordnance Test Station
China Lake, California
ATTN: Code 45 (5)

Director (Code 6180)
U. S. Naval Research Lab
Washington 25, D. C.
ATTN: H. W. Carhart (1)

Armour Research Foundation
Illinois Inst. of Tech.
Chicago, Illinois
ATTN: C. K. Hersh
Chem. Div. (1)

Arthur D. Little, Inc.
Acorn Park
Cambridge , Massachusetts
ATTN: D. C. Bowersock, Jr. (1)

Commanding Officer
U. S. Naval Underwater Ord. Sta.
Newport, Rhode Island
ATTN: W. W. Bartlett (1)

Aerojet-General Corporation
P. O. Box 296
Azusa, California
ATTN: M. Grenier, Librn (1)

Aerojet-General Corporation
Sacramento Plants
P. O. Box 1947
Sacramento 9, California
ATTN: R. G. Weitz, Head
      Tech. Info. Office (1)

Aeronutronic
Division of Ford Motor Company
Ford Road
Newport Beach, California
ATTN: Library (1)

Aeroprojects, Inc.
West Chester, Pennsylvania
ATTN: W. Tarpley (1)

Air Reduction Company, Inc.
Murray Hill, New Jersey
ATTN: Dr. Fred Balcar (1)

American Cyanamid Company
1937 W. Main Street
Stamford, Connecticut
ATTN: Dr. A. L. Peiler (1)

General Electric Company
Rocket Propulsion Units
Building 300
Cincinnati 15, Ohio
ATTN: S. F. Sarner (2)

Hughes Tool Company
Aircraft Division
Culver City, California
ATTN: Dr. I. Shapiro (1)

Jet Propulsion Laboratory
4800 Oak Grove Drive
Pasadena 3, California
ATTN: I. E. Newlan, Chief
      Rept. Group (1)

Atlantic Research Corporation
Edsall Road & Shirley Highway
Alexandria, Virginia (2)

Bell Aerosystems
Box 1
Buffalo 5, New York
ATTN: T. Reinhardt (1)

Callery Chemical Company
Callery, Pennsylvania
ATTN: Document Control (1)

The Dow Chemical Company
Security Office
P. O. Box 31
ATTN: I. G. Morrison,
      Chem. Dept. (1)

Esso Research and Engng. Company
P. O. Box 51
Linden, New Jersey
ATTN: Dr. J. P. Longwell
      Spec. Proj. Unit (1)

Texaco Experiment, Inc.
P. O. Box 1-T
Richmond 2, Virginia
ATTN: Library (1)

Food Machinery and Chemical Corp.
Special Projects Branch
P. O. Box 38
Buffalo 13, New York (1)

The Fulton-Irgon Corporation
P. O. Box 591
Dover, New Jersey
ATTN: David Lippmann (1)

Phillips Petroleum Company
145 Chemical Laboratories Bldg.
Bartlesville, Oklahoma
ATTN: H. M. Fox (1)

Purdue University
Lafayette, Indiana
ATTN: M. J. Zucrow (1)

Reaction Motors Division
Thiokol Chemical Corporation
Denville, New Jersey
ATTN: Library (1)

Liquid Propellant Information Agency
Applied Physics Laboratory
The Johns Hopkins University
8621 Georgia Avenue
Silver Spring, Maryland (3)

Marquardt Corporation
16555 Saticoy Street
Box 2013 - South Annex
Van Nuys, California (1)

Minnesota Mining & Manufacturing C.
900 Bush Avenue
St. Paul 6, Minnesota
ATTN: R. W. McElroy, Sec. Adm.
      For: J. W. Millin (2)

New York University
Department of Chemical Engineering
New York 53, New York
ATTN: P. F. Winternitz (1)

Olin Mathieson Chemical Corp.
Research Library
New Haven, Connecticut
ATTN: Mrs. Laura M. Kajuti (3)

Peninsular ChemResearch, Inc.
P. O. Box 3597
1207 N.W. Fifth Avenue
Gainesville, Florida
ATTN: Paul Tarrant (1)

Monsanto Chemical Company
Research and Engineering Division
Spec. Proj. Dept. - 1 Chem. Lane
Everett Station, Boston 49, Mass.
ATTN: K. Warren Easley (1)

Texaco, Inc.
Texaco Research Center
Beacon, New York
ATTN: Tech. Lib. (1)

Nat'l Aeronautics & Space Admin.
1520 H Street
Washington 25, D. C.
ATTN: T. L. K. Smull
      Code BG (10)

Rocketdyne
North American Aviation, Inc.
6633 Canoga Avenue
Canoga Park, California
ATTN: J. Silverman (3)

Rohm and Haas Company
Redstone Arsenal
Huntsville, Alabama
ATTN: Librn (1)

Shell Development Company
Emeryville, California
ATTN: R. R. Ward (1)

Space Technology Labs
P. O. Box 95001
Airport Station
Los Angeles 45, California
ATTN: James R. Dunn (1)

Stauffer Chemical Company
Chauncey, New York
ATTN: J. R. Gould (1)

Thiokol Chemical Corp.
Redstone Division
Huntsville, Alabama
ATTN: Tech. Dir. (1)

Wyandotte Chemicals Corp.
Wyandotte, Michigan
ATTN: R. A. Graham
      Dept. Cont. Res. (1)

Union Carbide Chemicals Company
Development Department
P. O. Box 8356
South Charleston, West Virginia
ATTN: Dr. H. W. Schulz (1)

United Aircraft Corporation
400 Main Street
East Hartford, Connecticut
ATTN: Library (1)

Engineering Projects Laboratory
Massachusetts Inst. Tech.
Cambridge 39, Massachusetts
ATTN: Gail E. Partridge, Librn. (1)

Thayer School of Engineering
Dartmouth College
Hanover, New Hampshire
ATTN: Prof. Robert C. Dean, Jr. (1)

American Potash & Chemical Corp.
201 W. Washington Boulevard
Whittier, California
ATTN: Dr. R. Stewart (1)

Space Systems Division
Rocket Test Annex
Edwards, California
ATTN: DGR (1)
      DGPL (1)

Commander
Aeronautical Research Laboratory
Wright-Patterson AFB, Ohio
ATTN: ARC, Mr. Karl Scheller (1)

Allied Chemical Corporation
General Chemical Division
Research Laboratory
P. O. Box 405
Morristown, New Jersey
ATTN: L. G. Wiltrakis
      Sec. Office (1)

Aerospace Corporation
P. O. Box 95085
Los Angeles 45, California
ATTN: Dr. D. H. Loughridge
      Dir. Appl. Res. Mgmt. (2)

Battelle Memorial Institute
505 King Avenue
Columbus 1, Ohio
ATTN: Mr. Charles E. Day
      Classified Rept. Librn (1)

McGraw-Hill Tech. Writing Service
McGraw-Hill Book Company
330 W. 42nd Street
New York 36, New York (1)

Aeronautical Systems Division
Wright Patterson AFB, Ohio
ATTN: ASNRPP (1)
      ASRCEE-1 (1)

Department of the Navy
Office of Naval Research
Washington 25, D. C.
ATTN: Power Branch
      Code 429

General Dynamics/Convair
San Diego 12, California
ATTN: Engng Library
      K. G. Blair, Ch. Librn.
      Mail Zone 50-03 (1)

Aerojet-General Corporation
Combustion Dynamics Section
Thrust Chamber Technical Staff
Department 9616
Sacramento, California
ATTN: Dr. F. Reardon